Karlsruhe Institute of Technology

Annual Report 2022 of the Institute for Thermal Energy Technology and Safety

Walter Tromm (Ed.)

KIT SCIENTIFIC WORKING PAPERS 249

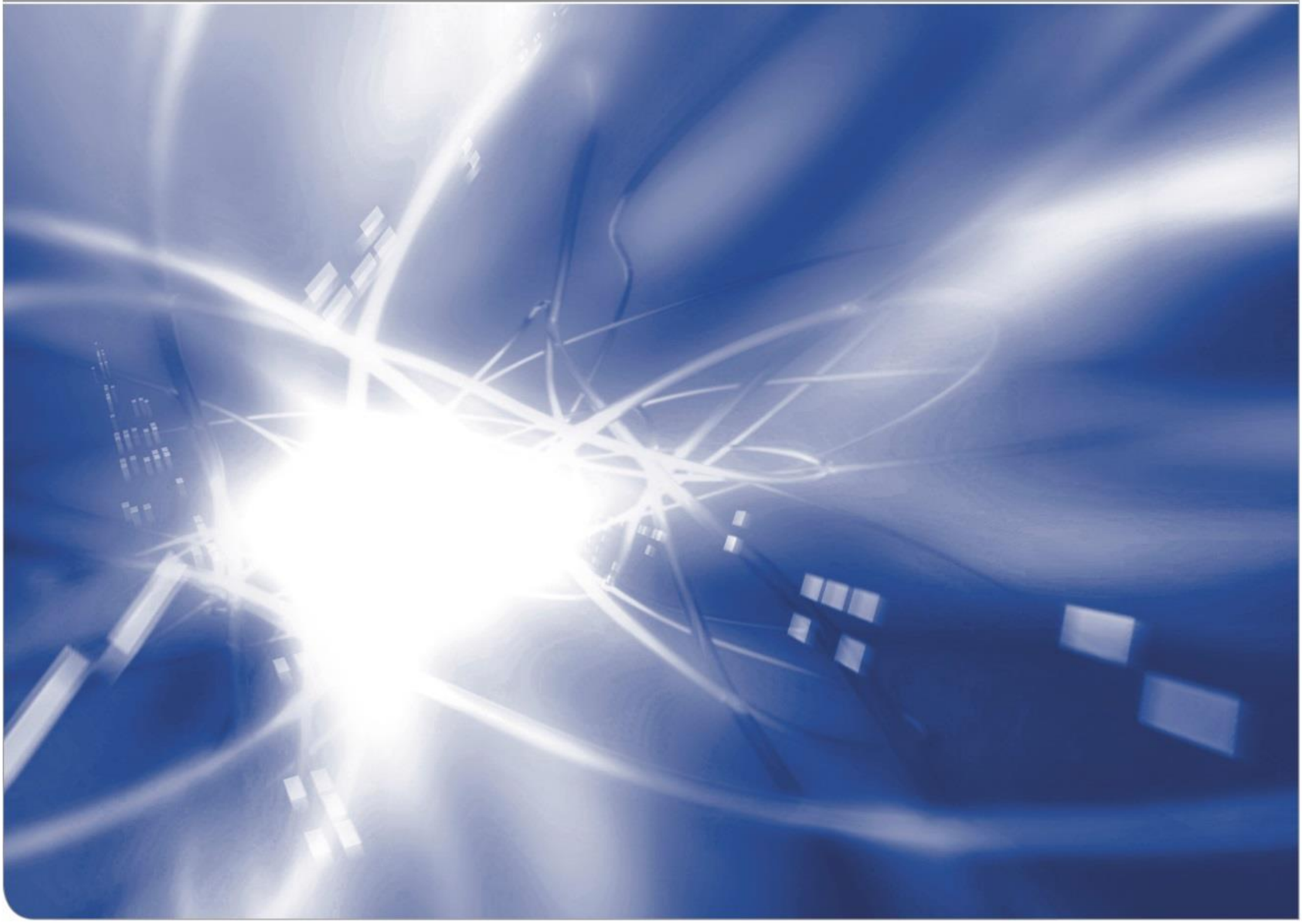

KIT – The Research University in the Helmholtz Association

www.kit.edu

Institute for Thermal Energy Technology and Safety
Hermann-von-Helmholtz Platz 1
76344 Eggenstein-Leopoldshafen
https://www.ites.kit.edu

Impressum

Karlsruher Institut für Technologie (KIT)
www.kit.edu

This document is licensed under the Creative Commons Attribution – Share Alike 4.0 International License (CC BY-SA 4.0): https://creativecommons.org/licenses/by-sa/4.0/deed.en

2024

ISSN: 2194-1629

Content

Institute for Thermal Energy Technology and Safety

Structure and Activities of the Institute for Thermal Energy Technology and Safety (ITES)

Walter Tromm

The Institute for Thermal Energy and Safety (ITES) is situated with its offices and research laboratories in Campus North of Karlsruhe Institute of Technology (KIT).

The research of ITES focuses on conversion from thermal power to electric power for future power systems without CO2 emission including hydrogen technologies and on safety. In the past ITES concentrated on safety features and on methods to mitigate severe accidents for nuclear power plants. Nowadays, ITES uses these competences, gained from a profound experience in numerical simulation and in design and operation of large-scale experimental facilities to apply this knowledge mainly in the area of renewable energies.

The combination of science and technology with education and training is a systematic approach at KIT, and ITES is contributing accordingly to courses in mechanical engineering, supervises several bachelor and master theses each year and coordinates master programs in energy technologies. Compact courses on energy technologies are given also in executive master programs and in the Framatome Professional School, which is funded by industry and managed by ITES.

Resources

The employees of ITES contribute to the research-programs Materials and Technologies for the Energy Transition (MTET), Energy System Design (ESD), Fusion (FUSION), and Nuclear Waste Management, Safety and Radiation Research (NUSAFE) in the research field energy of the Helmholtz Association (HGF). By the end of 2022, around 94 scientists, engineers and technicians have been working at ITES on this wide range of CO_2-free technologies for energy conversion. Fig. 1 illustrates that 41 % of the ITES employees were working for the NUSAFE program, but steadily reduced in recent years. Around two third of the employees were funded in 2022 by the Helmholtz Association (HGF), the others by third party funds of the European Commission, by industry, by German ministries or by other research funds. Doctoral students as well as students of the Baden-Wuerttemberg Cooperative State University (DHBW) were filling around 20 % of these positions at ITES. In addition, students perform their bachelor or master theses or spend an internship in the research laboratories of ITES.

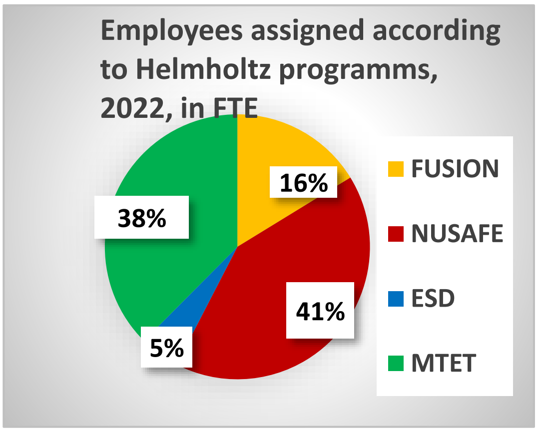

Fig. 1: Assignment of ITES personnel to Helmholtz programs.

An overview of the structure of ITES is given by the organization chart, Fig. 2. Because all working groups are embedded in the research field energy of the Helmholtz association (HGF) a close collaboration within the groups is guaranteed.

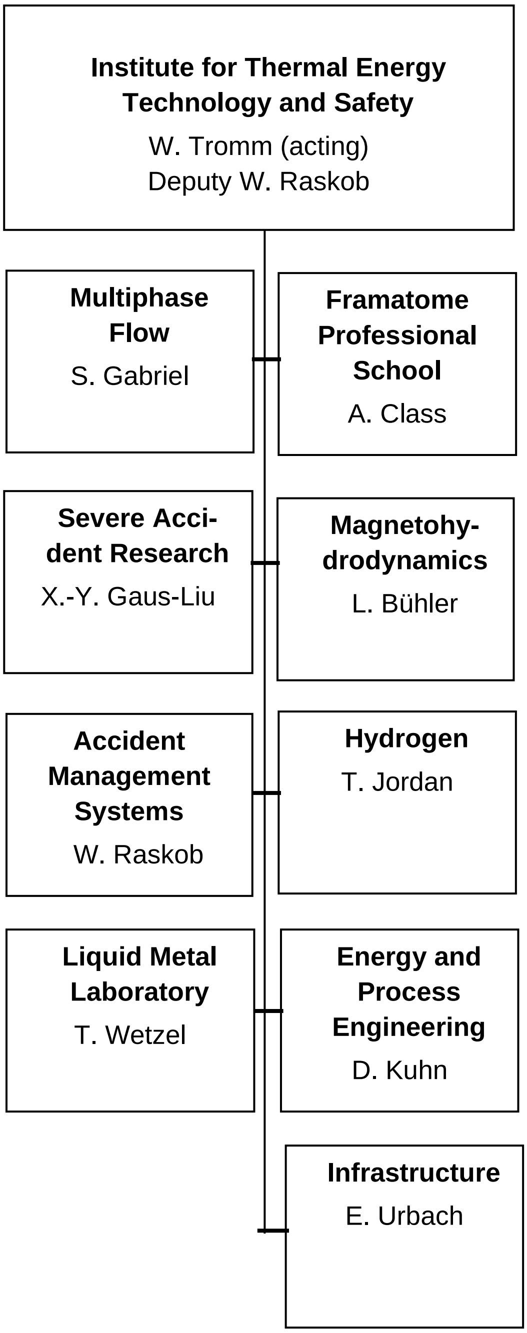

Fig. 2: Organization chart of the Institute for Thermal Energy Technology and Safety

Working groups on Severe Accident Research, on Multi-Phase Flow as well as the Framatome Professional School still concentrated in 2022 primarily on nuclear applications, whereas the Karlsruhe Liquid Metal Laboratory (KALLA) and the Hydrogen group were addressing nuclear as well as renewable energy technologies. The working group on Magneto-Hydrodynamics is primarily working on nuclear fusion applications, whereas the working group on Energy and Process Engineering is concentrating on geothermal energies. The working group Multiphase Flows is mainly experimentally investigating technically relevant, complex flow phenomena. The field of activity currently focuses on the build-up of the complex structure of the COSMOS-H high-pressure loop. The working group on Accident Management Systems continued to extend the application of its simulation models not only to nuclear emergency cases but to several critical infrastructures within the program ESD. Thus, the institute covers a wide field of different energy technologies and related safety investigations. The share of personnel resources on the different research topics reflects the requirements of the Helmholtz Association's energy research field.

They are all supported by a joint infrastructure, comprising a metal workshop, manufacturing urgent test components, a welding shop, and an electromechanical workshop. Other tasks of the infrastructure include the IT-administration, business administration and public website of the ITES. The Infrastructure team is active as well in education and training activities.

Every year, several students of the Baden-Württemberg Cooperative State University are employed by ITES, managed by the Infrastructure group, to work with the research teams as part of their educational program.

Working in a research area with industrial application ITES practices a Quality Management System appropriate to EN ISO 9001.

Department: Magnetohydrodynamics

Magnetohydrodynamics for liquid-metal blankets

L. Bühler, B. Lyu, H.-J. Brinkmann, C. Courtessole, V. Klüber, C. Köhly, C. Mistrangelo, J. Roth

MHD flows in blanket manifolds

In the frame of the EUROfusion research program, liquid metal blankets are being developed and experimentally tested in the International Thermonuclear Experimental Reactor (ITER), where lead lithium (PbLi) is used as breeder material and heat transfer medium. For purification and tritium extraction, the liquid metal is circulated towards external ancillary facilities. The flow of the electrically conducting PbLi in the plasma-confining magnetic field induces electric currents and related electromagnetic forces affect the flow distribution and create enormous pressure drop. Across electrically conducting walls separating neighboring fluid regions, leakage currents may create significant electromagnetic flow coupling.

Magnetohydrodynamic (MHD) analyses performed at ITES in 2022 focussed on the performance of the European reference concept of a water-cooled lead lithium (WCLL) blanket, which has been selected as a test blanket module (TBM) for ITER. The flow has been studied in a scaled mock-up using NaK as a model fluid in the MEKKA facility of ITES at KIT (see Figure 1). Typical flow paths and poloidal, toroidal and radial coordinates are indicated in Figure 2. The feeding manifold of the mock-up is supplied with liquid metal by a circular pipe, the fluid distributes among the breeder zones (blue line) by passing through windows in the back plate. Then it circulates in radial direction to approach the first wall, turns in poloidal direction around the BU baffle plate before flowing radially towards the collecting windows and into the draining manifold (red line). A detailed description of the experimental test-section, installation and instrumentation has been presented in [1].

Key components for the performance of blanket modules are the manifolds distributing PbLi among breeder units (BUs) [2, 3]. The liquid metal flow in WCLL manifolds and BUs has been analyzed using a hybrid asymptotic approach, by full numerical simulations and by experiments performed in MEKKA. The analyses take care of the fact that in the present design, the feeding and draining manifolds have different size.

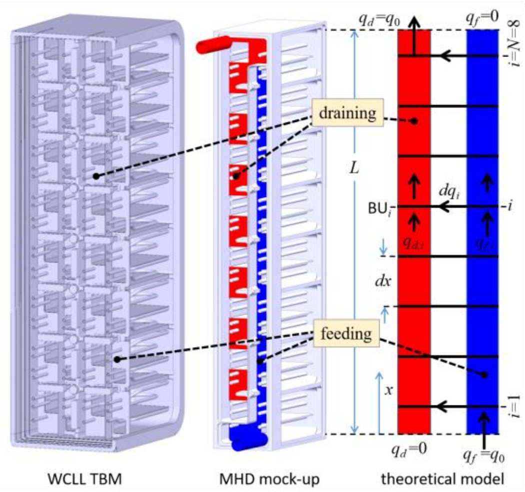

Figure 1 Design of a scaled mock-up for MHD experiments in MEKKA with 8 BUs stacked along the poloidal direction [1]. The geometry has been derived from the WCLL ITER TBM [4]. View into the system of manifolds and sketch defining details of the theoretical model [5].

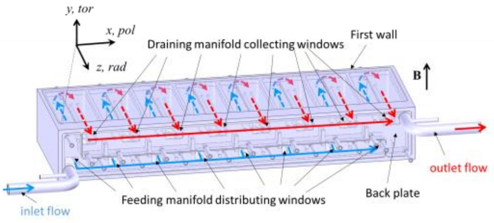

Figure 2 Experimental MHD mock-up of a WCLL TBM with schematic liquid metal paths. Poloidal, toroidal and radial coordinates are x, y and z.

Hybrid approach for determining pressure drop and flow distribution

The hybrid approach is based on asymptotic theory used for 3D simulations of electrically coupled flow in distinct poloidal sections of the manifolds. For such analyses, the entire geometry is split into a number unit elements of poloidal length dx, such as the one displayed in Figure 3.

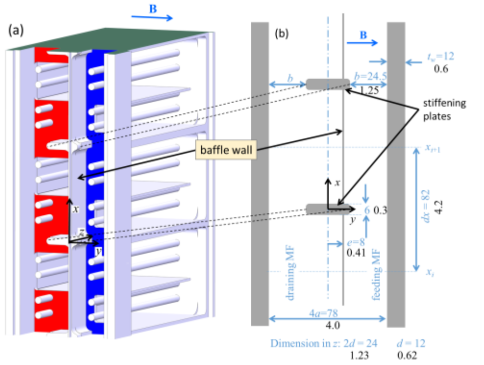

Figure 3 view of a TBM mock-up and definition of a unit element (a); geometry and coordinates (b). Black notation is nondimensional and scaled with *a*, the blue one is measured in mm.

As described in [5], coupled asymptotic simulations have been performed for the prototypical geometry of length dx, assuming various pressure heads Δp_f and Δp_d for feeding and draining manifolds.

The flow is governed by the nondimensional Hartmann number and the interaction parameter

$$Ha = aB\sqrt{\frac{\sigma}{\rho\nu}}, \quad N = \frac{\sigma a B^2}{\rho u_0},$$

where *a* stands for a typical length of the problem (see Figure 3, further details of the simulations can be found in [5]), B denotes the magnitude of the magnetic field, and specific electric conductivity, density, and kinematic viscosity of the fluid are σ, ρ, and ν. Ha is a nondimensional measure for the strength of the magnetic field and N denotes the ratio of electromagnetic to inertia forces. The hydrodynamic Reynolds number is related to these parameters as $Re=Ha^2/N$.

One such result for velocity distribution in two cross sections and electric potential ϕ plotted on the fluid-wall interface is shown in Figure for the special case of $\Delta p_f = \Delta p_d$. We observe relatively smooth velocity distributions in cores with thin Hartmann boundary layers at walls perpendicular to the magnetic field and jets with high velocity at walls parallel to $\boldsymbol{B}$. The flow partitioning is expressed in flow rate fractions $\alpha = q/q_0$, where individual flow rates q are measured as fractions of the total flow rate q_0. Various simulations yield the fractions of flow α_f and α_d carried by the feeding and draining manifolds, depending on Δp_f and Δp_d. Vice versa, we may interpret the results as shown in Figure 5 in order to define pressure drop correlation as $\Delta p_f(\alpha_f)$ and $\Delta p_d(\alpha_d)$. The latter ones are required as input of the hybrid model to assemble the data for prescribing the global performance of the module.

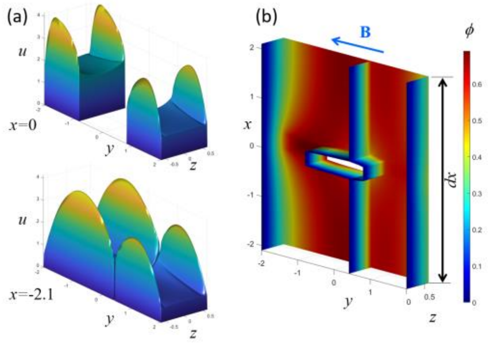

Figure 4 Results of a simulation with electromagnetic coupling at $Ha=1000$, for pressure differences $\Delta p_f = \Delta p_d$. (a) Velocity profiles in the symmetry plane $x=0$ and near the entrance $x = -2.1$, (b) view on the distribution of nondimensional electric potential on the fluid-wall interface in half of the geometry for $z>0$.

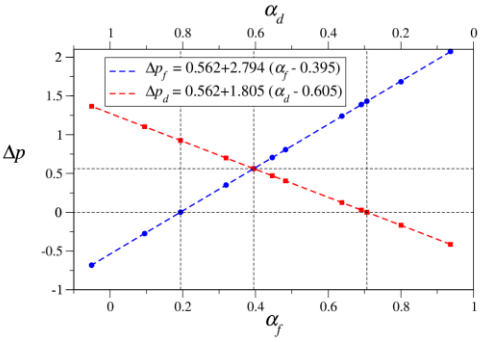

Figure 5 Variation of pressure drops with flow rates, $\Delta p_f(\alpha_f)$ and $\Delta p_d(\alpha_d)$.

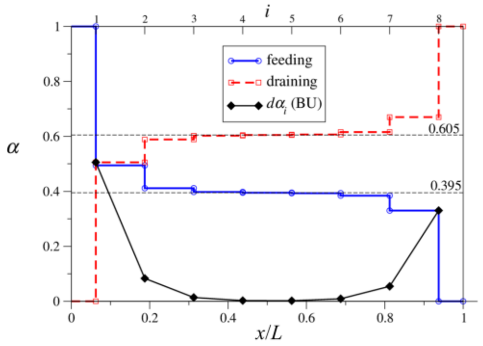

Figure 6 Distribution of flow rates in feeding and draining channels and in BUs of a WCLL TBM mock-up.

Data displayed in Figure 5 is used as input for the global model, which ensures mass conservation as $\alpha_{f,i} + \alpha_{d,i} = 1$, i.e. the entire flow is carried by the feeding and draining ducts and eventually the total exchange between the both sections is accomplished by the flux though all BUs as $\Sigma d\alpha_i = 1$.

Coming from the smaller feeding duct, the fluid tries to reach the larger draining manifold as soon as possible. Figure 6 shows that BU1 and BU2 transfer approximately 50% and 8% of the flow from the feeding to the draining ducts, respectively. Then flow rate fractions are close to $\alpha_f = 0.395$ and $\alpha_d = 0.605$, for which pressure drops in feeding and draining ducts are equal (Figure 5). Flow rates carried by BU3÷BU6 become insignificant so that an efficient exchange of fluid in these units is not guaranteed. The remaining flow is transferred to the draining duct via BU7 (5%) and BU8 (33%). The obtained non-uniform flow distribution among BUs is not acceptable for applications and ongoing work will determine optimal values of $e(x)$ in order to overcome this deficiency.

Mock-up experiments in MEKKA

To investigate the pressure distribution and flow partitioning in the WCLL TBM, a 1:2.5 scaled mock-up was fabricated and experiments were performed in the MEKKA facility using NaK as a model fluid. The manifolds were reproduced as faithfully as possible given the influence these components have on the flow. The entire test section is made of stainless steel (1.4571) and its external dimensions are 668.4mm × 102.0mm × 222.6 mm (see Figure 7).

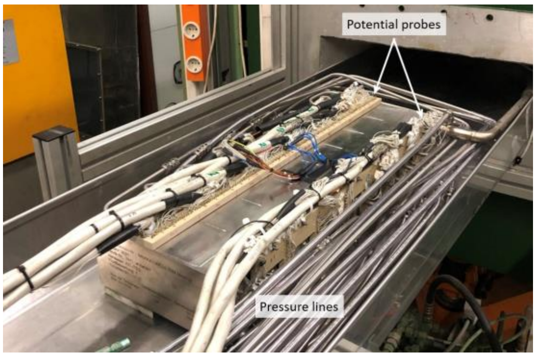

Figure 7 Mock-up installed in front of the magnet with pressure taps connected to the pressure measurement system and electrodes installed on the top wall and on the sidewall of the manifolds.

Details of the instrumentation are depicted in-Figure 8. The pressure distribution is measured by 28 pressure taps located throughout the entire mock-up. For accurate measurements, the pressure taps are connected via a series of pneumatically actuated valves to 5 capacitive pressure transducers with different measuring ranges scaling from a few mbar up to 10 bar. Additionally, electric potential distributions are recorded on the surface of the mock-up. For that purpose, two insulating Peek plates equipped with 160 and 120 spring-loaded gold-plated electrodes are installed on the top Hartmann wall and the back plate of the manifolds, respectively.

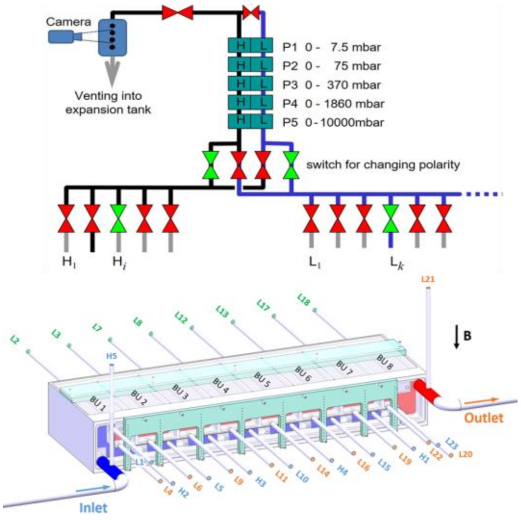

Figure 8 Sketch of the mock-up showing the labelled pressure taps (bottom) and of the differential pressure measurement system showing how the pressure taps are connected to the capacitive pressure transducers (top).

Experiments were performed for various flowrates and strengths of the magnetic field. In the following, nondimensional parameters are expressed using a characteristic length L_{BU} corresponding to half the height of the BUs and the mean velocity u_{BU} resulting from an assumed evenly distributed flow across all 8 BUs, i.e. $u_{\mathrm{BU}}=(q_0/8)/(A_{\mathrm{BU}}/2)$ where q_0 is the volumetric flowrate and A_{BU}, the entire cross-section of a single BU.

A typical pressure distribution obtained for $Ha = 1000$ and $Re = 1000$ is shown in Figure 9. Results are plotted against the curvilinear coordinate *s* that denotes the length of the flow path in the mock-up. The pressure is scaled by the characteristic value in the manifolds $p_{\mathrm{M}}=\sigma u_{\mathrm{M}} L_{\mathrm{M}} B^2$ based on the mean velocity in the manifolds $u_{\mathrm{M}}=q_0/A_{\mathrm{M}}$ and their characteristic length scale $L_{\mathrm{M}}=L_{\mathrm{BU}}/2$.

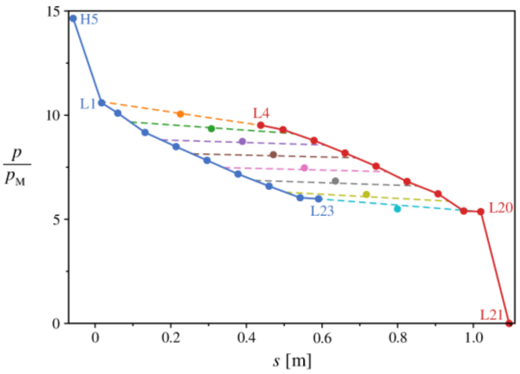

Figure 9 Pressure distribution along typical flow paths measured for $Ha = 1000$ and $Re = 1000$.

Most of the pressure drop occurs at the inlet and outlet of the mock-up caused by strong 3D effects when the fluid passes through the sudden expansion between the inlet circular pipe and the feeding manifold (between H5 and L1) or when the flow cross-section contracts at the exit of the mock-up (between L20 and L21). The rest of the pressure drop is mainly caused by the manifolds where the liquid metal flows much faster than in the breeder units. From Figure 9, one can observe that the pressure head across the BUs are larger in BU1 and BU8, respectively than in the other BUs. This is perhaps better highlighted when plotting the pressure distribution along the corrected poloidal coordinates ξ shown in Figure 10. This result reveals that the pressure heads $\Delta p_{BU} = \Delta p_f - \Delta p_d$ differ between BUs and therefore the flow is not uniformly distributed across all the BUs. This result supports the conclusions of the hybrid model presented above.

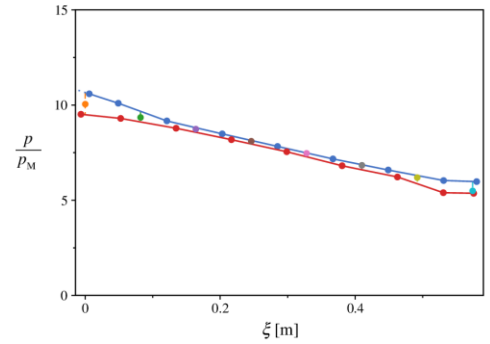

Figure 10 Pressure distribution along poloidal coordinates ξ in the feeding (blue) and collecting (red) manifolds for $Ha = 1000$ and $Re = 1000$. The origin of ξ for both manifolds has been chosen as the center of the respective windows connecting the BUs to the manifolds. The origin of ξ for pressure taps at the first wall has been chosen at the pressure tap in BU1.

Pressure differences were measured between selected pressure taps for a wide range of Re numbers and $500 \leq Ha \leq 4000$. Results obtained for the entire mock-up $\Delta p_{All}=p_{H5}-p_{L21}$ as well as for the contributions of both manifolds, $\Delta p_{FM}=p_{H2}-p_{L23}$ and $\Delta p_{CM}=p_{L4}-p_{L22}$, and of the inlet and outlet of the mock-up where the flow suddenly expands ($\Delta p_{Exp}=p_{H5}-p_{L1}$) and contracts ($\Delta p_{Cont}=p_{H20}-p_{L21}$) are displayed in Fig. 11.

It can be seen that these pressure drops fall into 5 lines when plotted against the interaction parameter N. For the largest N values ($N \geq 1000$), i.e. for all Re investigated when $Ha \geq 3000$, the overall pressure drop in the mock-up becomes constant as the flow becomes inertialess. In this regime, the pressure losses created by the sudden expansion and contraction converge to the same value $\Delta p_{Exp} \approx \Delta p_{Cont} \approx 3.8$ as the expansion and the contraction have the same geometry and the associated pressure loss no longer depends on the flow direction. This is however not the case when inertia effects are stronger. For smaller interaction parameters, the pressure drop created when the flow enters the mock-up decreases with N^{-1} and even becomes negative at the highest Re and lowest Ha considered here. However, the pressure drop that occurs at the sudden contraction remains much larger than the pressure recovery occurring at the inlet of the mock-up.

In the manifolds, results confirm that the pressure drops created by both manifolds are equal for $N > 10$. It was found that for $10 \leq N \leq 1000$, the pressure loss scales as $N^{-0.16}$. For the lowest interaction parameters ($N < 10$), i.e. in flow with weak electromagnetic effects, the pressure drop across the collecting manifold becomes larger than for the feeding one.

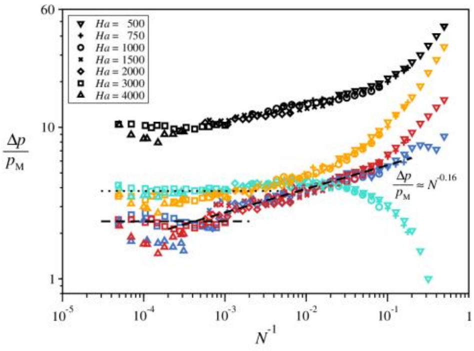

Figure 11 Pressure drop measured across the entire mock-up $\Delta p_{All}=p_{H5}-p_{L21}$ (black) and contributions of the feeding manifold $\Delta p_{FM}=p_{H2}-p_{L23}$ (blue), collecting manifold $\Delta p_{CM}=p_{L4}-p_{L22}$ (red), inlet expansion $\Delta p_{Exp}=p_{H5}-p_{L1}$ (teal), and outlet contraction $\Delta p_{Cont}=p_{L20}-p_{L21}$ (orange) as a function of the inverse interaction parameter N for $500 \leq Ha \leq 4000$ and various Re.

Results of electric potential measurements on the Hartmann wall of the BUs shown for the same parameters $Ha = 1000$ and $Re = 1000$ in Figure 12 further support previous observations. Nondimensional electric potential scaled by $\phi_{BU}=u_{BU}L_{BU}B$ confirms the uneven flow partitioning across all BUs. Although the Hartmann walls are too thick in the present case to determine directly the core velocity from the gradient of potential, the much larger signal variations observed in BU1 and BU8 compared to BU2÷BU7 clearly indicate higher flowrates in the external BUs than in the central elements of the module. Moreover, it can be seen that the signal in BU1 has almost twice the magnitude of that in BU8. This is again in agreement with the hybrid model and results from the larger cross-section of the collecting manifold compared to the feeding manifold.

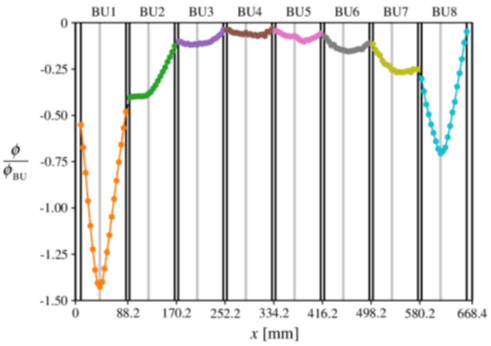

Figure 12 Electric potential distribution on the top Hartmann wall of the breeder units measured along the poloidal direction x for $Ha = 1000$ and $Re = 1000$. The location of the walls separating the BUs and of the baffle plates (in gray) are materialized by the vertical lines.

Full numerical simulations for the entire mock-up of a blanket module

Numerical simulations have been carried out to predict the MHD flow in an experimental mock-up when exposed to moderate uniform magnetic fields [6]. Figure 2 displays the design of the test-section with the principle sketch of the liquid metal path. For the present investigation, special care has been taken to find the optimal grid for resolving all the thin MHD boundary and internal layers.

In the following, results for the liquid metal MHD flow in an entire experimental mock-up of a WCLL TBM, shown in Figure 2, are described for a uniform magnetic field, for Ha=200, and an inlet velocity u_0=0.01m/s. For these preliminary simulations, the dummy pipes in the breeder zones have been omitted. Full electromagnetic coupling of neighboring fluid regions across electrically conducting walls has been taken into account.

In Figure 13a, velocity streamlines are plotted in the mock-up, visualizing some liquid metal paths both in the manifold ducts and in the breeder units. The fluid passes from the inlet pipe into the manifold and a part of it enters the window connecting the feeding manifold with BU1 (see red streamlines). The liquid metal then flows along the baffle plate, it returns towards the back plate to be collected by the second poloidal duct. The remaining liquid metal is supposed to distribute along the manifold among the other seven BUs. However, the largest portion flows directly to BU8.

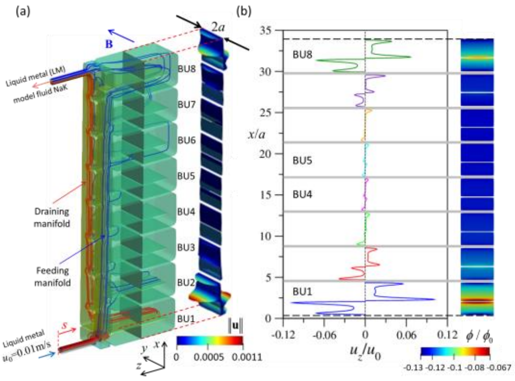

Figure 13 Flow in the experimental mock-up of a WCLL TBM at Ha=200 and inlet velocity u_0=0.01m/s. Velocity streamlines and 3D velocity contours in the middle xy plane of the geometry (a). Velocity profile in the center of the module and electric potential distribution on the same xy plane (b).

Profiles of radial velocity u_z in BUs are displayed both as 3D contours on the xy plane in the middle of the mock-up (Figure 13a) and as 2D graph along the poloidal centerline of the module (Figure 13b). Here the velocity has been scaled by the inlet velocity u_0. As expected in electrically conducting channels, the velocity distribution is characterized by uniform cores and side layer jets along walls parallel to the magnetic field. Full numerical results confirm that the flow rates in BU1 and BU8 are much larger than the ones in the other breeding zones. In BU3 ÷ BU6 there is almost no flow. The velocity distribution resembles the one obtained by numerical simulations for the MHD flow in a helium cooled lead lithium (HCLL) blanket mock-up, which were confirmed by experimental data [7]. Contours of electric potential on the same xy plane, shown in Figure b, exhibit analogously larger values in the first and last breeding zones.

The reason behind the significant flow imbalance is the geometry of the manifold where the cross-sections of the two poloidal ducts remain on average constant when the liquid metal moves in poloidal direction. On the other hand, the flow rate in the feeding and draining manifolds reduces and increases, respectively. For a better performance of the TBM with a more uniform flow partitioning among all BUs, the manifold design should be optimized so that the cross-sections of the ducts adapt to the changing flow rates along the poloidal liquid metal path.

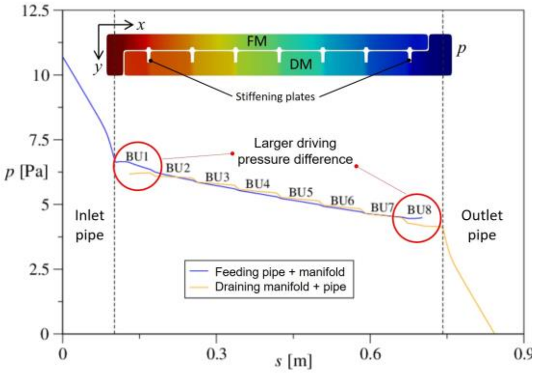

Figure 14 Pressure along pipes, feeding (FM) and draining (DM) manifolds. Coordinate *s* starts at the inlet pipe (see Figure 13a). In the subplot, contours of pressure are shown on a *xy* cross-section of the manifold.

These non-homogeneous characteristics of the flow in the WCLL TBM mock-up is evidenced by the pressure distributions along the manifolds that are plotted in Figure 14. The steps in the pressure profiles are due to the periodic occurrence of expansions and contractions along the liquid metal flow paths in the manifolds. These constrictions are caused by the penetration of the stiffening plates in the poloidal ducts (see *xy* plane in the subplot in Figure 14). The local pressure jumps are higher in the draining manifold since there the reduction of the cross-section is more significant than in the feeding one. The differences of pressure in feeding and draining manifolds constitute the pressure heads between entrance and exit of the BUs and they are obviously not the same for all BUs. At both module ends, highlighted by red circles, there are larger driving pressure differences causing the stronger flow through BU1 and BU8.

These preliminary results for moderate magnetic field provide first insight in the physical behavior of MHD flows in an entire WCLL TBM mock-up. In future numerical simulations, the mesh will be refined and the number of CPUs increased to predict MHD flows under stronger magnetic fields to approach fusion relevant operating conditions. A comparison with upcoming experimental data will allow to further validate the code and the numerical procedures.

Bend flows in non-uniform magnetic field

In recent years, a number of studies on pressure driven and buoyant MHD flows in geometries related to blanket modules and in liquid metal manifolds, increased the understanding of MHD phenomena in liquid metal blankets [8] [9] [5] although the prediction of such flows in complete blanket modules for fusion relevant parameters is still ongoing [10]. On the other hand, only few works considered the MHD flow in supply and return pipelines connecting the blanket modules with the external ancillary systems. Therefore, the liquid metal flows in the pipes which cross the shield that protects the superconducting magnets from neutron radiation-induced damages have been investigated numerically. The supplying pipe features two bends in series that turn the flow first from the radial direction perpendicular to the magnetic field into a direction parallel to the toroidal **B** lines and then back to a perpendicular orientation (Figure 15).

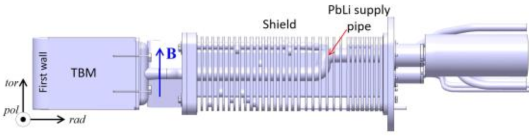

Figure 15 View on the ITER TBM and the PbLi pipes across the shield.

In fully developed MHD flows in straight pipes in uniform magnetic fields, electric currents close within duct cross-sections and remain confined in 2D planes parallel to the magnetic field. In curved bends, potential gradients along the flow path drive currents in 3D loops that traverse different cross-sectional planes. These currents induce electromagnetic Lorentz forces that affect velocity and pressure distribution in the double bend pipe [11, 12]. In the problem under investigation, we consider additionally the influence of spatial variation of the magnetic field along the axis of the pipes.

Model geometry

In Figure 16, the model geometry is displayed together with the coordinate system and the main dimensions taken from the most recent design of a WCLL TBM for ITER and the connecting piping system to the ancillary systems. As for previous numerical studies [11], operating conditions have been provided by *Fusion for Energy* F4E and the data used for the present simulations are summarized in Table 1.

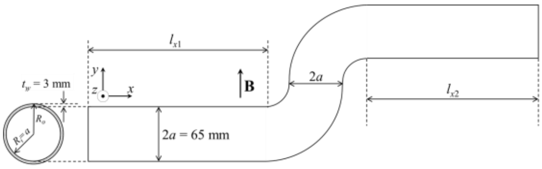

Figure 16 Model geometry used for the numerical analysis, coordinate system and main dimensions.

Table 1 Operating conditions of the WCLL TBM and model dimensions.

a	t_w	$\dot{m}$	u_0	T_{in}	T_{out}	T_0
mm	mm	kg/s	m/s	°C	°C	°C
32.5	3	0.65	$1.99 \cdot 10^{-2}$	295	319	307

Before performing full numerical simulations in the non-uniform magnetic field as present in the shield, initial simulations for uniform fields have been carried out and compared with asymptotic results to test the problem set-up and code performances for such MHD flow. Major findings are briefly summarized and displayed in Figure 17.

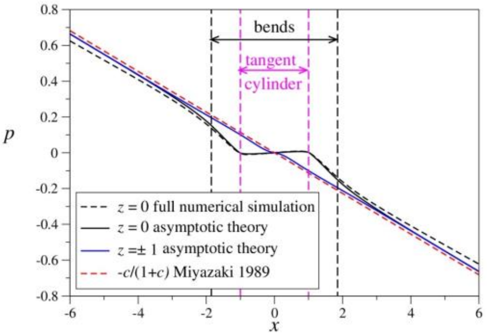

Figure 17 Scaled pressure plotted along the radialdirection for a uniform magnetic field. Solid lines are results from an asymptotic solution valid for large Ha and large N, the dashed lines are obtained by full numerical simulations for N=5104.

Asymptotic results (black solid line) and numerical simulations (black dashed line) yield quite good agreement for pressure variation in the 3D region of the geometry. We find increased pressure gradients before and after the bends as well as a weak, locally reversed pressure gradient in the middle of the bends inside a virtual tangent cylinder. 3D numerical simulations give slightly smaller pressure gradients in fully developed flow regions. This can be explained by the fact that the asymptotic analysis used a definition of the wall conductance parameter according to Walker [13] that applies best when walls are very thin. Since the full numerical simulation is not based on such assumption and resolves the finite thickness of the wall with a fine grid, results obtained by numerical simulations should be more accurate.

For applications in ITER, the magnetic field across the shield is not uniform and its radial distribution is plotted in Figure 18. The solid lines indicate the distribution of the toroidal magnetic field at different poloidal positions, as provide by F4E. The red dashed line is obtained by fitting the curves and this distribution is used for the numerical simulations. In order to reduce the length of the computational domain and to facilitate the definition of boundary conditions, it is assumed that the magnetic field is constant in a certain portion of the inlet and the outlet pipes at sufficient distance from the bends whose middle plane is located at $x=2.369\text{m}$. The position of the model geometry in the spatially varying magnetic field and colored contours of $\boldsymbol{B}$ are shown in the subplot on the top left of the figure.

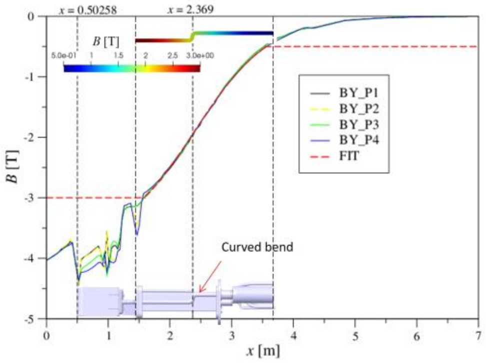

Figure 18 Radial distribution of the magnetic field. Solid lines represent the distribution of the toroidal magnetic field at different poloidal positions, as provided by F4E. The red dashed line is a fitting curve used for numerical calculations. Contours of magnetic field strength in the model geometry are shown in the subplot on the top left side of the figure to indicate the position of the bends.

Numerical results

In the following, results are presented for the geometry described in Figure 16 and the magnetic field distribution as plotted in Figure 18. We consider a curved pipe with a radial-toroidal-radial orientation, which transports the liquid metal from the region with large magnetic field, i.e. from the blanket, towards the ancillary systems where $\boldsymbol{B}$ is much smaller.

Figure 19 shows contours of velocity magnitude (a) and radial velocity (b) on the radial-toroidal symmetry plane at $z=0$. The strongest velocity gradients occur across a thin layer that develops along magnetic field lines tangent to the wall in the middle of the double bend. Together with the boundary layers, it forms a virtual cylinder, marked by the red dashed line, in the periphery of which the 3D MHD phenomena are mainly confined. Contours of the radial velocity component (Figure 19b) clearly show that the fluid domain splits in 3 cores: the ones upstream and downstream of the bends have similar characteristics, the velocity distribution is pretty uniform resembling the main features of a fully developed velocity profile. In the middle core the velocity in the center reduces while the largest portion of the flow rate is transported by the boundary- and internal layers where high velocity jets are present.

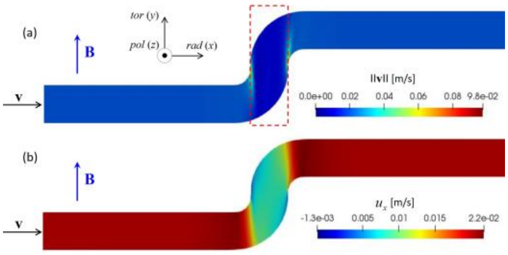

Figure 19 Results for $Ha=2621$ and $N=1318$. Contours of velocity magnitude (a) and radial velocity (b) on the radial-toroidal symmetry plane $z=0$. The red dashed region marks the virtual cylinder.

The evolution of the velocity distribution and the progressive growth of the velocity in the layers can be seen in Figure 20 in which 3D velocity profiles, colored by the velocity magnitude, are plotted at different cross sections along the flow path. For better visualization, some profiles in the curved bend have been presented in two separated views.

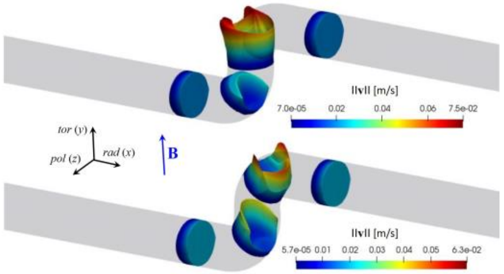

Figure 20 Results for $Ha=2621$ and $N=1318$. 3D velocity distribution at different positions along the flow path. When approaching the bends the velocity start increasing in the boundary layers while reducing in the center. For better visualization, the four profiles in the bends have been presented in separated views. Two different color scales are used for the velocity profiles.

In Figure 21a, colored contours of electric potential are plotted on the fluid-wall interface. The strongest gradients in radial direction are localized near the virtual cylinder indicated by the red dashed lines. Moderate radial potential variations are present in the straight pipes caused by the radial profile of the magnetic field. Only in the regions where the magnetic field is assumed constant and fully developed conditions are imposed at entrance and exit, the potential is constant too and it keeps the same value along magnetic field lines with changes in transverse direction. Figure 21b. shows radial profiles of electric potential in the center of the geometry ($z/a=0$) and near the sides ($z/a=\pm1$). Highest values of potential magnitude are found near the sides in the inlet duct, where the electric potential scaled by $\phi_0=u_0Ba$ is $\phi/\phi_0(x=\infty,z/a=\pm1)=\pm0.894$ in agreement with predictions for fully developed pipe flow [14]. When approaching the bends, a significant reduction of the magnitude of wall potential can be observed near the sides at $z/a=\pm1$. In Figure 21b, cross-sections at positions P1 and P2 indicate the beginning and the end of the bends (see same figure on the right).

Variations of electric potential along the radial coordinate drive 3D currents that close through the wall and the fluid giving rise to additional Lorentz forces that affect velocity and pressure distribution. In the identified virtual cylinder, the 3D currents close exclusively in the fluid domain.

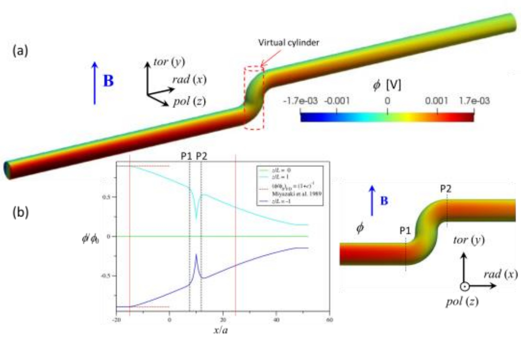

Figure 21 Results for $Ha=2621$ and $N=1318$. Contours of electric potential (a), and radial variation in the center of the geometry ($z/a=0$) and near the sides ($z/a=\pm1$) (b). The figure on the right shows the beginning (P1) and the end (P2) of the bends. The two vertical red lines indicate the length of the shield.

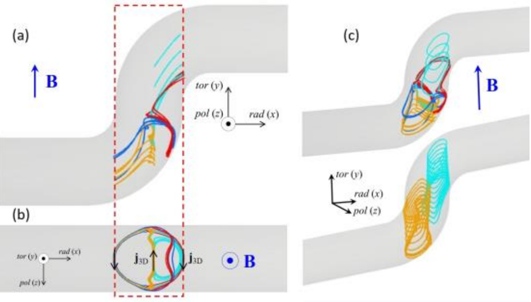

Figure 22 Results for $Ha=2621$ and $N=1318$. Electric current streamlines that close exclusively in the fluid. The red dashed line indicates the virtual cylinder.

In Figure 22, some characteristic current streamlines are displayed. Side (a), top (b) and 3D (c) views should facilitate the understanding of the current paths. The orange and cyan lines form two poloidal tubes, as visible in Figure 22c on the bottom, which meet almost in the center of the virtual cylinder. In the lower part of the bends, there are current lines that circulate across the entire cross-section of the cylinder (blue lines) and in the right half, the red lines move partly along the bend wall and then upstream forming larger loops. When seeding current streamlines outside the virtual cylinder, currents induced in the fluid start closing their path through the wall too. In the straight pipes, the 3D MHD effects are much weaker than in the bends.

The variations of pressure along lines in the center of the model geometry at $z/a=0$ and near the sides at $z/a=\pm1$ are plotted in Figure 23. The pressure has been scaled by the quantity $p_0=\sigma u_0 B^2 a$. The two vertical dashed lines indicate the size of the shield behind the ITER TBM. In the subplot on the right, the distribution in the center of the model geometry has been enlarged for better visualization. Solid lines are results obtained by an asymptotic approach valid for $N\rightarrow\infty$, i.e. for very intense magnetic fields, where inertia forces are negligible compared to electromagnetic forces, while the dashed lines are from full numerical simulations.

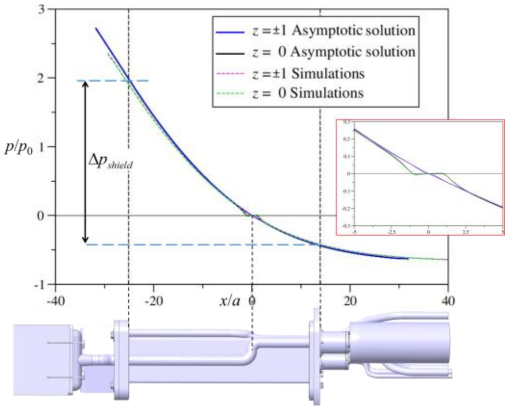

Figure 23 Results for $Ha=2621$ and $N=1318$. Scaled pressure plotted along the radial direction. In the right subplot, the bend region has been enlarged for better visualization. Solid lines are results from an asymptotic solution valid for $N\rightarrow\infty$ and the dashed lines are obtained by full numerical simulations.

In Figure 23, the coordinate system has been chosen such that the center of the curved bends is at $x=0$ in order to compare calculations with the asymptotic data. Close to the inlet and the outlet, where the magnetic field is constant, the flow reaches fully developed conditions characterized by constant pressure gradients. When the magnetic field $B(x)$ starts reducing along the main flow direction from the maximum value $B_{max}=3\mathrm{T}$, the magnitude of the pressure gradient reduces progressively while approaching the bends. In the symmetry plane of the model geometry at $z/a=0$ near the end of the inlet straight pipe the pressure gradient starts increasing and after reaching a maximum it becomes smaller and smaller and even slightly reversed in a narrow region around the center of the bends in the tangent cylinder. This faster radial variation of the pressure is due to the occurrence of 3D currents (see Figure 22) that create additional electromagnetic Lorentz forces, which modify locally the pressure distribution. Near the sides at $z/a=\pm1$, 3D MHD effects are weaker than in the middle of the pipes since transverse Lorentz forces compensate the stronger radial gradients in the center. The presence of the bends causes significant 3D MHD effects that remain confined to the region immediately around the bends and affect mainly the velocity distribution.

MaPLE inauguration

MaPLE (Magnetohydrodynamic PbLi Experiment) is a facility to investigate, multi physics effects and in particular the interaction of the PbLi flow with strong magnetic fields present in fusion applications. The focus of future experiments is on free, forced and mixed convection flows with heat transfer. MaPLE has been built in the US at UCLA [15] and it was substantially upgraded with contributions from EUROfusion. The facility has been moved to KIT in 2021/2022 and recommissioned as a EUROfusion facility open to partners in breeding blanket development. On October 14th 2022, the Festive Colloquium and EUROfusion Use Planning Meeting has been held at KIT for the recommissioning of the MaPLE facility at KIT. The colloquium was attended by international scientists as well as European representatives, demonstrating the interest of the fusion community in the R&D activities to be carried out. MaPLE will support European scientists in understanding MHD phenomena in connection with heat transfer in liquid metals and it will enhance the verification & validation of the numerical codes used for studying these issues.

MaPLE will support and strengthen the development of breeding blankets for DEMO or test blanket modules for ITER by increasing the confidence and reliability of results.

Figure 24 Visit of MaPLE as part of the Inauguration Colloquium at KIT.

Further work

Support of HCPB design activities

Within the EUROfusion Work Package Breeding Blanket BB.S.02.01-T001, R&D activities were carried out for a preliminary conceptual design of a helium-cooled pebble bed (HCPB) blanket for a DEMO reactor, where granular lithium ceramics are used as breeder material. The design activities have been supported by ITES in terms of developing a full 3D reactor segment for inboard and outboard blankets. The work extends previous achievements for a central outboard blanket (COB) and left inboard blanket (LIB) segment, which were initially designed as sliced modules with short poloidal extent as shown in Figure 25.

The present concept is based on an arrangement of fuel-breeder pins, consisting of concentric tubes forming respectively the inner and outer cladding, arranged in a periodic pattern (see Figure 25, bottom). The volumes inside the pins are filled with the Advanced Ceramic Breeder (Li_4SiO_4 and Li_2TiO_3) pebbles and closed at the back by filter plates. The pins are surrounded by titanium beryllide blocks ($Be_{12}Ti$) acting as neutron multiplier. The first wall facing the plasma is 25 mm thick and actively cooled by helium at a pressure up to 8 MPa. The wall is coated with 2 mm thick functional graded materials of tungsten and Eurofer97 as protection against plasma erosion by fast particles. The helium purge gas and coolant is distributed to the breeder zones by manifolds formed by a series of parallel plates in the back. Additional stiffening plates are required to provide sufficient mechanical strength of the structure at high pressure. A detailed description of the HCPB concept can be found at [16, 17].

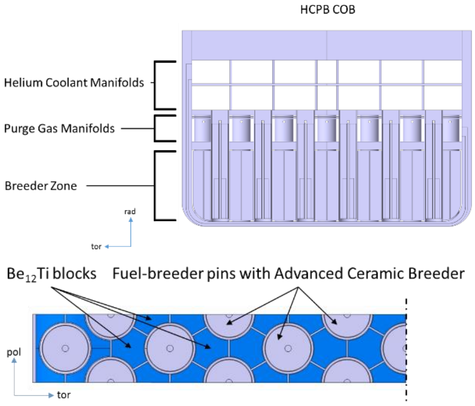

Figure 25 Toroidal-radial view of HCPB COB sliced module (top); toroidal-poloidal pattern of the breeder pins embedded in $Be_{12}Ti$ blocks (bottom).

The development of IB and OB full 3D segments is based on the radial build-up of the sliced COB and LIB modules, the FW contour consisting of poloidal straight segments enclosing the plasma (see Figure 26, left) and the partitioning of segments per 22.5° reactor segment (see Figure 26, right).

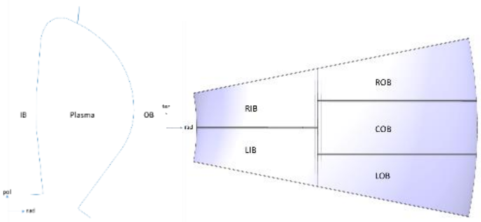

Figure 26 Poloidal-radial view of the first wall contour around the plasma (left); toroidal-radial view showing the partitioning of IB and OB segments per 22.5° reactor segment (right).

Starting from the FW, the boundaries of all following walls were built-up with the given dimensions. The radial setups of the LIB and COB modules have been toroidally extended not rotated, so that plane surfaces (sections) in poloidal-toroidal direction could be formed. With this strategy, all outer walls of the full segments have be designed as shown in Fig. 27.

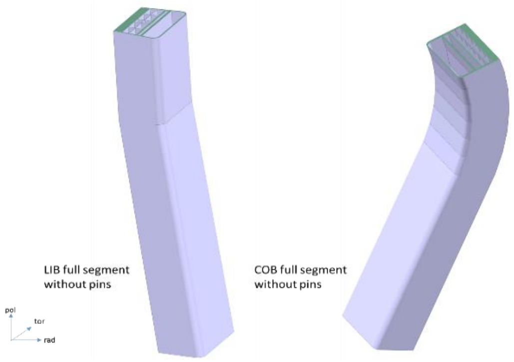

Figure 27 Sectional view of a lower part of LIB and COB segments without pins.

The distribution of the breeder pins starts with a perpendicular orientation from the first wall. Each section of a segment is filled with pins individually to achieve the densest packing factor. The distribution of breeder pins in the full 3D segments can be seen in Figure 28. In this conceptual design, there are in total 954 breeder pins in the LIB and 1469 pins in the COB segment. The elements forming a LIB and COB segment have been designed in quite detail for the breeder zones with all pins, purge gas manifolds, and helium coolant manifolds.

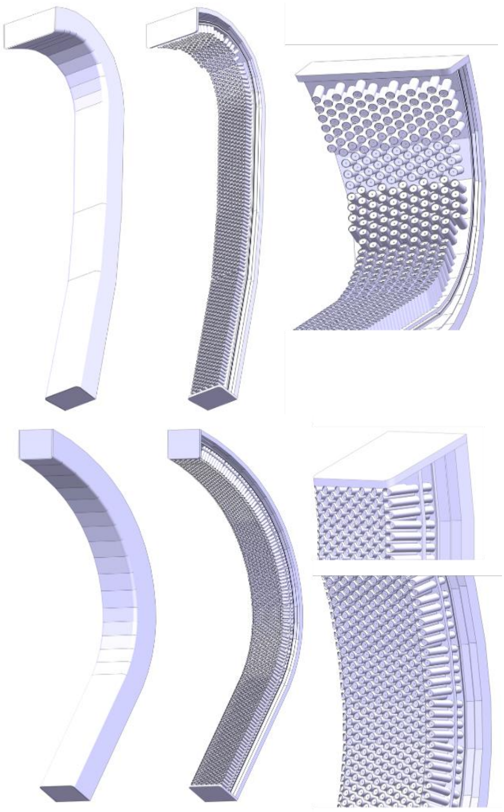

Figure 28 Full 3D LIB (top) and COB (bottom) segments with fuel breeder pins.

Additional work not mentioned in detail in this report

In addition to the topics described above, the MHD group at ITES KIT contributed with scientific papers to blanket-relevant MHD topics in [18, 19, 20, 21, 22, 23].

References

[1] Koehly, C., Bühler, L. and Courtessole, C., "Design of a scaled mock-up of the WCLL TBM for MHD experiments in liquid metal manifolds and breeder units," *Fusion Engineering and Design,* vol. 192, p. 113753, 2023.

[2] Mistrangelo, C., Bühler, L. and Brinkmann, H.-J., "Experimental investigation of MHD pressure losses in a mock-up of a

liquid metal blanket," *Nuclear Fusion,* vol. 58, p. 036012, 2018.

[3] Mistrangelo, C., Bühler, L., Koehly, C. and Ricapito, I., "Magnetohydrodynamic velocity and pressure drop in manifolds of a WCLL TBM," *Nuclear Fusion,* vol. 61, p. 096037, 2021.

[4] Aubert, J., et al., "Design and preliminary analyses of the new Water Cooled Lithium Lead TBM for ITER," *Fusion Engineering and Design,* vol. 160, p. 111921, 2020.

[5] Bühler, L. and Mistrangelo, C., "A simple MHD model for coupling poloidal manifolds to breeder units in liquid metal blankets," *Fusion Engineering and Design,* vol. 191, p. 113552, 2023.

[6] Mistrangelo, C., Bühler, L. und Klüber, V., „Towards the simulation of MHD flow in an entire WCLL blanket mock-up,“ in *32th Symposium on Fusion Technology SOFT, Dubrovnik, Croatia, September 18-23, 2022*, 2022.

[7] Mistrangelo, C. and Bühler, L., “Determination of multichannel MHD velocity profiles from wall-potential measurements and numerical simulations,” *Fusion Engineering and Design,* vol. 130, pp. 137-141, 2018.

[8] Yan, Y., Ying, A. and Abdou, M., “Numerical study of magneto-convection flows in a complex prototypical liquid-metal fusion blanket geometry,” *Fusion Engineering and Design,* vol. 159, p. 111688, 2020.

[9] Chen, L., Smolentsev, S. and Ni, M.-J., “Toward full simulations for a liquid metal blanket: MHD flow computations for a PbLi blanket prototype,” *Nuclear Fusion,* vol. 60, no. 7, p. 076003, 2020.

[10] Mistrangelo, C., Bühler, L. und Klüber, V., „Towards the simulation of MHD flow in an entire WCLL blanket mock-up,“ *Fusion Engineering and Design,* vol. 193, p. 113752, 2023.

[11] Bühler, L., Klüber, V. and Mistrangelo, C., "Magnetohydrodynamic flow in stepwise bent circular pipes," in *Proceedings of the 12th PAMIR International Conference Fundamental and Applied MHD, Krakow - Poland, July 4 - 8*, 2022.

[12] Bühler, L., Klüber, V. and Mistrangelo, C., "Magnetohydrodynamic flow in stepwise bent circular pipes," *Magnetohydrodynamics,* vol. 58, no. 4, pp. 339-347, 2022.

[13] Walker, J. S., “Magnetohydrodynamic flows in rectangular ducts with thin conducting walls,” *Journal de Mecanique,* vol. 20, no. 1, pp. 79-112, 1981.

[14] Miyazaki, K., Nakano, M., Horiba, T., Inoue, S. and Yamaoka, N., “MHD pressure drop along a NaK flow around a stepwise change of tube diameter under a transverse magnetic field,” *Fusion Engineering and Design,* vol. 8, pp. 233-239, 1989.

[15] Smolentsev, S., Li, F.-C., Morley, N., Ueki, Y., Abdou, M. and Sketchley, T., "Construction and initial operation of MHD PbLi facility at UCLA," *Fusion Engineering and Design,* vol. 88, pp. 317-326, 2013.

[16] Zhou, G., "Status of design activities of the DEMO Helium Cooled Pebble Bed breeding blanket in Europe," in *Presentation at Technology of Fusion Energy (TOFE 2022), 12.--16. Juni 2022*, Anaheim, CA, USA, 2022.

[17] Zhou, G., Kang, Q., Hernandez, F., D'Amico, S. and Kiss, B., "Thermal hydraulics activities for consolidating HCPB breeding blanket of the European DEMO," *Nuclear Fusion,* vol. 60, no. 9, p. 096008, 2020.

[18] Mistrangelo, C., "Development of predictive tools to simulate MHD flows under strong magnetic fields: study of MHD flows to support the WCLL BB design," EUROfusion, BB.S.04.01-T001-D001, 2022.

[19] Courtessole, C., Brinkmann, H.-J. and Bühler, L., "Experimental investigation of magneto-convective flows around two

differentially heated cylinders" *Journal of Fluid Mechanics*, p. accepted, 2024.

[20] Bühler, L., Courtessole, C. and Mistrangelo, C., "Magnetohydrodynamic flows in strong magnetic fields for application in fusion blankets," *Invited presentation at 12th PAMIR International Conference Fundamental and Applied MHD, Krakow - Poland, July 4 - 8*, 2022.

[21] Bühler, L., Lyu, B., Brinkmann, H.-J., Courtessole, C., Klüber, V., Köhly, C., Mistrangelo, C. and Roth, J., "Magneto-hydrodynamics for liquid metal blankets," in *Annual Report 2021 of the Institute for Thermal Energy Technology and Safety*, W. Tromm, Ed., Karlsruhe Institute of Technology, 2022.

[22] Mistrangelo, C., Bühler, L., Brinkmann, H.-J., Courtessole, C., Klüber, V. and Koehly, C., "Magneto-convective flows around two differentially heated cylinders," *Heat and Mass Transfer,* vol. 59, p. 2005-2021, 2023.

[23] Courtessole, C., Brinkmann, H.-J. and Bühler, L., „Relaminarization of magneto-convective flow around a pair of submerged differentially heated cylinders,“ *Presentation at 9th International Symposium on Bifurcations and Instabilities in Fluid Dynamics, Groningen, Netherlands, August 16-19, 2022*.

Department: Severe Accident Research

SAR research activities in 2022

B. Fluhrer, X. Gaus-Liu, T. Cron, R. Stängle, Th. Wenz and M. Vervoortz

In 2022, the SAR team worked on one hand for tasks within the European projects ESFR-SMART and ESFR-SIMPLE that empower the design maturity of safe and economical European Sodium-Cooled Fast Reactor, on the other hand intensively on the design and control concept of HELOKA-US facility (HELOKA-Upgrade Storage) within the EUROfusion BOP (Balance of Power) program.

European projects within severe accident research: ESFR-SMART and ESFR-SIMPLE

The European ESFR-SMART Horizon 2020 project has been completed at the end of August 2022. In the last months of this project, the SAR team has been mainly working on several documentations and publications [1].

After completion of the EU Horizon 2020 ESFR-SMART project, a follow-up project, ESFR-SIMPLE (European Sodium Fast Reactor - Safety by Innovative Monitoring, Power Level flexibility and Experimental research) has been approved upon HORIZON-EURATOM call, which started in October 2022. The new project has the main objective to improve the safety and economics of the Generation IV ESFR, which paced on the achievements in the ESFR-SMART project.

The SAR team leads the work package 6 “Advanced components for passive safety”, and is mainly involved in Task 6.2, in which the safety concepts of an in-vessel metallic core catcher shall be evaluated. The main objective in this task is to minimize the core catcher ablation by corium jet impingement from the transfer tubes in the initial stage of a severe accident as well as the long-term ablation by a molten pool. The new experiments foreseen in the ESFR-LIVE test facility at KIT shall validate long-term ablation behavior of the innovative concepts. Three different test series are planned to investigate the influence of ablation cavities, resulting from the short-term jet impingement on the core-catcher, and to investigate the presence of reinforcement pods inside the corium pool on the long-term ablation of the core catcher. First discussions on the experimental campaigns has been started in 2022. In 2023 it is planned to accomplish the final definition and to start with the preparations for the experiments.

HELOKA—Upgrade Storage – Experimental Demonstration of the He-cooled DEMO Balance of Plant

Introduction

HELOKA-US is a new-build infrastructure to demonstrate the operational capabilities of the Intermediate Heat Transfer System (IHTS) of the Helium Cooled Pebble Bed (HCPB) DEMO reactor design developed under the EUROfusion Horizon Europe program. In Fig. 1 a schematic layout of the design of the Indirect coupling design of the HCBP DEMO reactor is shown.

The IHTS system with two tanks for the ESS (Energy Storage System) decouples the intermittent pulsed fusion thermal power output to a constant usable thermal power feeding the Power Conversion System (PCS). The operational mode of DEMO is a repeated sequence of a pulse state (about 2 hours) and of a dwell state (about 10 minutes).

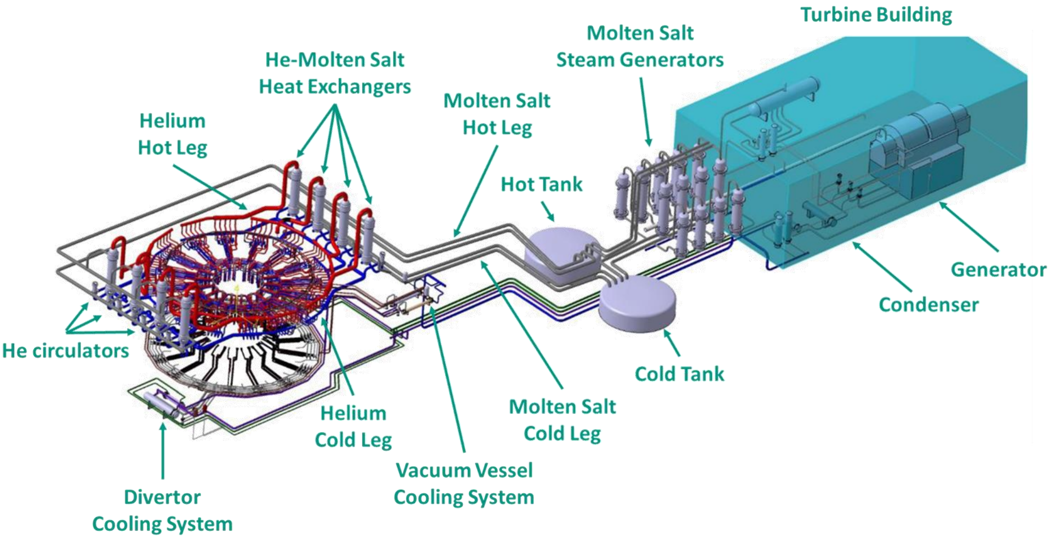

Figure 1: Layout of the design of the ICD design of HCBP DEMO reactor [2].

A scaling factor of 1:1000 for the power level of one of the eight Primary Heat Transfer System (PHTS) circuits of DEMO has been selected for HELOKA-US corresponding to 260 kW of nominal power. Molten Salt HITEC shall be used as the heat transfer fluid in the IHTS.

The main objectives of HELOKA-US project are:

1. To study relevant phenomenology of interest for the design of components relevant for the HCPB Indirect Coupling Design variant of Balance of Plant.
2. To demonstrate that the IHTS is able to handle power pulses and dwell phases having time characteristics similar to the HCPB DEMO design.
3. To provide a testing facility for developing and qualifying specific technological components like the helium/molten salt heat exchanger (He/MS HX).

The HELOKA-US project will be realized in 2 phases, which have different subtasks. In Phase 1a, the scaled Molten Salt (MS) loop will be designed, constructed and commissioned using the molten salt HITEC (an eutectic of $NaNO_3$-$NaNO_2$-KNO_3) as heat transfer and storage medium. The MS loop mock-up will then tested and operated in different operational states (Phase 1a-1). In a next step, test sections of relevant geometry for He/MS HX for the molten salt side will be investigated (Phase 1a-2) and in Phase 1a-3, a scaled He/MS HX will be integrated in the MS loop. Phase 1b will connect the MS loop to HELOKA-HP, that simulates the primary loop of a Helium cooled DEMO reactor for smooth steady state and smooth transient investigations. Phase 2 will construct a new He loop equipped with an improved helium blower compared to existing HELOKA-HP and connection to the MS loop by the He/MS heat exchanger to be able to perform fast end representative operational transients.

Realization of Phase 1a-1

The HELOKA-US facility will integrate the existing HELOKA infrastructure and LIVE infrastructure in one operational site. Figure 1 shows the concept of integration of HELOKA-US with the existing facilities in Phase 1a. The systems in green are existing facilities and components and systems in red are new ones.

The MS loop (named as ES loop in HELOKA-US) and the N2 gas system will be erected. The ES loop will be coupled with the existing HELOKA-WHT loop (high pressure water loop) by a MS/water heat exchanger. The WHT loop acts as the heat sink of the ES loop. The WHT loop is then coupled with an on-site water loop at ambient pressure (HELOKA-WCS) to transfer the heat from WHT to the atmosphere.

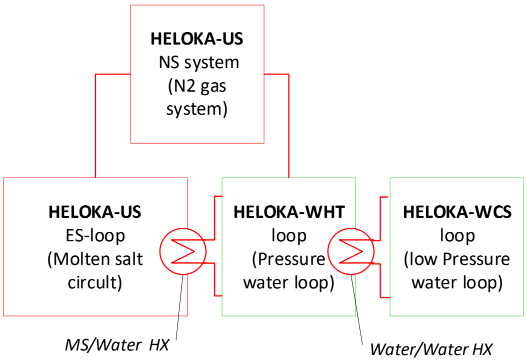

Figure 2: HELOKA-US Phase 1a concept on the integration of existing systems.

The heating source in Phase 1a is an electrical heater. The ES loop includes two tanks and three MS bypasses to enable flexible control of MS temperature and flow rate. The ES loop has the following functions:

- To transfer the energy continuously to the heat sink which is the WHT system. The WHT loop mimics the Power Conversion System in DEMO.
- To store about 10 % of the thermal energy during pulse operation for releasing it during dwell operation.
- To maintain the helium temperature of the PHTS during dwell operation at the outlet of the He/MS HX constant. The power generation during dwell is only about 1 % of the pulse operation, so only a very small stream of molten salt from the cold tank is directed through the He/MS HX.

The HELOKA-US facility will also be connected with a pressure nitrogen system for providing cover gas to the two tanks serving as pressure control gas in the ES-loop and as stabilization medium of the HITEC chemical.

Figure 2 shows a preliminary Pipe / Instrumentation diagram (PID) of the ES loop and an implied NS system within the two dashed lines marking the boundary to the PHTS foreseen on the left side in Phase 1b and to the water cooling system WHT at the right side.

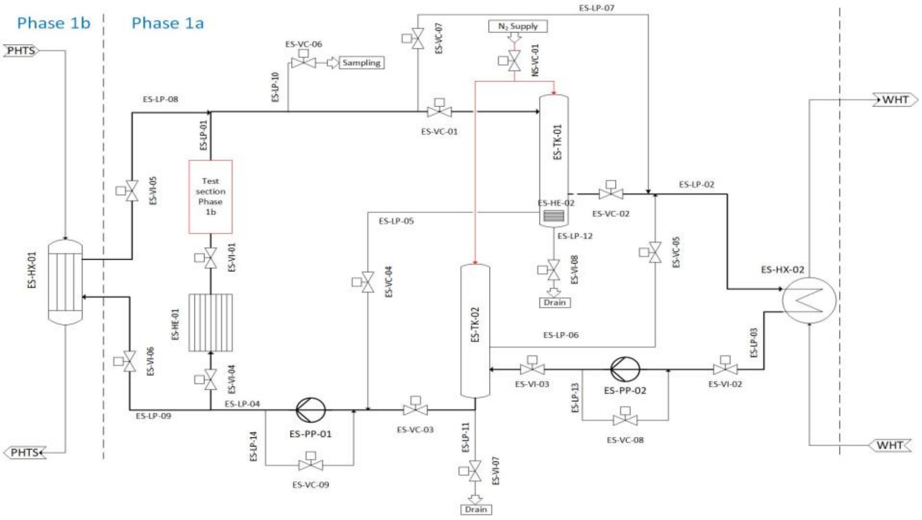

Figure 3: Preliminary PID of the ES loop.

The design power of HELOKA-US is 260 kW corresponding to ~1/1000 of one of the eight DEMO HCPB IHTS circuits. The durations of pulse and dwell are the same as in DEMO power cycle. The requirement on the MS operational temperature at the inlet of ES-HE-01 (270 °C) is to represent the MS inlet temperature of DEMO He/MS HX (IHX in DEMO reactor) for an adequate cooling of He outlet temperature to 290 °C in the IHX. The boundary conditions of HELOKA-US are summarised in Table 1.

Table 1 Boundary conditions of HELOKA-US ES loop

	Pulse	**Dwell**
Power of ES-HE-01, kW 1)	260	2.6
Duration, s2)	7200	600
ES-HE-01 MS side in / out temp. °C 2)	270/465	270/299
ES-HX-02 MS side inlet/outlet temperature, °C 2)	465 / 270	465 / 270
ES-HX-02 water side inlet/outlet temperature, °C 3)	160 / 220	160 /220

1) Designed power level of HELOKA-US facility
2) Requirement from DEMO IHTS system
3) Preliminary requirement of WHT system

The HELOKA-US molten salt loop shall represent the DEMO IHTS concept in maximal possibility in all described operational phases. The operation of the HELOKA-US ES loop is divided into non-power generation modes and operational modes. The operational modes include the pulse and dwell states and the transients between them (100 sec of each). With the completion of Phase 1a-1, HELOKA-US shall be able to simulate all states and transients in non-power as well as in power generation modes. Operational states and transients have been defined for Phase 1a-1, Figure 4. The states are indicated in rectangle, whereas the transients are indicated by line arrows. Red line arrows are temperature upward ramps, whereas blue arrows are temperature downward ramps.

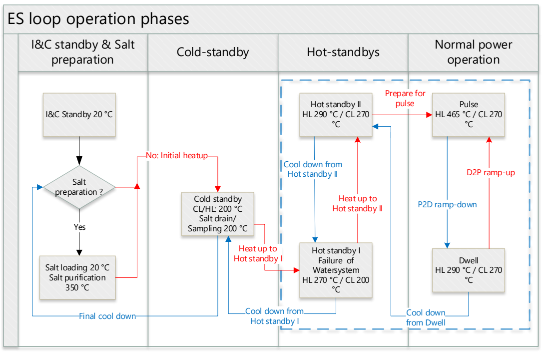

Figure 4: Operational states and transients in HELOKA-US.

In 2022, the work within the HELOKA-US project was mainly concentrated on the following topics:

- Preparatory works in order to provide the area for the new platform and to provide the necessary infrastructure for HELOKA-US operation such as heating, lighting, arrangement of work areas, compressed-air supply lines, power supply.
- Construction of a new platform for HELOKA-US in the experimental hall 660 (s. Figure).
- Definition of a preliminary PID diagram and definition of operational states for HELOKA-US.
- Completion of a technical specification for a tender offer and starting a call for tenders.

In 2023, it is planned to place an order for constructing the HELOKA-US test facility as described above. The detailed design and engineering phase for HELOKA-US will then be started together with the contractor.

Figure 5: Overview of the new platform.

References and publications

[1] Gaus-Liu, X., Bigot, B., Journeau, C., Payot, F. , Cron, T., Clavier, R., Peybernes, M.; Angeli, P. E., Fluhrer, B.; “Experiment and Numerical Simulations on SFR Core-catcher Safety Analysis after Relocation of Corium”, 10th European Review Meeting on Severe Accident Research (ERMSAR 2022), Karlsruhe, Germany, 16.05.2022 – 19.05.2022

[2] Perez-Martin, S., Bubelis, E., Hering, W., Barucca, L.; „R&D Needs for the Design of the EU-DEMO HCBP ICD Balance of Plant in FP9”, J. Nucl. Eng. 2022, 3, pp 135-445, https://doi.org/10.3390/jne3040029

[3] Fluhrer, B., Gaus-Liu, X., Cron, T., Stängle, R., Vervoortz, M., Wenz, T.; “LIVE-BWR Experiments to Study the Effect of CRGT Cooling on In-Vessel Melt Retention Strategy”, 19th International Topical Meeting on Nuclear Reactor Thermal Hydraulics (NURETH-19), Brussels, Belgium, March 6 - 11, 2022

[4] Gaus-Liu, X., Cron, T., Bottomley, D., Fluhrer, B.; “MCCI on Siliceous and LCS Concrete with Oxide and Metallic Melt: Re-Evaluation of MOCKA Experiments”, 19th International Topical Meeting on Nuclear Reactor Thermal Hydraulics (NURETH-19), Brussels, Belgium, March 6 - 11, 2022

[5] Madokoro, H., Gaus-Liu, X., et.al., “LIVE-J1 Experiment on Debris Melting Behavior Toward Understanding Late In-Vessel Accident Progression of the Fukushima Daiichi Nuclear Power Station”, 19th International Topical Meeting on Nuclear Reactor Thermal Hydraulics (NURETH-19), Brussels, Belgium, March 6 - 11, 2022

[6] Madokoro, H., Yamashita, T., Gaus-Liu, X., Cron, T., Fluhrer, B., Sato, I., Mizokami, S., “The Experimental and Simulation Results of LIVE-J2 Test - Investigation on Heat Transfer in a Solid-Liquid Mixture Pool”, Nuclear Technology, 2022, DOI: 10.1080/00295450.2022.2121545

[7] Gaus-Liu, X., Bubelis, E., Perez-Martin, S., Ghidersa, B.-E., Hering, W.; “Design Features and Simulation of the New-Build HELOKA-US Facility for the Validation of the DEMO Helium-Cooled Pebble Bed Intermediate Heat Transport and Storage System”, J. Nucl. Eng. 2022, 3, pp. 461–472, https://doi.org/10.3390/jne3040032

Department: Multiphase Flow

Construction of the COSMOS-H high-pressure test facility

Stephan Gabriel, Wilson Heiler, Giancarlo Albrecht, Felix Heineken, Nicolas Wefers

In 2022, the activities of the department of multiphase flows focused on the completion of the experimental facility COSMOS-H in addition to further projects. In operation, the high-pressure loop will enable the investigation of thermal-hydraulic topics such as heat transfer during flow boiling including to boiling crisis under 1:1 power plant conditions. COSMOS-H consists of a high-pressure water/steam loop with a thermal power of approx. 1.2 MW, which can reach an operating pressure of up to 160 bar and an operating temperature of up to 360°C. The cooling system consists of two cooling loops with a thermal output of approx. 2 MW, a 600 kW electrical heating power for the test section and a comprehensive measurement and control system. A modular test track system was developed for the first series of experiments in the Project McSAFER [1] at COSMOS-H. The facility can thus be used to investigate various issues in thermal energy technology and its design enables new measurement technology and test setups to be flexibly integrated into the system.

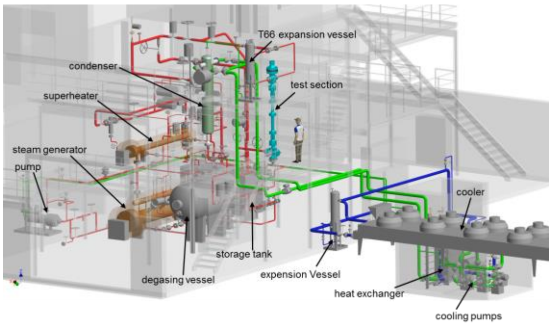

Figure 1: CAD for piping and steel construction of the entire COSMOS-H system

Over the past few years, a lot of time has been invested in the design, optimization and detailed construction of the system. In 2021, the design was completed with regard to both the hydraulics and the mechanics of the pipe performance system, the apparatus and the steel structure, and the proof of function was provided. This was done on the one hand using extensive simulations with a system code [2] and in the dynamic thermo-mechanical CAE System Rohr2. After around 14 months of construction, the optimized piping construction of the high-pressure circuit, including the associated steel structure with over 80 pipe supports, was completed in spring 2022.

Once the high-pressure circuit had been completed, the focus was on setting up and commissioning all other subsystems of the plant as well as the measurement and control technology. As all the equipment and pipe connections were now in place, many of the processes already prepared for setting up the measurement and control technology and other subsystems were be completed.

Figure 2: Installing the power supply for the test track

The powerful components of the high-pressure loop, such as the cooler and steam generator as well as the steam superheater, which were procured by COSMOS-H at the start of construction, were maintained and tested on tightness and functionality by the manufacturers to ensure smooth operation for the commissioning and acceptance tests.

As part of the safety concept, the system, whose test section includes high-pressure sight glasses, is controlled from a control room located outside to the building in order to ensure that operating personnel do not need to remain in the danger zone of the heated pressure vessel system during operation. The construction of the control room had already been initiated in 2021 and made considerable progress in summer 2022 with the installation of the container building next to Building 428. The control system was then relocated from the internal control room in building 428 to this external container building and all the necessary cable connections were established. Once the necessary connections had been completed, the software for the control system and the test

Figure 3: Assembly of the external cooler (top) and the steam generator (bottom) after maintenance before commissioning

section control software were installed and the first cold function tests were carried out.

Figure 4: Construction and completion of the external control room

As the strength test had to be carried out at ambient temperature, i.e. at 20°C, the system had to be prepared for a test pressure of 328 bar. This corresponds to the mechanical material load at 160 bar and 360°C. The preparation included the removal of all sensors that could not withstand this pressure and the application of two high-pressure pumps connected in series, which had to apply the test pressure after filling and closing the high-pressure loop. First, the high-pressure loop with a volume of approx. 3.5 m³ was pressurized in steps of 100 bar each and after each step the steady state and thus the tightness of the system was inspected. In addition to the expected smaller leaks at nozzles and flanges, a larger leak occurred at a pressure of approx. 260 bar at the lower test section connection, which reduced the system pressure down to 50 bar again before the corresponding valves were closed after approx. 20 seconds. The source of this leak was a misalignment of the system-side flange (DN65 PN320) by approx. 8 mm in relation to the vertical position. This manufacturing defect was quickly rectified by a specialist company and the strength test was restarted. On May 16, 2022, the high-pressure circuit reached 329.45 bar at the lowest point of the system during the official pressure test and withstood this for over an hour without any leaks. The strength of the system was thus officially verified by an inspector. The further tests based on the design documents were also successfully completed by fall 2022.

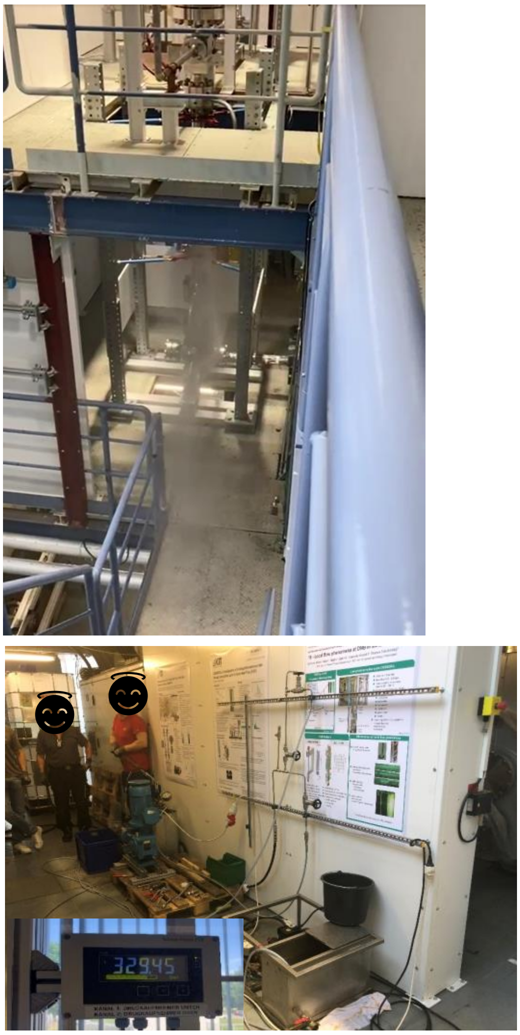

Figure 1: Preparation of the system for the pressure test. Right: High-pressure pump and pressure measurement technology for the application of the test pressure, left: Snapshot of the leak at the lower test section flange at approx. 250 bar

Figure 2 Top: The top floor of the facility with the top of the test track in the foreground. Below Ground floor(l) and 1st floor(r) of the COSMOS-H facility

The high-pressure loop was thus completed. The next step was to attach the sensors and safety valves that had previously been removed for the pressure test. Most of these had already been connected to the control system and calibrated before the pressure test, so the screw connections had to be tested. Due to the expected pressures and temperatures, the screwing was torque-controlled and the rotational angle was monitored and documented using a hydraulic unit.

By the end of the year, the trace heating of the high-pressure loop was applied to the system, followed by the entire thermal insulation of the system and the test section. At the same time, the final subsystems, such as the leakage detectors for the oil cooling circuit, were installed. Then the cold function tests were started. The housing was closed and all safety systems were set into operation. By the end of 2022, the hardware of COSMOS-H was fully completed and all cold tests had been completed.

For 2023, however, numerous further steps remain before experimental operation, such as the parameterization of the controller systems under hot plant conditions and the acceptance tests of the main safety functions.

Literature:

[1] Sanchez-Espinoza, Victor Hugo, et.al.: The H2020 McSAFER Project: Main Goals, Technical Work Program, and Status, *Energies* **2021**, *14*(19), 6348, https://doi.org/10.3390/en14196348

[2] Sean Lapuk: Control Optimization of Thermal Hydraulic Test Facility COSMOS-H by Simulation with APROS 6, Master Thesis, KIT/ITES 2017

Department: Karlsruhe Liquid metal Laboratory (KALLA)

KALLA research in 2022: From heat transfer fundamentals up to high tech carbon from CO_2

Markus Daubner, Benjamin Dietrich, Ines Duran, Frank Fellmoser, Christoph Hofberger, Marta Kamienowska, Ralf Krumholz, Tim Laube, Karsten Litfin, Martin Lux, Franziska Müller-Trefzer, Klarissa Niedermeier, Leonid Stoppel, Neele Uhlenbruck, Thomas Wetzel, Kurt Wittemann

Introduction

In 2022 at Karlsruhe Liquid Metal Laboratory (KALLA) we continued and intensified our efforts in our three strategic focus areas 1) Thermal fluid dynamics of liquid metals, 2) Liquid metal based thermal storage and 3) Liquid metal based process technology. All our work aims at enabling technologies and creating new ideas for the energy transition and for the fight against global warming, with their challenges not only for the energy sector, but for chemistry, transport and the society as a whole.

The following report will provide a short overview of some important steps and results in our various projects, reaching from extending fundamental knowledge all the way up to technological innovations with a clear application perspective. And while we remain dedicated to our goal of being among the research teams defining the state of the art in liquid metal technology in our international environment and community, we know, that we cannot do anything useful just on our own. We therefore remain grateful and work actively for the fruitful and strong partnership with our research partners across Europe and worldwide.

We look forward to working with YOU in future, so if you find an interesting point on the next pages, do not hesitate to get in touch.

Thermal fluid dynamics of liquid metals

GALINKA

The use of liquid metals in solar tower power plants as a heat transfer medium has been discussed for some time. In this process, the concentrated sunlight is transferred to the heat transfer medium in the so-called receiver. The receiver typically consists of a bundle of tubes. The focusing of the sunlight results in an inhomogeneous distribution of heat or temperature over the circumference of the tube. For the thermal dimensioning of the receiver, so-called Nusselt correlations are necessary. In order to obtain these on the basis of experiments, a test facility with a special test section was set up at KALLA in the DFG project (WE 4672/4-1), which allows azimuthally homogeneous (full heating) but in particular also various inhomogeneous boundary conditions to be realized. For reasons of practicability, GaInSn is used as the model fluid. The project ended in 2022, but the continuation application was positively reviewed and another 3 years were granted (WE 4672/4-2). The results of the first phase of the project have been published in [1] [2][3][4], the most important aspects are:

1) Nusselt correlations determined for fully heated, thermally and hydro-dynamically developed liquid metal tube flows are equally suitable for calculating circumferentially averaged Nusselt numbers for liquid metal flows in tubes heated over half of the circumference of the tube. This can be seen in Figure 1, as the data in principle follow very well the trend

of Skupinski's correlation derived for the case of a homogeneous heated liquid metal tube flow.

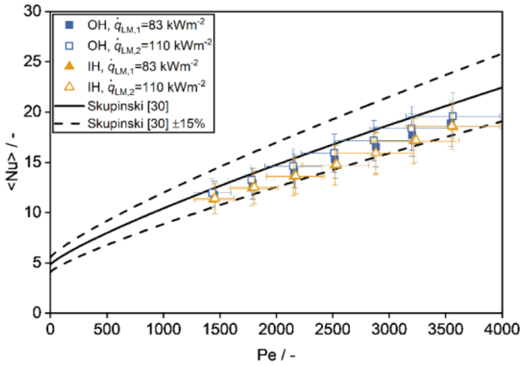

Figure 1: Comparison of the averaged Nusselt-number 〈Nu〉 of experimental date for an azimuthally homogeneous (OH) and inhomogeneous (IH) heated tube with the correlation according to Skupinski et al [5].

2) In the case of liquid metal tube flows, larger temperature differences occur in the tube wall between the heated and unheated halves compared to conventional fluids (e.g. water). This can be explained by the significantly higher convective heat transfer coefficients in liquid metal, as well as the greater influence of the semi-peripheral heating on the local Nusselt numbers than in conventional fluids. This finding is in agreement with theoretical considerations by Flesch [6] and is of high relevance for the design of technical apparatus, since higher thermomechanical stresses can accompany these higher temperature differences. This is a very important aspect, especially for the intended applications with high heat flux densities and temperature levels.

The value of the data obtained in the WE 4672/4-1 project is based, among other things, on the fact that, in contrast to the few data in the literature, precise knowledge of the boundary conditions and measurement uncertainties is available. Thus, a much more reliable design of technical apparatus will be possible in the future. Furthermore, the results support the validation of numerical simulations and the further development of turbulence models for liquid metal tube flows with heat transfer in current work [7][7].

Fuel assembly experiments in Heavy liquid metal flows

Liquid heavy metal such as an eutectic lead-bismuth alloy (LBE) is one of the preferred coolants for the design and operation of modern nuclear reactors such as the MYRRHA (Multi-purpose hYbrid Research Reactor for High-tech Applications) or the Gen-IV reactors. The precise knowledge of the mechanical and thermal properties of the coolant in the reactor core and the fuel elements is of great importance for safe and reliable operation. In addition, the geometry of the fuel assemblies can change during operation due to swelling, creep and mechanical defects and can influence safety. As part of the EU PATRICIA (Partitioning And Transmuter Research Initiative in a Collaborative Innovation Action) and PASCAL (Proof of Augmented Safety Conditions in Advanced Liquid-metal-cooled systems) projects, two experiments in LBE and numerical modelling with CFD were launched at KALLA.

In the first experiment, the influence of a well-defined porous blockade in a 19-pin wire spaced rod bundle will be investigated in the THEADES loop of KALLA. Following the EU project MAXSIMA [8][9][10][11], in which a complete blockage of several subchannels was investigated experimentally and numerically, a realistic partial blockage will be investigated in PATRICIA by using a sintered ceramic element with well-defined porosity. The detailed instrumentation will provide insights into local hot spots as well as recirculation patterns that will be used to validate numerical models.

In a second experimental study, the effect of deformations in a rod bundle on the local flow and temperature field in a 7-pin wire spaced rod bundle is investigated. The rod bundle contains a rotating central rod and bendable outer pins to simulate wire displacements and bent rods in a rod bundle. This experiment is performed in the THESYS LBE loop at KALLA. Another deformation study is being set up as a water rod bundle experiment at the Karman Institute for Fluid Dynamics (VKI) in Brussels as part of the EU PASCAL project. The detailed design of the experiment and blocking is supported by the KALLA team and the CFD analysis after the experiment is performed by FPS (see Figure 2).

Figure 2: Longitudinal cut through the planned rod bundle deformation test section in EU-Project PATRICIA with the deformation piston in the center.

Liquid metal based thermal energy storage

<u>Filler material screening for packed-bed heat storage</u>

Liquid metals have been proposed as heat transfer fluids in high-temperature heat storage systems due to their excellent heat transfer capabilities and large operating temperature range [12]. In 2020 and 2021, a lab-scale packed bed heat storage system (VESPA) has been successfully demonstrated [13][13]. In the lab-scale experiments of VESPA, lead-bismuth eutectic was used as heat transfer fluid and zirconium silicate in the form of spherical ceramic particles as filler material at temperatures from 180°C to 380°C. The tests run for one year with 36 cycles in total and the filler material showed no signs of corrosion under the electron microscope after the experiments.

In parallel to the VESPA experimental campaign a selection of filler materials was tested (in collaboration with Institute for Pulsed Power and Microwave Technology (IHM, KIT)) in contact with 500°C lead-bismuth eutectic for 4 weeks. The selection was based desired thermo-physical properties, which are a high heat capacity, high density and low thermal conductivity, based on numerical simulations [14.]The results showed that the two glasses investigated (sodium glass und borosilicate glass) exposed to LBE are not resistant to LBE as can be seen in Figure 1 a) and b). Under the investigated ceramics, the amorphous phase of steatite is penetrated predominantly by lead, as is shown in Figure 1 c). The scanning electron microscope images of the surfaces of zirconium silicate and zirconium dioxide do not show any signs of corrosion attack as can be seen in Figure 1 d) and e).

In 2023, a pilot-scale set-up (DUO-LIM) with a thermal storage capacity of 100 kWh is planned to be tested, again using zirconium silicate as packed bed due to the successful compatibility in the lab-scale tests.

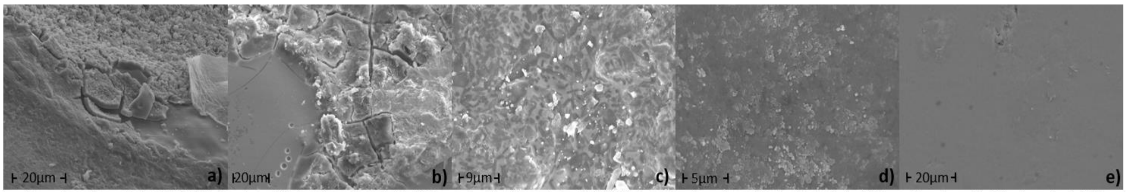

sodium glass, 4 weeks in LBE (1500x)
borosilicate glass, 4 weeks in LBE (1000x)
steatite, 4 weeks in LBE (2500x)
zirconium silicate, 4 weeks in LBE (5000x)
zirconium dioxide, 4 weeks in LBE (1500x)

Figure 1: Different materials exposed to LBE for 4 weeks and LBE is removed. a) sodium glass, b) borosilicate glass c) steatite, d) zirconium silicate, e) zirconium dioxide

Set up of a High Temperature Liquid Metal Loop for Testing Future Process Engineering Key Components

At the Karlsruhe Liquid Metal Laboratory (KALLA), a high temperature liquid lead loop has been designed and is currently in the construction phase. The goal of the BMWK funded project LIMELISA is to test key components for advanced process engineering like valves and a radial pump provided by the project coordinator KSB [15]. In 2022, the piping and instrumentation diagram (P&ID) has been developed and represents the functional relationship between all components like vessels, pipes, valves, pumps and the instrumentation of the different components of the test rig. Safety considerations have been made and loop components like vessels, piping system and venturi flow meters, and supporting structures, manufacturing dummies and a protection tray are available or currently under construction (Figure 7). In addition, hardware like semi-finished products, pipes, pipe fittings, metal profiles, pipe- and component hangers, valves, flange connections, gaskets, lead, heat tracing, instrumentation, measurement- and control technique as well as vacuum components have been selected and purchased. Furthermore, electrical cabinets for the power supply of the trace heating and related fuses and relays have been designed and assembled.

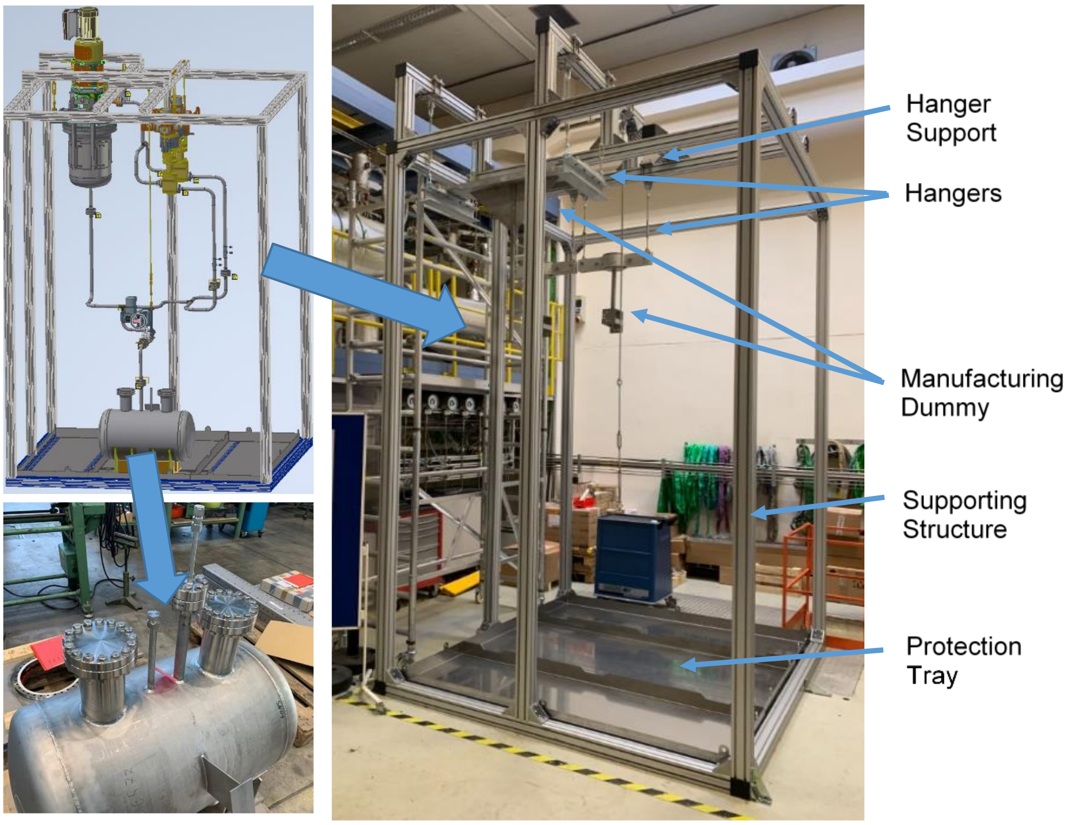

Figure 7: Top left: CAD model of the high-temperature liquid metal loop of LIMELISA, bottom left: sump tank, right: Construction of the supporting structure for the liquid metal loop

Liquid metal based process technology

DECAGAS^{LM} - Decarbonisation of natural gas in liquid metal

Hydrogen technology is seen as a major pillar of a successful energy transition. In June

2020, the German government adopted the national hydrogen strategy [16]. While, the preferred hydrogen production option formulated there is so called green hydrogen, i.e. such produced by water electrolysis, we work at KALLA on another production route, the so called pyrolysis of methane or other hydrocarbons as raw material, but nevertheless without producing CO_2. Since 2012, the work carried out at KALLA has led to a continuously operable process for direct thermal methane pyrolysis as a viable process to produce hydrogen and solid carbon from methane, several gas mixtures such as natural gas H (standard pipeline gas in Germany) and – perspectively – biogas. In the process, the extensive experience with liquid metals, established at KALLA, could be transferred into successful lab-scale experiments, which to date have repeatedly proven the possibility to reach high methane conversion rates and their dependency on operation parameters like temperature [17][18].

Since 2019, together with the industrial partner Wintershall Dea [19] the technique has been further developed towards the use in an industrial scale. The basis is the pyrolysis of methane in a liquid metal bubble column reactor (see Figure 8).

In this process, methane gas or mixtures were passed through liquid tin, heated to a temperature of 950 °C to 1200 °C. Due to the temperature conditions, the methane as well as higher alkanes are split into two components, solid powdered carbon and gaseous hydrogen. Since the solid carbon has a much lower density than the liquid tin, it accumulates on the surface of the liquid metal and was discharged during operation of the reactor. The gas phase, containing a mixture of hydrogen, unreacted methane and other hydrocarbons, will be further processed according to the requirements of the final application. Unreacted methane and other hydrocarbons can be fed back into the reactor.

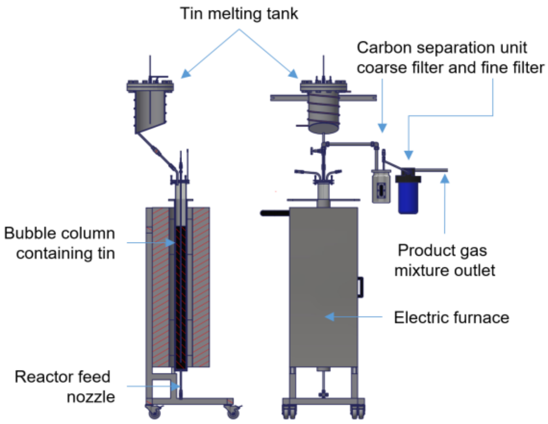

Figure 8: Bubble column reaction system for pyrolysis with carbon separation system.

The extended development of the reactor since 2019 resulted in carbon discharge in operation, increased throughput and the pyrolysis of natural gas H. Additionally the influence of several admixtures to pure methane on the hydrogen yield and product gas composition was determined.

MTET InnoPool Solar H_2

The Innovation Pool project *“Clean and Compressed Solar H_2“* is evaluating the use of solar energy to produce hydrogen by direct thermal pyrolysis of methane based on liquid metal technology.

In a chemical reactor filled with liquid tin, methane decomposes into hydrogen and solid carbon. No CO2 is emitted in this process. A significant degree of CH4 conversion is achieved at a temperature of around 1000 °C. For this process to be completely CO2-free, the energy required for the pyrolysis reaction must be derived from renewable energy sources such as solar thermal energy or photovoltaic.

In 2022 the project carried out an in-depth theoretical analysis of the influence of CO_2 on methane pyrolysis as a key factor in the use of biogas (a renewable energy source consisting mainly of methane and carbon dioxide) as a reactant. In this case, according to available literary sources, hydrogen is mainly produced simultaneously by two reactions: dry reforming of methane and pyrolysis of methane. In addition, other parallel reactions occur simultaneously, including the reverse gas shift of water and the Boudoir reaction.

Name	Reaction
CO_2 reforming of methane	$CH_4 + CO_2 \rightleftarrows 2CO + 2H_2$
CH_4 pyrolysis	$CH_4 \rightleftarrows C + 2H_2$
Reverse Water Gas Shift	$CO_2 + H_2 \rightleftarrows CO + H_2O$
Boudouard	$2CO \rightleftarrows CO_2 + C$
Steam reforming of methane	$CH_4 + H_2O \rightleftarrows CO + 3H_2$
Steam reforming of methane	$CH_4 + 2H_2O \rightleftarrows CO_2 + 4H_2$
CO_2 oxidation of Sn	$Sn + 2CO_2 \rightleftarrows 2CO + SnO_2$
CH_4 reduction of SnO_2	$SnO_2 + 2CH_4 \rightleftarrows Sn + 4H_2 + 2CO$

Depending on the ratio of CH_4 to CO_2 feed and the operating temperature of the process, the composition of the product gas changes. The direct application of biogas in the reforming process has very significant potential as it eliminates the costly step of separating carbon dioxide from the input gas mixture.

An important aspect that has the potential to significantly affect overall system performance is the interaction of CO_2 and liquid tin at operating temperatures. Theoretical analysis has shown that although CO_2 oxidises metallic tin, at the high temperatures typical of system operation the resulting tin oxide is reduced back to Sn in the presence of carbon and methane. In addition, it is also not expected that tin carbides or carbonates will be formed. However, experimental studies are required to confirm this.

An extensive research review article on all this in detail and on many more aspects was written and submitted to a scientific journal for publication.

NAMOSYN - Anhydrous formaldehyde production with sodium vapours as the catalyst

The BMBF-funded project NAMOSYN (Sustainable Mobility with Synthetic Fuels), involving 37 partners including BASF, BMW, BP, DLR and others, aims to develop and test synthetic fuels for diesel and petrol engines. Anhydrous formaldehyde can be used as an intermediate for the synthesis of a promising alternative to diesel (oligomeric oxymethylene dimethyl ethers, OMEs) [20]. For this purpose, the MEDENA (methanol dehydrogenation with sodium (Na) catalyst) mini-plant was designed and built at ITES with the goal of proving that the dehydrogenation of methanol to anhydrous formaldehyde using sodium as a catalyst can be carried out on a mini-plant scale.

In 2022, the sodium catalyst dosing system was successfully tested. This setup was able to provide a uniform distribution of sodium over time and reproducible results. The catalytic tests were carried out at temperatures ranging from 650 °C to 900 °C and with varying amounts of methanol and sodium in the stream. The results obtained were comparable to those achieved on a lab-scale in the literature [21].

In April 2023, the NAMOSYN project will be completed.

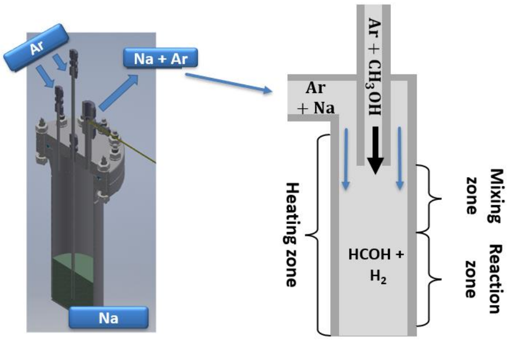

Figure 1. Sodium evaporation unit and reactor concept for dosing of sodium vapour in the MEDENA mini-plant

NECOC - Negative Emissions by Carbon Synthesis from Atmospheric CO_2

The BMWK funded project NECOC aims at creating negative emissions by synthesizing solid carbon materials from atmospheric CO_2 in a three-step process. In collaboration with the two start-ups Climeworks Germany GmbH and INERATEC GmbH, a group of researchers from the Karlsruhe Liquid Metal Laboratory (KALLA) and the Institute of Thermal Process Engineering (TVT) successfully demonstrated the process shown below in December 2022, converting atmospheric CO_2 into carbon powder for several days.

Atmospheric CO_2 is separated from the air via a direct air capture (DAC) facility developed by Climeworks. The second process step, operated by INERATEC, is the catalytic methanation of CO_2 using microstructured reactor concepts in order to overcome the challenge of the high thermal stability of the CO_2 molecule. In a third step the thermal dissociation of methane, also known as methane pyrolysis, takes place in a liquid metal bubble column reactor developed at KALLA. The innovative technology using liquid tin as heat transport medium prevents the pyrolysis reactor from clogging as the solid carbon produced by methane pyrolysis rises to the liquid metal surface as a powder due to its lower density compared to tin.

After extensive preparation and theoretical work [22], at the end of 2022, carbon was synthesized successfully via methane pyrolysis at two temperature levels, using gas mixtures from the methanation of atmospheric CO_2 as feedstock. No disruption of the pyrolysis process due to impurities from previous process steps (H_2, CO_2, N_2, H_2O, O_2) was observed. Currently, the thus obtained carbon products are analyzed in detail in order to determine their potential for various industrial applications. According to the process parameters realized, different types of carbon formed during methane pyrolysis in the liquid metal bubble column reactor were found, see Figure 1.

The successful demonstration of the NECOC process was met with huge interest, from the media, industry, individuals and politicis [23].

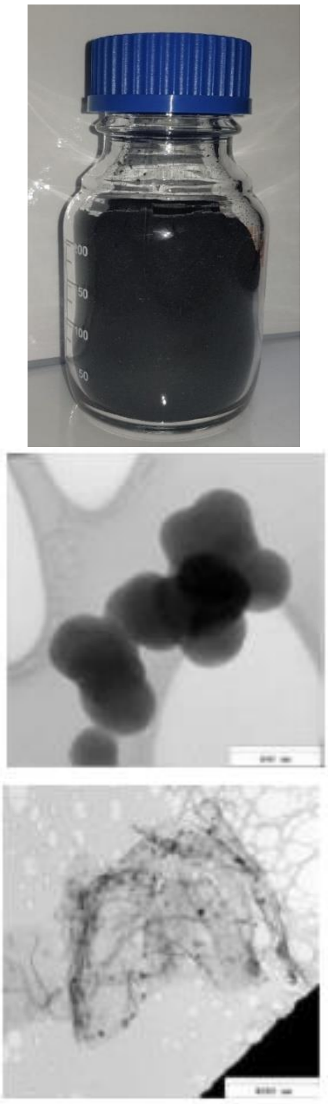

Figure 1: top: Carbon powder synthesized from atmospheric CO2 via the NECOC process; middle: transmission electron microscopy (TEM) picture of soot particles [22]; bottom: TEM picture of graphene-like carbon sheets mixed with soot particles [22].

References

[1] Laube, T., Emmendörfer, F., Dietrich, B., Marocco, L., Wetzel T.; Thermophysical properties of the near eutectic liquid Ga-In-Sn

alloy. Data Article. KITopenData [Online-Datenbank], 2021. doi: 10.5445/IR/1000140052.

[2] Laube, T., Dietrich, B., Marocco, L., Wetzel, T.; Turbulent heat transfer in a liquid metal tube flow with azimuthally inhomogeneous thermal boundary conditions. Int. J. Heat Mass Transf. 189, 122734, 2022.

[3] Laube, T., Dietrich, B., Marocco, L., Wetzel, T.; Heat transfer and pressure drop data of a turbulent tube flow of water and GaInSn with azimuthally inhomogeneous heat flux. Data Article. KITopenData [Online-Datenbank], 2023. https://

[4] Laube, T., Dietrich, B., Marocco, L., Wetzel, T.; Conjugate heat transfer of a turbulent tube flow of water and GaInSn with azimuthally inhomogeneous heat flux. Submitted to Int. J. Heat Mass Transf., Februar 2023, Reviews receiced Mai 2023.

[5] Skupinski, E., Tortel, J., Vautrey, L.; Determination des coefficients de convection d'un alliage sodium-potassium dans un tube circu-laire, Int. J. Heat Mass Transf., vol. 8, no. 6, pp. 937–951, 1965.

[6] Flesch, J.; LBE-cooled tube receiver performance - Design aspects and high-flux operation in a solar furnace, Dissertation, KIT, 2021.

[7] Straub, S., Forooghi, P., Marocco, L., Wetzel, T., Frohnapfel, B.; Azimuthally inhomogeneous thermal boundary conditions in turbulent forced convection pipe flow for low to medium Prandtl numbers, Int J. Heat Fluid Flow, vol. 77, no. 6, pp. 352–358, 2019.

[8] Pacio, J., Daubner, M., Fellmoser, F., Litfin, K., Wetzel, T.; Heat Transfer Experiment in a Partially (Internally) Blocked 19-Rod Bundle with Wire Spacers Cooled by LBE, Nuclear Engineering and Design, 330 (2018), 225-240

[9] Pacio, J., Daubner, M., Wetzel, T.; Local Blockages in a Rod Bundle with Wire Spacers: Heat Transfer in LBE for the Safety Assessment of MYRRHA, Advances in Thermal Hydraulics (ATH 2018) 2018 ANS Winter Meeting, Orlando, Florida, November 11-15, 2018

[10] Batta, A., Class, A. G.; Thermalhydraulic CFD Validation for Liquid Metal Cooled 19-Pin Hexagonal Wire Wrapped Rod Bundle, 8th International Topical Meeting on Nuclear Reactor Thermal Hydraulics (NURETH-18), Portland, Oregon, USA, August 18-23, 2019

[11] Batta, A., Class, A. G., Pacio, J.; Numerical analysis of a LBE-cooled blocked 19-pin Hexagonal wire wrapped rod bundle experiment carried out at KIT-KALLA within EC FP7 Project MAXSIMA, The 8th European Review Meeting on Severe Accident Research (ERMSAR), Warsaw, Poland, May 16-18, 2017

[12] Niedermeier, K.; Numerical Investigation of a Thermal Storage System Using Sodium as Heat Transfer Fluid (PhD thesis), KIT Scientific Publishing, KIT-SR 7755, 2019.

[13] Müller-Trefzer, F., Niedermeier, K., Daubner, M., Wetzel, T.; Experimental investigations on the design of a dual-media thermal energy storage with liquid metal, Applied Thermal Engineering, 213 (2022), 118619.

[14] Laube, T., Marocco, L., Niedermeier, K., Pacio, J., Wetzel, T.; Thermodynamic Analysis of High-Temperature Energy Storage Concepts Based on Liquid Metal Technology, Energy technology, 8 (3) (2020), 1900908.

[15] Niedermeier, K., Lux, M., Weisenburger, A., Wetzel, T.; Design of an Experimental Loop for Testing Key Components for Thermal Energy Storage with Liquid Lead at 700 °C, 2022. International Renewable Energy Storage and Systems Conference (IRES 2022), Düsseldorf, Deutschland, 20.–22. September 2022.

[16] Die nationale Wasserstoffstrategie. BMWi, 2020. https://www.bmwi.de/Redaktion/DE/Publikationen/Energie/die-nationale-wasserstoffstrategie.pdf

[17] Geißler, T.; Methan-Pyrolyse in einem Flüssigmetall-Blasensäulenreaktor. Dissertation. Karlsruher Institut für Technologie. 2017.

[18] Stoppel, L., Fehling, T., Geißler, T., Baake, E., Wetzel, T., Carbon dioxide free production of hydrogen, IOP Conference Series: Materials Science and Engineering, 228 (2017), 012016

[19] Presseinformation 141/2019. Wasserstoff aus Erdgas ohne CO_2-Emissionen. https://www.kit.edu/kit/pi_2019_wasserstoff-aus-erdgas-ohne-co2-emissionen.php

[20] Oestreich, D., Lautenschütz, L., Arnold, U., Sauer, J.; Reaction kinetics and equilibrium parameters for the production of oxymethylene dimethyl ethers (OME) from methanol and formaldehyde, Chemical Engineering Science, 163 (2017), 92-104

[21] Ruf, S., May, A., and Emig, G.; Appl. Catal. A Gen., vol. 213, no. 2, pp. 203–215, 2001

[22] Uhlenbruck, N., Dietrich, B., Hofberger, C., Stoppel, L., Wetzel, T. (2022); Methane Pyrolysis in a Liquid Metal Bubble Column Reactor: A Model Approach Combining Bubble Dynamics with Byproduct and Soot Formation. Energy Technol., doi.org/10.1002/ente.202200654

[23] https://www.kit.edu/kit/pi_2022_107_neue-anlage-produziert-kohlenstoff-aus-luft.php

Department: Resilient and Smart Infrastructure Systems (RESIS)

Key Advancements in the Research Area of Energy System Resilience, Nuclear Safety, and Decision Support in 2022

S. S. Ottenburger, D. Trybushnyi, N. Chavan, T. Makumbi, T. Schichtel, T. Müller, W. Raskob

Introduction

RESIS conducts research in the area of smart resilience engineering and risk mitigation technology. Is active in two Helmholtz programs, namely Energy System Design (ESD) and Nuclear Waste Management, Safety and Radiation Research (NUSAFE), and contributing to the EuroFusion program. In general, RESIS combines the use of simulations, artificial intelligence and mathematics to develop solutions that improve the resilience of critical socio-technical systems [1]. The challenges of the energy transition as well as the management of potential nuclear hazards are part of the RESIS topic portfolio. We are working on a better understanding of risks, which on the one hand can be dispersion-based and e.g. radiological in nature or relate to complex networked infrastructure systems, which are more systemic in nature. An in-depth analysis of (systemic) risks and uncertainties provides a basis for developing different approaches to resilience-enhancing measures. This report outlines some of our key activities in 2022.

Planning and Managing Complex Networked Systems

FRAMESS (Framework for Systemic Risk Analysis and Exploration of Sustainable Solutions) is a platform approach for advanced simulation, resilience studies and decision support and it employs various techniques, including graph- and multi-agent-based simulation, to facilitate comprehensive risk analysis and validation of resilience concepts. It offers robust sustainable modeling and a software engineering architecture that is adaptable to various contexts, such as energy, transport, and urban environments. Moreover, it seamlessly integrates multi-criteria decision analysis (MCDA), making it a powerful tool for informed decision-making. This platform also caters to the demands of AI-driven network optimization and management. An initial version of FRAMESS was officially introduced at the 2022 Hannover Fair, and it has been extensively applied in the SimPaTrans project as the foundational technology for a Decision Support System, serving the German Federal Agency for Civil Protection and Disaster Relief (BBK). This collaboration has yielded significant advancements in the field. FRAMESS is not just a stand-alone tool; it forms a potential basis for a wide array of resilience planning and crisis management projects, to bolster preparedness and response capabilities.

High dams and hydropower: Neural networks and risk forecast

In the project DAMAST, studying the safety of the large Enguri dam and its hydropower plant in Georgia, our main research topic was directed onto the search for approaches to compute dam displacement as well as the induced seismicity. No physical models to represent these quantities as a function of observable meteorological and hydrological variables were known, so an alternative way of creating a good approximation was suggested: a usage of artificial intelligence algorithms. The last decade has brought a deep understanding and robust implementations of the AI tools and frameworks, particularly the Deep Neural Networks (DNNs). Nowadays, a Python developer with some data science background can prepare the data to study, clean it up, define the model input and output and start an automated search for the best DNN to fit the data (see Autokeras [2]). In the project the following relations were studied: 'induced seismicity - water level, net solar radiation, air temperature, atmospheric surface Pressure', 'dam displacement - water level, net solar radiation, air temperature, atmospheric surface pressure, with/without seismicity'. The automated approach has brought up an observation that the net solar radiation helps a DNN to essentially reduce the error on the validation data subset. In other words, the net solar radiation is in high correlation with the induced seismicity and the dam displacement. A physically based open source model WRF-Hydro[3] was preliminarily tuned up to calculate the relation 'precipitation - water level'. For the other two variables - induced seismicity and dam displacement - a corresponding DNN with a good approximation was found. As it is possible to freely get good quality meteo forecasts for the whole world (Global Forecast System model [4], NOMADS meteo provider [5]), the WRF-hydro model together with the two DNNs can calculate a forecast of the induced seismicity and the dam displacement. Further work on converting these parameters into the risk forecast is planned.

Fusion reactor accidents and tritium

Our task in the EuroFusion program to perform dose assessments to the population from hypothetical accidents of the next step fusion reactor named DEMO. As fusion reactors differ from nuclear power plants, in particular as the radionuclide tritium is an important component of the inventory, special assessment models have to be applied. Furthermore, as the site of DEMO is not known at present, probabilistic studies for a generic site have to be performed. To be in line with former studies for ITER (International Thermonuclear Experimental Reactor), similar boundary conditions were used. The two probabilistic assessment codes COSYMA [6] for activation products and UFOTRI [7] for tritium were applied. In 2022, the focus of the work was related to screening for unit releases of tritium, activated corrosion products (ACPs) and tungsten dust. Deterministic calculations with different meteorological parameters, representing typical worst-case release conditions were compared with the 95% percentile of the probabilistic release scenarios. The highest doses in the vicinity of the site were similar for the worst-case deterministic scenario and the 95% percentile. This assured, that the 95% percentile that is used in our assessments did not underestimate the consequences to the population.

As the two assessment models COSYMA and UFOTRI were developed some 30-40 years ago, in particular the atmospheric dispersion models of the two codes are no longer state of the art. To overcome that issue, a new task was setup in 2021 to integrate the tritium specific functionalities of UFOTRI into the decision support system JRODOS (JAVA based real-time online decison support) with state-of-the-art simulation models [8]. Besides this integration of tritium specific features, probabilistic functionalities will be also added. This would allow to perform similar assessments with just one code JRODOS as was so far done with two, COSYMA and UFOTRI. Work in 2022 concentrated on the extraction of routines from UFOTRI.

JRODOS: Activities for the Ukraine

The year 2022 brought new challenges to the world, and this had a reflection on the RESIS group activities [9]. Due to the war in Ukraine the risks of a nuclear accident on one or sev-

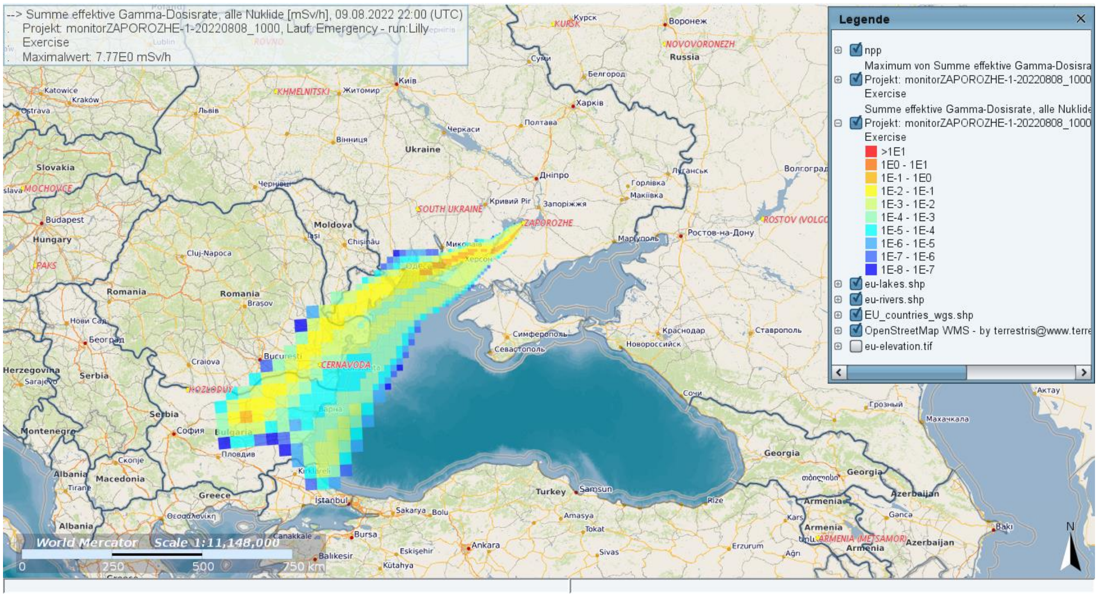

Figure 1 A potential heavy release scenario at Zaporischschja NPP, total gamma dose rate, 24h after the release.

eral Ukrainian nuclear power stations have increased dramatically. To build up the preparedness and be ready to estimate the potential consequences of such cases a close contact to the State Nuclear Regulatory Inspectorate of Ukraine, Ukrainian Hydromet and other Ukrainian authorities has been established in March 2022. Several detailed heavy accident scenarios have been given to the group by the Inspectorate. Since April 2022 there are JRODOS atmospheric dispersion calculations for all the four Ukrainian nuclear power stations performed hourly in an automatic manner. The resulted concentration and dose rate maps are then exchanged with the Japanese partners to compare the calculations with the Japanese atmospheric dispersion model SPEEDY. In all the different weather situations observed within the 8 months the comparison between JRODOS and SPEEDY was consistent. This fact brings an additional assurance that the data processing and the computational models used in JRODOS correctly represent the reality.

Towards the new JRODOS Module for Nuclear Explosions

The JRODOS module 'Nuclear Explosion' is developed to serve for the quantitative risk assessment based on fallout predictions for land surface bursts of nuclear weapons. The Lagrangian atmospheric dispersion models LASAT and FLEXPART are utilized in the module 'Nuclear Explosion”. The range of validity of LASAT concerning the horizontal extent is local to regional range (up to source distances of about 200 km), that of FLEXPART up to global range. The application of LASAT has to be validated carefully because of the limited vertical extent.

The fallout pattern from particles of visible size is established within about 24 hours after the burst. This is referred to as 'early' fallout, also sometimes called 'local' or 'close-in' fallout. In addition, there is the deposition of very small particles which descend very slowly over large areas of the earth's surface. This is the 'delayed' (or 'worldwide') fallout, to which residues from nuclear explosions of various types – air, high-altitude, surface, and shallow subsurface – may contribute.

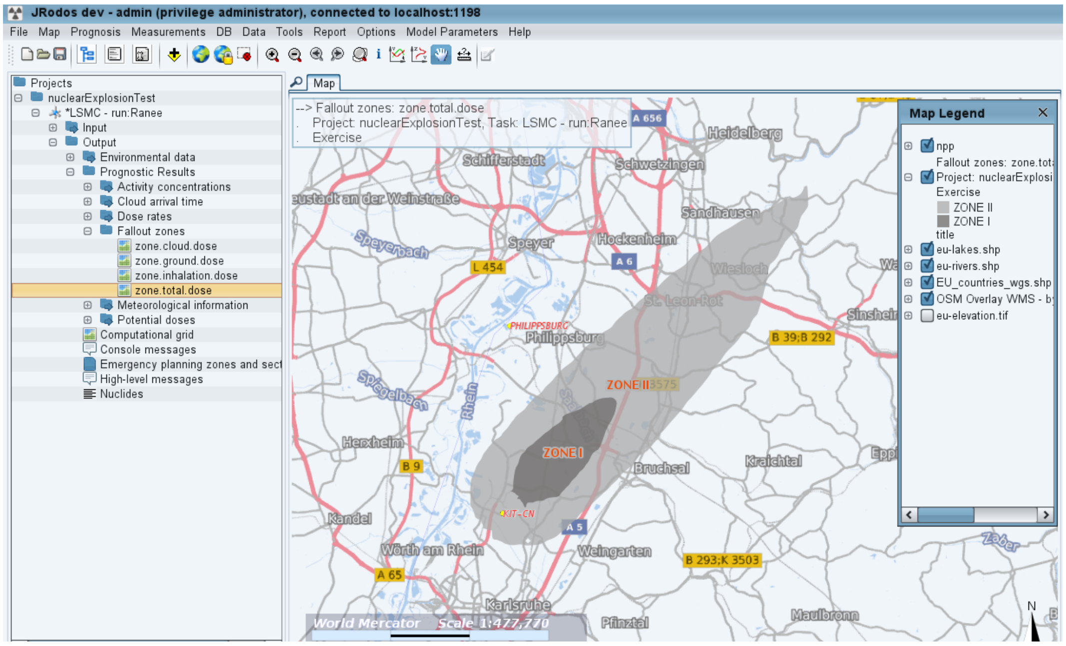

JRodos dev - admin (privilege administrator), connected to localhost:1198

--> Fallout zones: zone.total.dose
Project: nuclearExplosionTest, Task: LSMC - run:Ranee
Exercise

Figure 2 Hazard areas: Zone I and Zone II

JRODOS presents the hazard zone I (potential effective dose after 4 hours exceeds 1500mSv) and hazard zone II (potential effective dose after 24 hours exceeds 500mSv) for cloud-shine, ground-shine, inhalation and total dose. (s. Fig. 2)

Furthermore, JRODOS presents the cloud arrival times as contour plot for each time-step without (Fig. 3) and together with additional results (Fig. 4)

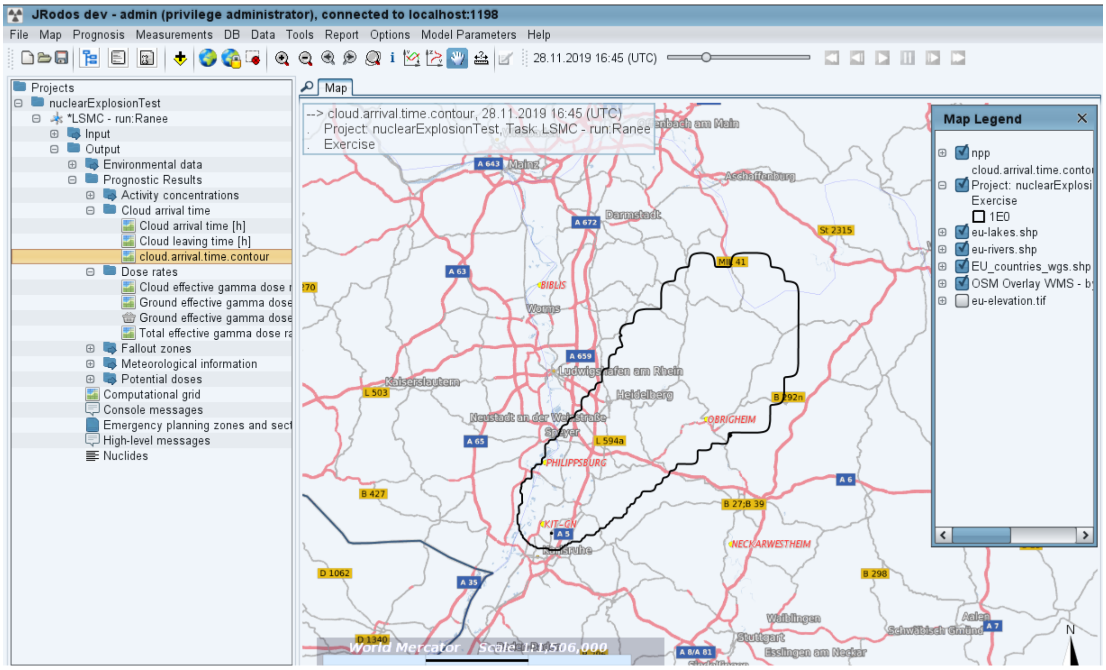

JRodos dev - admin (privilege administrator), connected to localhost:1198

28.11.2019 16:45 (UTC)

--> cloud.arrival.time.contour, 28.11.2019 16:45 (UTC)
Project: nuclearExplosionTest, Task: LSMC - run:Ranee
Exercise

Figure 3 Cloud arrival time contour plot

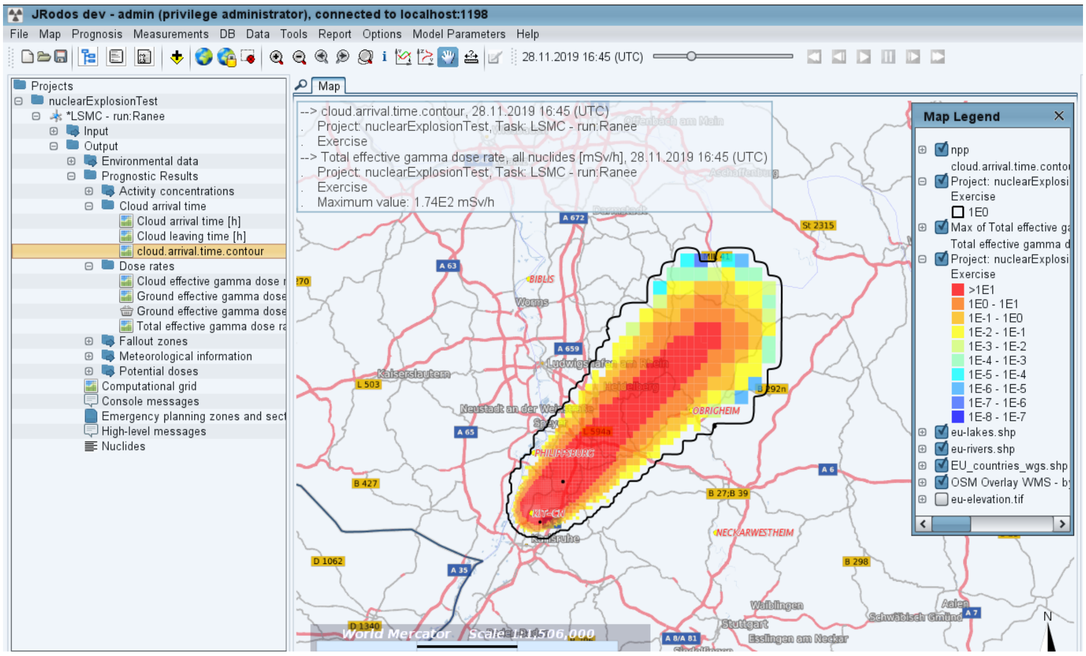

```
--> cloud.arrival.time.contour, 28.11.2019 16:45 (UTC)
.   Project: nuclearExplosionTest, Task: LSMC - run:Ranee
.   Exercise
--> Total effective gamma dose rate, all nuclides [mSv/h], 28.11.2019 16:45 (UTC)
.   Project: nuclearExplosionTest, Task: LSMC - run:Ranee
.   Exercise
.   Maximum value: 1.74E2 mSv/h
```

Figure 4 Cloud arrival time contour plot together with total effective gamma dose rate

Figures 2-4 show the results of a simulation run for a nuclear explosion of 60kt explosive yield. JRODOS was equipped to handle aerosols. The particle size distribution is a characteristic of the nuclear explosion and therefore part of the module setup. In 2022 the focus of the work was the improved modelling of the inhalation dose. Particles with a diameter of more than 10µm will not contribute to the inhalation dose. Although the model rule for this realization is simple the code realization in JRODOS is very expensive.

Multi-criteria decision analysis and different application contexts

Two main aspects have driven the activities of the RESIS department in the field of MCDA during 2022: The project MAESTRI and the coordinated Helmholtz efforts regarding MCDA.

MAESTRI (Management Systems Supporting Environmental Remediation) is a project of the IAEA (International Atomic Energy Agency) and addresses the environmental remediation of radiologically contaminated sites like e.g. the vicinity of former nuclear power plants. The challenge in this task is to find a justifiable balance between the restoration of the original state in between ‘as much as possible” and ‘as much as needed”, taking various stakeholder interests into account in the decision making.

RESIS is part of the MAESTRI core group acting as MCDA expert and advisor in the ongoing project. The task of the core group is to establish MCDA as the method of choice addressing the before mentioned objective, providing best practice guidelines and a gold standard for an effective approach, coaching the selection of appropriate methods and last but not least to train the according people of the IAEA member states to operatively apply MCDA in the end.

So far, these activities have resulted in an official document summarizing the method, justification by selected historic examples and suggestions how to approach the objective. Also, during 2022 RESIS has actively contributed in organising two workshops in February and October for dissemination and spreading of the MAESTRI project. In addition to the supervised exercises during this workshop the MCDA tool of ITES was presented as a teaching and training utility for the MCDA method in general and in particular for the environmental remediation.

The coordinated Helmholtz efforts regarding MCDA aim for spreading and awareness of the usefulness of the MCDA methodology in the area of energy system design [10] and sustainability. Started in 2021 by KIT (ITES, ITAS), DLR, and FZ Jülich the members of the group regularly meet either virtual or in person to coordinate their activities in this area. In 2022 a workshop was organised in Fulda with external experts also joining the meeting, resulting in published report with an overview of MCDA activities in Helmholtz so far and suggestions for best practises. Again, the MCDA tool of ITES was presented on several occasions is now considered as core component for a common Helmholtz MCDA tool to be supported used by the participating institutions. Especially the cooperation between ITAS and ITES lead to several publications and a significant improvement of the MCDA tool in respect to the desired purpose in HGF, enhancing it by several important algorithms (e.g. PROMETHEE) used in the MCDA community.

Assessment of Uncertainties Affecting Dosimetric Calculation for Intake of Radon and NORM

Inhalation of radon gas and progeny is one of the leading causes of lung cancer among underground miners and indoor workers [11]. The inhaled radon progeny deposit in the respiratory airways of the lung and because of their relatively short half-lives, decay mainly in the lung before being cleared either by absorption to blood or by particle transport to the alimentary tract [12].

The Human Respiratory Tract Model (HRTM) was used to calculate the absorbed doses to regions of the lung. Uncertainty of calculated doses to regions of the lungs needed to be assessed by performing a parameter uncertainty analysis to derive a frequency distribution of the equivalent doses per unit exposure for a miner.

INTDOSKIT in-house software developed at KIT that calculates internal doses was extended to perform a Monte Carlo simulation. Probability distributions for parameter values were chosen to represent variations in exposure conditions and variability among miners.

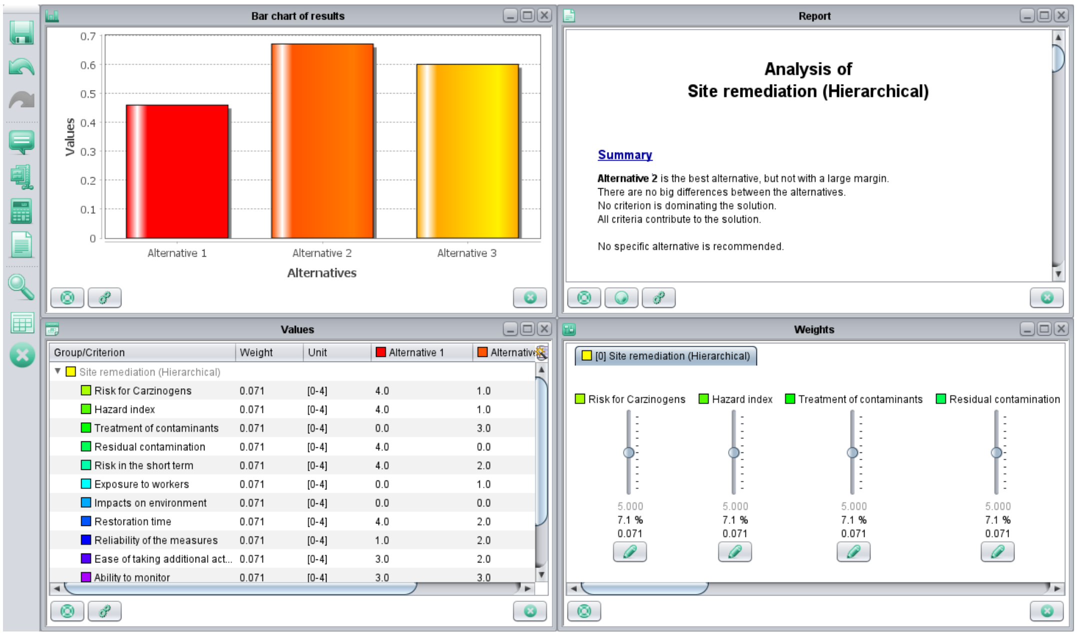

Analysis of
Site remediation (Hierarchical)

Summary

Alternative 2 is the best alternative, but not with a large margin.
There are no big differences between the alternatives.
No criterion is dominating the solution.
All criteria contribute to the solution.

No specific alternative is recommended.

Group/Criterion	Weight	Unit	🟥 Alternative 1	🟧 Alternativ
▼ 🟨 Site remediation (Hierarchical)				
🟩 Risk for Carzinogens	0.071	[0-4]	4.0	1.0
🟩 Hazard index	0.071	[0-4]	4.0	1.0
🟩 Treatment of contaminants	0.071	[0-4]	0.0	3.0
🟩 Residual contamination	0.071	[0-4]	4.0	0.0
🟩 Risk in the short term	0.071	[0-4]	4.0	2.0
🟦 Exposure to workers	0.071	[0-4]	0.0	1.0
🟦 Impacts on environment	0.071	[0-4]	0.0	0.0
🟦 Restoration time	0.071	[0-4]	4.0	2.0
🟦 Reliability of the measures	0.071	[0-4]	1.0	2.0
🟪 Ease of taking additional act...	0.071	[0-4]	3.0	2.0
🟪 Ability to monitor	0.071	[0-4]	3.0	3.0

🟨 [0] Site remediation (Hierarchical)

🟩 Risk for Carzinogens	🟩 Hazard index	🟩 Treatment of contaminants	🟩 Residual contamination
5.000	5.000	5.000	5.000
7.1 %	7.1 %	7.1 %	7.1 %
0.071	0.071	0.071	0.071

Figure 5. The MCDA tool as it was used in the MAESTRI workshop. Evaluation of criteria and stakeholder preferences leads to an ranking of alternatives as a suggestion for decision makers.

A total of 1000 runs were performed and a dose distribution obtained. Figure 6 depicts the Monte Carlo simulation technique.

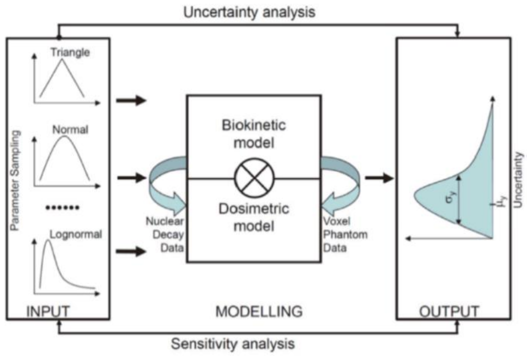

Figure 6: Monte Carlo simulation for uncertainty and sensitivity analysis [3]

Simulation results showed that the equivalent dose to the lung followed a normal distribution with a mean value of 24.57 mSv/mJhm-3 and a standard deviation of 0.33 as shown in Figure 7.

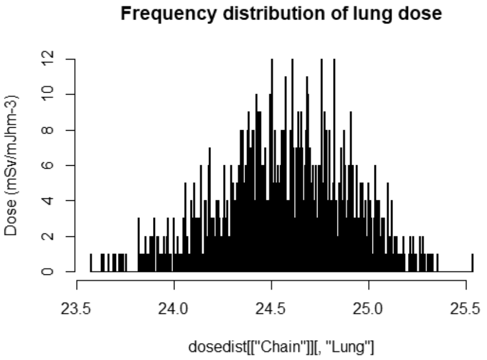

Figure 7: Distribution of lung dose

Modeling the biokinetic behavior of americium in the human body with and without the presence of decorating agents

This work is part of the German Ministry for Education and Research (BMBF) funded project RADEKOR. it aims to improve the understanding and model the behavior of radioactive materials in the human body.

The assessment of radiation dose is important after the internal exposure of Americium to estimate risks, minimize exposure, and adhere to regulations. To estimate the intake, both in vivo and in vitro measurements are employed, complemented by biokinetic modelling. The widely accepted biokinetic models provided by the International Commission for Radiation Protection (ICRP) are commonly utilized. localized contamination is reduced by administrating chelating agents such as Ca-DTPA or Zn-DTPA to the patients. It accelerates the urinary and faecal excretion of Americium. Chelating agents form complexes with Americium and reduce its effect on metabolic processes and remove them from body. However, the precise chelation sites within the human body remain unknown. As part of our ongoing project, we aspire to identify this chelation mechanism in the liver and model the kinetics of the chelation process within the human body.

Due to the scarcity of data and knowledge available we are actively interacting with people on various platforms such as European Radiation Dosimetry Group (EURADOS), Health Physics Society (HPS). This year we have visited Los Alamos National Laboratory (LANL) and United States Transuranium Registries (USTUR) for possible collaborations. In 2 trips to USTUR, the human case data of interest is identified. This data is being used to understand the biokinetics of Am in the presence of chelating agent and Development of pharmacokinetically realistic model for Americium.

References

[1] Fuchs, S., „Den Total-Blackout in jedem Fall verhindern‘ – Resilienzforschung am KIT - Campus-Report am 18.10.2022“, 2022, doi: 10.5445/IR/1000151566.

[2] „AutoKeras: An AutoML system based on Keras“. Zugegriffen: 15. Oktober 2023. [Online]. Verfügbar unter: https://autokeras.com/

[3] „WRF-Hydro Modeling System“. Zugegriffen: 15. Oktober 2023. [Online]. Verfügbar unter: https://ral.ucar.edu/projects/wrf_hydro

[4] „Global Forecast System (GFS)“. Zugegriffen: 15. Oktober 2023. [Online]. Verfügbar unter: https://www.ncei.noaa.gov/products/weather-climate-models/global-forecast

[5] „NOAA Operational Model Archive and Distribution System“. Zugegriffen: 15. Oktober 2023. [Online]. Verfügbar unter: https://nomads.ncep.noaa.gov/

[6] Commission of the European Communities, „COSYMA (1991) COSYMA: A New Program Package for Accident Consequence Assessment. A Joint Report of KfK and NRPB“, Nr. Report EUR-13028 EN, 1991.

[7] Raskob, W., „UFOTRI: Description of the New Version of the Tritium Model UFOTRI 4.0, including user guide“, Bd. Report KfK-5194, 1993.

[8] Levdin, I., Trybushnyi, D., Zheleznyak, M. und Raskob, W., „RODOS re-engineering: aims and implementation details“, Bd. Raskob W, Hugon M (eds) Enhancing nuclear and radiological emergency management and rehabilitation: Key results of the EURANOS European project, S. 181–189.

[9] Zheleznyak M., u. a., „Ecological footprint of Russia’s Ukraine invasion“, Science, Bd. 377, Nr. 6612, S. 1273–1273, Sep. 2022, doi: 10.1126/science.ade6869.

[10] Ottenburger, S. S., Möhrle, S., Müller, T. O. und Raskob, W., „A Novel MCDA-Based Methodology Dealing with Dynamics and Ambiguities Resulting from Citizen Participation in the Context of the Energy Transition“, Bd. Algorithms, Nr. 15(2), 2022, doi: 10.3390/a15020047.

[11] Kendall, G. M. und Smith, T. J., „Doses to Organs and Tissues from Radon and its Decay Products“, Bd. Journal of Radiological Protection, Nr. 22, 2002.

[12] Marsh, J. W., Uncertainty analysis of the absorbed dose to regions of the lung per unit exposure to Radon progeny in a mine. Didcot: Health Protection Agency, 2009.

Department: Energy and Process Engineering

Design study of the MONIKA-ORC-Turbine and comparison with experimental results

Cristian Leonardo Niño Avella, Hans-Joachim Wiemer

For industrial waste heat applications, the heat of 100 - 200 °C has a great potential. One way to tap this energy potential is its conversion into electrical energy via a thermodynamic cycle process. Electricity generation for these low temperature cycles is today usually realized via an Organic Rankine Cycle (ORC) process.

Varying the boundary conditions and the working fluids used has a large impact on the net power yield and thus the economics of a waste heat application.

The approach taken by the ITES-EVT group is to maximize electrical power production by selecting a heat transfer fluid suitable for the site-specific boundary conditions in Europe and a supercritical live steam pressure. In previous studies ORC [1], [2],[3] Vetter et al. have shown that significant performance improvements are possible under supercritical conditions.

Environmental and operational criteria such as high thermal conductivity, low specific volume, high chemical stability, low corrosiveness, low flammability, toxicity, low ozone depletion potential (ODP) and global warming potential (GWP) were considered in the selection of the working fluid [4].

To optimize and validate this simulation model, we built a supercritical ORC (MoNiKa) (Fig 1,2). This also offers the possibility to analyze individual components in detail.

The following report focuses on the investigation of the ORC turbine.

The MoNiKa power plant

The MoNiKa (Modular low-temperature cycle Karlsruhe) is a small power plant with the following components:

- Turbine
- Propane Tank
- Pumps
- Heat exchanger
- Condenser

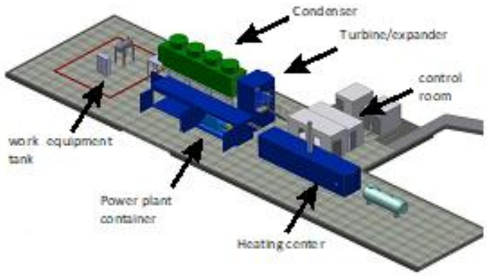

Fig. 1: MoNiKa -ORC power plant

In the master thesis of C. L. Niño Avella [5] we mainly study the experimental results of the turbine operation with a focus on the load range between 40 and 100%.

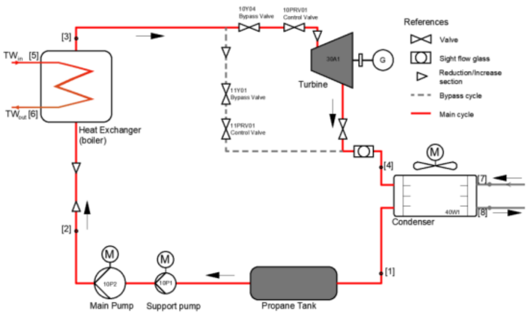

Fig.2: Scheme of the power plant MoNiKa

Component’s description

The pumping system consists of two pumps. A Grundfos circulation pump and a LEWA triplex M514US G3G main pump. This is a membrane piston pump with a maximum mass flow of 3.6 kg/s and a design pressure of 6.5 MPa.

The heat exchanger manufactured by Gesmex, is the connection between both cycles, (water and organic). It is a counter- flow plate heat exchanger designed to work in a supercritical regime. The installed thermal design power is 1000 kW for full load operation.

Fig. 3: Propane tank und Condenser

The condenser Fig.3 manufactured by KÜHL-TURMKARLSRUHE is located between the outlet of the turbine (or throttle valve) and the propane tank. In addition, the condenser is prepared for operation with water spray. The condenser is equipped with three vertical fans (impeller and diffusor) of 2.5m diameter. The power consumption of each motor is max. 13 kW at 322 RPM and a maximum flow rate of 44 m3/s each and a total of 39 kW - 132 m3/s.

The last component of the circuit is the turbine GT 120 – 4 Fig.4.

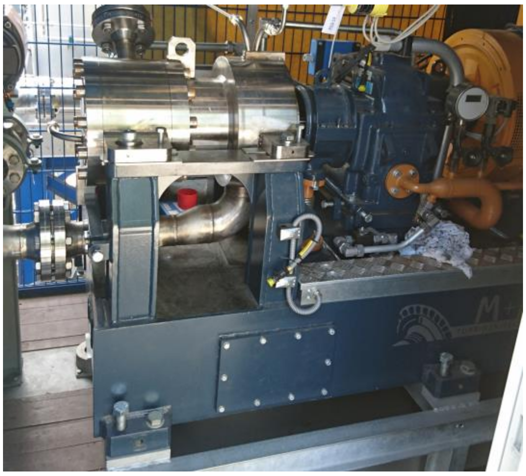

Fig. 4: Turbine with gearbox and generator

Fig.5 shows a cross-section of the axial four-stage propane turbine with constant stage pressure (impulse design) with a nominal rotational speed of 9996 1/min. It is a welded construction made by M+M TURBINE-TECHNIK [8]

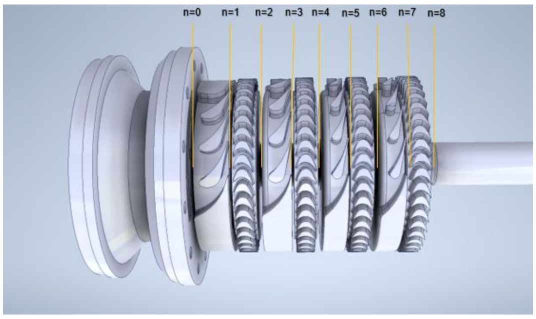

Fig. 5: M+M Turbine interior view

The thrust bearing is located in the steam inlet. It is sealed to the outside by carbon seals. The steam inlet area (face side) is closed and has a leakage gas discharge which is directed to the exhaust steam. In the area of the shaft passage at the coupling connection (gear side), a closed design is not possible. Here, nitrogen is supplied behind the first seal and the nitrogen-propane mixture is vented behind the second seal. Behind the third seal, atmospheric conditions prevail.

A gearbox is connected to the 150 MVA synchronous generator.

The MarelliMotori generator use a DEIF control system. We are measuring the generator power with this system.

Instrumentation

The sensor technology installed in MoNiKa fulfills two requirements: first, to control and operate the power plant, and second, as a platform for scientific studies conducted in the plant. For this reason, the plant is much more extensively instrumented than a normal power plant. For balancing purposes, temperature and pressure sensors are installed along the entire cycle, i.e., at the inlet and outlet of each component.

The mass flow and density of the working fluid is measured between the outlet of the main pump and the inlet of the heat exchanger using an E+H Promass 83F sensor.

A WIKA TR34 Class A-PT100 is used to measure temperatures at all points in the system.

For pressure measurements at the MoNiKa plant we use the Vegabar 81 and 82. These pressure transmitters are universally applicable for the measurement of gases, vapors and liquids.

To measure the environmental conditions, the system is equipped with one pressure, humidity and temperature sensor. In addition, a set of type k thermocouples and a pressure senor is installed in each chamber of the condenser.

Calculation of the turbine

In order to develop the analysis of the MONIKA ORC-Turbine, the study was made on each cross section of it. The variable n represents the cross section in which the calculation is being made as presented in Figure 5.

If the total pressure ratio PR is given as in Equation 1, each stage will have the same pressure ratio as an initial assumption.

$m = 1, \dots 4$

$$PR = \frac{P_0}{P_8} \qquad [kPa] \qquad (1)$$

$$P_{2m-1} = \frac{P_{2m-2}}{PR^{1/4}} \qquad [kPa] \qquad (2)$$

For the case of an ideal impulse turbine:

$$P_{2m} = P_{2m-1} \qquad [kPa] \qquad (3)$$

As the MONIKA turbine is an impulse turbine, in the initial distribution, I supposed that the pressure at the outlet of the vanes is the same as the pressure at the outlet of the blades for the same stage.

Calculation of blade velocity

The MONIKA turbine is an axial impulse turbine, i.e., the fluid moves in the axial direction and the blades move only in the circumferential direction, i.e., their velocity depends only on the angular velocity and the mean radius of the blade as given in equation 5. As mentioned before, the mean radius of the blades and vanes remains constant, and therefore the circumferential velocity of the blades remains constant through the entire turbine.

$$U_{ax,n} = 0 \qquad [\text{m/s}] \qquad (4)$$

$$U_{u,n} = R_{m,n}\omega \qquad [\text{m/s}] \qquad (5)$$

As can be seen in Figure 5, the outlet of the vanes is represented by the odd numbers of n, the outlet of the blades is represented by the even numbers, and the inlet section is indicated by 0. This nomenclature is used in the mean line analysis to go through the different cross sections of the turbine.

Calculation for the vane stage

The calculation for the vane part of the stages, the values for n are 1,3,5,7. This means that the procedure presented below is repeated for each outlet of the vanes.

The first step is to find the isentropic enthalpy using the entropy for the previous stage and the given pressure for this stage. In the case where n=1, the entropy used corresponds to the inlet entropy s_0 of the turbine.

$$h_{s,n} = h(P_n, s_{n-1}) \qquad \text{[J/kg]} \qquad (6)$$

Once the isentropic enthalpy was determined, I used Soderberg's correlation to determine the losses and gain and overall efficiency for each vane stage [9, p.97].

$$\zeta_n{}' = 0.04 + 0.06 * \left(\frac{\varepsilon_n}{100}\right)^2 \qquad - \qquad (7)$$

$$\varepsilon_n = \alpha_n - \alpha_{n-1} \qquad \text{[rad]} \qquad (8)$$

$$\zeta_n = (1 + \zeta_n{}') * \left(0.993 + 0.021 * \frac{ca_n}{hb_n}\right) - 1 \qquad (9)$$

The efficiency of the vane stage can be expressed as a function of the losses, therefore (10 p. 164):

$$\eta_n = 1 - \zeta_n \qquad (10)$$

Once the stage efficiency is defined, the value for the real enthalpy after the vane stage can be found with equation 11.

$$h_n = h_{n-1} - \eta_n(h_{n-1} - h_{s,n}) \qquad \text{[kPa]} \qquad (11)$$

Now that we have the enthalpy and the pressure in the cross-section n, we can find the properties of the fluid, thus

$$s_n = s(h_n, P_n) \qquad \text{[J/kgK]}$$

$$\rho_n = \rho(h_n, P_n) \qquad \text{[kg/m3]}$$

$$T_n = T(h_n, P_n) \qquad \text{[K]}$$

$$X_n = X(h_n, P_n)$$

From the energy balance, it is possible to write the change in enthalpy as a function of the change in kinetic energy, as shown in equation 12.

$$\frac{V_n{}^2}{2} - \frac{V_{n-1}{}^2}{2} = h_{n-1} - h_n \qquad \text{[J/kg]} \qquad (12)$$

The mass flow is directly related to the velocity and density of the fluid as shown in equation 5.13:

$$\frac{V_n{}^2}{2} = \frac{Mv_n}{\rho_n An_n sin\alpha_n} and \frac{V_{n-1}{}^2}{2} = \frac{Mv_n}{\rho_{n-1} An_{n-1} sin\alpha_{n-1}} \qquad \text{[J/kg]} \qquad (13)$$

Since the mass flow is constant at the inlet and outlet of the vane, it can be written using the enthalpy vs. velocity relation for the vane stage as in Equation 14.

$$Mv_n = (2 * (h_{n-1} - h_n) * (\frac{1}{(\rho_n An_n sin\alpha_n)^2} - \frac{1}{(\rho_{n-1} An_{n-1} sin\alpha_{n-1})^2}))^{(\frac{1}{2})} \qquad \text{[kg/s]} \qquad (14)$$

Once the mass flow through the vanes has been determined, the velocity can be calculated.

$$V_{ax,n} = \frac{Mv_n}{\rho_n An_n} \, and \, V_{u,n} = \frac{V_{ax,n}}{tan\ \alpha_n} \qquad [m/s] \qquad (15)$$

$$|V_n| = \sqrt{{V_{ax,n}}^2 + {V_{u,n}}^2} \qquad [m/s] \qquad (16)$$

As mentioned above, the mass flow Mv corresponds only to the amount of fluid flowing through the vanes; to find a more accurate estimation, the leakage mass flow through the labyrinth tips is considered as Ml, it depends on the geometry configuration of the rotor, the density of the fluid and the pressure difference before and after the labyrinth tips [11].

$$Ml1_n = 0.8 * \pi * DL * HL * \sqrt{\rho_{n-1} P_{n-1}} \qquad [kg/s] \qquad (17)$$

$$Ml_n = ML1_n * \sqrt{\frac{1 - \left(\frac{P_n}{P_{n-1}}\right)^2}{z1 + \ln\left(\frac{P_{n-1}}{P_n}\right)}} \qquad [kg/s] \qquad (18)$$

Therefore, the total mass flow for the vane stage is estimated as follows

$$M_n = Mv_n + Ml_n \qquad [kg/s] \qquad (19)$$

Calculation for the blade stage

Once the mass flow is determined for the vane, it is possible to continue the calculation for the blades, which means the value of n=2,4,6,8.

The density remains constant as a first approximation for the inlet of the blades:

$$\rho_n = \rho_{n-1} \qquad [kg/m3] \qquad (20)$$

This value for the density is calculated again in function of enthalpy and pression and then it will be given as inlet value and calculated over and over again until it converges. In order to make this, it is necessary to find the enthalpy and pressure after the blade stage.

The relative velocity at the inlet of the turbine can be calculated as:

$$\vec{W}_{n-1} = \vec{V}_{n-1} - \vec{U}_{n-1} \qquad [m/s] \qquad (21)$$

The mass flow is considered constant as a second consideration.

$$M_n = M_{n-1} \qquad [kg/s] \qquad (22)$$

In order to determine the losses in the blade, the Soderberg's correlation has been used again, the expression in the case of the blades is slightly different to the one used for the vanes [9], being:

$$\beta_{n-1} = \mathrm{atan}\left(\frac{W_{ax,n-1}}{W_{u,n-1}}\right) \, and \, \beta_n(measured) \qquad [rad] \quad (23)$$

$$\zeta_n{}' = 0.04 + 0.06 * \left(\frac{\varepsilon_n}{100}\right)^2 \qquad - \qquad (24)$$

$$\varepsilon_n = \beta_n - \beta_{n-1} \qquad [rad] \quad (25)$$

$$\zeta_n = (1 + \zeta_n{}') * \left(0.975 + 0.075 * \frac{ca_n}{hb_n}\right) - 1 \qquad - \qquad (26)$$

Now with the Soderberg loss coefficient, the efficiency for the blade was determined as in equation 27 (11 p. 164).

$$\eta_n = 1 - \zeta_n \qquad - \qquad (27)$$

$$W_{ax,n} = \frac{M_n}{\rho_n An_{n-1}} \, and \, W_{u,n} = \frac{W_{ax,n}}{tan\ \beta_n} \qquad [m/s] \qquad (28)$$

$$\vec{V}_n = \vec{W}_n + \vec{U}_n \qquad \text{[m/s]} \qquad (29)$$

The change of cross-section between the outlet of the blade and the inlet of the next blade must be considered, since this will change the velocity of the fluid. It is assumed that the density remains constant during this step, so the velocity will only change depending on how the area expands.

$$\vec{V}_n = \vec{V}_n * \frac{An_{n-1}}{An_n} \qquad \text{[m/s]} \qquad (30)$$

$$\alpha_n = \operatorname{atan}\left(\frac{V_{ax,n}}{V_{u,n}}\right) \qquad \text{[rad]} \qquad (31)$$

$$|W_n| = \sqrt{{W_{ax,n}}^2 + {W_{u,n}}^2} \qquad \text{[m/s]} \qquad (32)$$

$$|W_{n-1}| = \sqrt{{W_{ax,n-1}}^2 + {W_{u,n-1}}^2} \qquad \text{[m/s]} \qquad (33)$$

$$|V_n| = \sqrt{{V_{ax,n}}^2 + {V_{u,n}}^2} \qquad \text{[m/s]} \qquad (34)$$

With the velocities and the efficiency of the blade fully determined, the isentropic enthalpy for the outlet at this stage is calculated using Equation 35 (11 p. 165).

$$h_{s,n} = h_{n-1} - \left(\frac{|W_n|^2}{2\eta_n}\right) + \frac{1}{2}(|W_{n-1}|^2 - |U_{n-1}|^2 + |U_n|^2) \qquad \text{[J/kg]} \qquad (35)$$

The ventilation losses have been considered in the calculation; these losses can be defined as an energy dissipation process due to the unsteady flow process at the tip of the blade sector. The ventilation power PV can be represented with sufficient accuracy as in equation 36 [10, p.420]:

$$PV_n = \pi C_n (1 - F_{n-1}) \rho_n 2R_{m,n} hb * {U_{u,n}}^3 \qquad \text{[W]} \qquad (36)$$

The ventilation coefficient C depends on the structural arrangement and whether the ring of blades rotates forward or backward; for the MONIKA turbine, the expression is for wreathed, forward flow:

$$C_n = 0.0095 + 0.55 * \left(0.125 + \frac{hb_n}{2R_m}\right)^2 \qquad \text{-} \qquad (37)$$

With the ventilation power and the mass flow, it is now possible to find the energy losses due to the ventilation process.

$$qV_n = \frac{PV_n}{M_n} \qquad \text{[J/kg]} \qquad (38)$$

This calculation also takes into account the losses caused by the partial inlet, these are caused near the edges of the active arcs due to the flow from the inlet into the blocked section, this process is known as emptying, and from the rotor leaving the blocked section (filling), these emptying and filling losses are proportional to the circumferential blade speed $U_{u,n}$ [13].

This method was developed for partial admission in a steam turbine. However, it was not designed for partial admission within stages, which could lead to deviations in the results.

$$qFE_n = \frac{0.21 c a_n U_{u.n} \sqrt{h_{n-1} - h_{s,n}}}{F_{n-1} 2R_{m,n}} \qquad \text{[J/kg]} \qquad (39)$$

The real enthalpy at the outlet of the vane stage was calculated using the values of the relative velocity, the circumferential velocity of the vane, and the previous enthalpy as shown in equation 40 [10].

$$h_n = h_{n-1} - \frac{(|W_n|^2 - |W_{n-1}|^2 + |U_{n-1}|^2 - |U_n|^2)}{2} \qquad \text{[J/kg]} \quad (40)$$

The ventilation losses and filling and emptying losses must be added to the calculated value of real enthalpy.

$$h_n = h_n + qV_n + qFE_n \qquad [\text{J/kg}] \qquad (41)$$

As the enthalpy increases, the power produced by each blade stage decreases, therefore the ventilation losses and the filling and empty losses reduce the power of the turbine as expected.

To find all the fluid properties at the outlet of this stage, it is still missing the pressure at this point, to determine this value it is used the isentropic enthalpy and the previously calculated enthalpy, using these two values and a secant method along with REFPROP, the outlet pressure can be determined [6].

$$P_n = P(s_{n-1}, h_{s,n}) \qquad [\text{kPa}] \qquad (42)$$

With enthalpy and pressure, it is now possible to determine fluid properties with direct functions in REFPROP.

$$s_n = s(h_n, P_n) \qquad [\text{J/kgK}]$$

$$\rho_n = \rho(h_n, P_n) \qquad [\text{kg/m3}]$$

$$T_n = T(h_n, P_n) \qquad [\text{K}]$$

$$X_n = X(h_n, P_n)$$

This density value is used as the input for the next iteration until the blade calculation converges.

Convergence of the method

The procedure described for the vane and blade stages is repeated for all stages of the turbine until the fluid properties are calculated for each cross section. The calculation approach I have chosen, is to iterate the mass flow and provide as input a pressure distribution for each cross section. In the previous steps, the mass flow was determined for each stage, then a pressure correction must be made depending on the relative mass flow difference for each cross section, which means that a pressure array from n=1 to n=number of cross sections is created. The relative mass flow differences are given by

$$dM_n = \frac{M_n}{M_0} - 1 \qquad [\text{kg/s}] \qquad (43)$$

$$M_0 = M_1 \qquad [\text{kg/s}] \qquad (44)$$

The pressure correction is calculated based on the relative mass flow for the next vane stage, except for the measured outlet pressure, then the correction is made for the first three stages only, leaving the pressure values for the cross-sections 7 and 8 unchanged.

$$dP_n = -P_n * dM_{n+2} \ \ where \qquad [\text{kPa}] \ (45)$$

dM_{n+2} $is\ the\ derivative\ for\ the\ next\ vane$

Then the new pressure distribution is:

$$P_n = P_n + dP_n * RF \qquad [\text{kPa}] \qquad (46)$$

The relaxation factor RF must be considered in the calculation to avoid negative pressure values and therefore complex enthalpy values. Once the new pressure distribution is set, the next iteration must be performed again for all turbine cross sections.

The iteration process is controlled by the mass error (Merror), which is the maximum value of the array dM, as soon as this mass error is lower than a previously defined error, it is assumed that the state points of the turbine have been found.

When all the values converge, the total turbine power $Pturb$, the total efficiency η_{turb} and the mass flow can be calculated.

The mass flow M is equal to the converging mass flow from above.

$$Pturb = M(h_0 - h_{ncs}) \qquad [W] \qquad (47)$$

To calculate the global efficiency of the turbine, the specific power produced by the turbine is divided by the isentropic change in enthalpy between the inlet and outlet of the turbomachine.

$$h_{s,outlet} = h(P_{ncs}, s_0) \qquad [W]$$

$$\eta_{turb} = \frac{h_0 - h_{ncs}}{h_0 - h_{s,outlet}} \qquad - \qquad (48)$$

At the end of the calculation, the fluid velocity must be compared with the local sound velocity of the fluid to analyze if the supersonic flow is reached in the different cross sections. When this happens, the cascade can be said to be "choked". This choking limit is relevant to mass flow because it limits the mass flow of the turbine [13].

$$if\ Ma \geq 1\ Supersonic\ flux$$

$$else\ Ma < 1\ Subsonic\ flux$$

The results obtained with the previous procedure, must fulfil a verification and validation based on the design parameters and on the measured data.

Verification with design values

The comparison of the calculated power and mass flow with the designed values shows a deviation of 1% for power and 2% for mass flow.

Validation with experimental data

The comparison of the experimental data from 8.11.21 and 9.11.21 include in the Master thesis of J. Mardon Pérez [7] shows an error in power of max. ± 4% and in mass flow of max. 8%.

Calculation Results

Using the measured turbine data from the 8.11.21 and 9.11.21 test runs, a mean line analysis is performed with a relaxation factor of FR=0.5. In the next figures, the graphs for enthalpy-entropy (h-s), and pressure-specific (P-v) volume are shown.

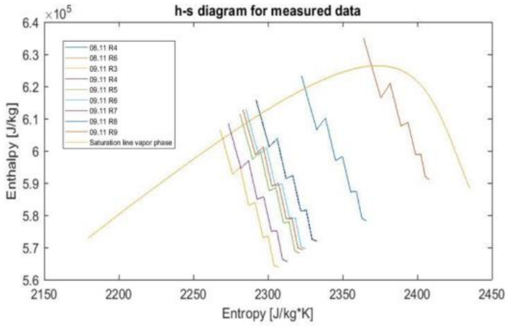

Fig.6 hs diagram

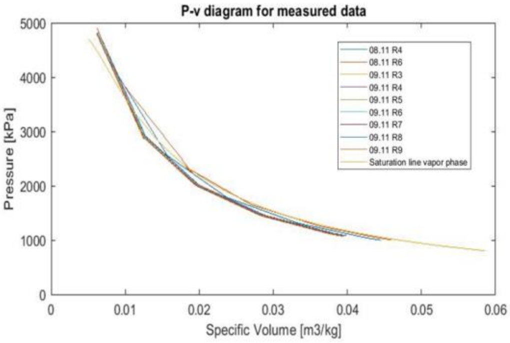

Fig.7 Pv diagram

The above diagrams 6,7 show the evolution of the thermodynamic properties of the working fluid in the different stages of the turbine. It is also noticeable that the behavior of the enthalpy is consistent with an impulse turbine, where the enthalpy drop occurs in the vanes and slightly increases in the rotor blades. Similarly, the pressure in the rotating stages of the turbine remains constant.

In all cases, the fluid is in the two-phase zone shortly after entering the first stage of the vanes, and the fluid vapor quality remains above 0.85.

The comparison between the velocity of the fluid and the velocity of sound is shown in Figure 8. It can be seen that all values are below Mach number one, therefore the fluid does not reach the supersonic condition in any of the cross sections.

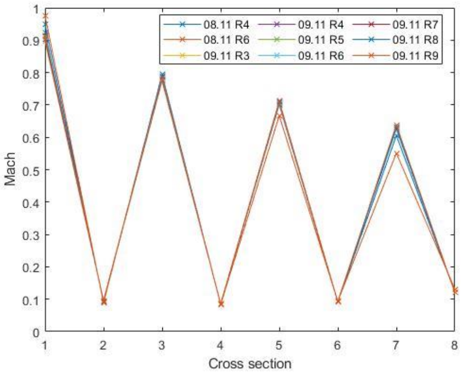

Fig.8 Mach number

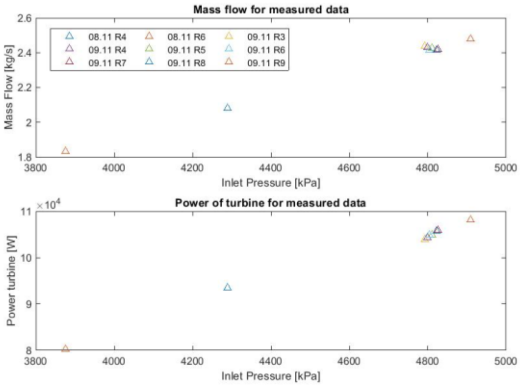

Fig. 9 Mass flow and power of the turbine

Figure 9 shows the impact on both power and mass flow of the fact that the inlet properties are not at supercritical levels, as shown for day 08.11.21, where the inlet properties did not reach this state, reducing the amount of power produced by up to 20 kW.

The calculated turbine power results in values of 83,7 to 96 kW for the inlet values of 8.11.21 and 102,1 to 104,4 kW for the 9.11.21.

The efficiency reaches values up to 78% which was not expected for such a small turbine with partial admission in all stages.

Taking into account all the deviations, it can be concluded that the deviations of the results obtained by the implemented calculation method compared to the measured data are in the range of 4% to -4% for the power produced and 4% to 8% for the mass flow. Therefore, they can be considered accurate enough to be validated and used to predict the operation of the turbine under different operating conditions.

Conclusion

In conclusion, the approach used in the mean line analysis showed that it is possible to determine the properties of the fluid inside the existing turbine from its geometric characteristics and thermodynamic properties at the inlet and outlet of the turbomachine, and that it is possible to verify and validate this method for the ORC turbine of the MONIKA plant, thus predicting its operation under different load conditions.

A better approximation in the calculation can be done by CFD analysis. The results of these calculations then replace the previously used loss correlations in the mean line analysis for each of the load cases.

References

1. Vetter, C., Wiemer, H.-J. and Kuhn, D.; Comparison of sub- and supercritical Organic Rankine Cycles for power generation from low-temperature/low-enthalpy geothermal wells, considering specific net power output and efficiency. Applied Thermal Engineering 51 (2013) 1-2, S. 871–879

2. Vetter, C.; Parameterstudie zur Simulation von Niedertemperatur-Kreis-prozessen (KIT scientific reports) 2011, ISBN 978-3866446731

3. Vetter, C., Wiemer, H.-J.; Dynamic Simulation of a Supercritical ORC using Low-Temperature Geothermal Heat. Melbourne, Australia (2015)

4. DiPippo, R.; Geothermal power plants. Principles, applications, case studies and environmental impact / Ronald DiPippo. Amsterdam: Butterworth-Heinemann 2015

5. Niño Avella, C. L.; Design study of the MONIKA-ORC-Turbine and comparison with experimental results, Master Thesis 2023, KIT-ITES

6. REFPROP 9.0. Reference Fluid Thermodynamic and Transport Properties Database. NIST National Institute of Standards and Technology (2018)

7. Pérez, J. M.; Experimental examination of the MONIKA-ORC Turbine and comparison of the results with thermodynamical calculation, Master Thesis 2022, KIT-ITES

8. M+M Turbinen-Technik GmbH. GT 120-4 Turbine Datasheet.

9. Dixon, S. L.; Fluid Mechanics, Thermodynamics of Turbomachinery ISBN 0 7506 7059 2, Oxford, UK: Butterworth-Heinemann, 1998.

10. Traupel, W.; Thermische Turboma-schinen Thermodynamisch-strömungstech-nische Berechnung, ISBN: 978-3-642-62102-4, Verlag Berlin Heidelberg: Springer, 2001.

11. Müller, H. K. and Nau, B. S.; "www. fachwissen-dichtungstechnik.de," 2003. [Online]. Available : http://www.fachwissen-dichtungstechnik.de/Kapitelseiten/Kapitel17.html. [Accessed 12 January 2023].

12. Berger, A., Polklas, T., Brunn, O. and Joos, F.; "Experimental investigation on performance of a control stage turbine under partial admission Paper ID ETC2019-135," Helmut Schmidt University, Hamburg, 2019.

13. a. d. Wiesche, S., Hake, L. and Cinnella, P.; EXPERIMENTAL AND NU-MERICAL ASSESSMENT OF AN ASYMP-TOTICALLY CORRECT CHOKING MACH NUMBER EXPRESSION FOR ORGANIC VAPOR FLOWS THROUGH TURBINE CASCADES, Paper ID: 83, Munich: 6th International Seminar on ORC Power Systems, 2021.

Department: Hydrogen

Fundamental Behaviour of Hydrogen to Applied Accident Consequence Analysis for Hydrogen as a Safe Energy Carrier

Andrei Denkevits, Andreas Friedrich, Joachim Grune, Olaf Jedicke, Thomas Jordan, Birgit Kaup, Alexei Kotchourko, Mike Kuznetsov, Alexander Lelyakin, Gottfried Necker, Marco Ordonez, Frank Prestel, Jeremy Rietz, Torsten Schuler, Karsten Sempert, Eugenio Torres de Ritter, Jianjun Xiao, Zhanjie Xu, Fangnian Wang

Introduction

The Hydrogen Department continued to develop models and in-house specialized reactive CFD codes (GASFLOW and COM3D) and conducted an extensive experimental program to deepen the understanding of the behavior of hydrogen in postulated accident. Recently accidental behaviour of cryogenic hydrogen became the focus of this research work. However, the team members also intensified transferring their insights and expertise into standardization, academic education and public consultation services.

Thus, this yearly report highlights ome research work related to the safety of liquid hydrogen cryostats and the development of hydrogen pilot projects for the Fessenheim innovation region. Then it summarises some extraordinary events.

Safe Liquid Hydrogen Storage

Liquid hydrogen is stored in cryostats at temperatures around -250°C. Despite vacuum insulation and radiation heat shielding there is always some heat transferred from the relatively “hot” environment into this cryogenic inventory. So, the containers have to limit temperature and pressure increase by venting the so-called boil-off.

If the vacuum is broken in a Loss Of Vacuum Accident (LOVA) the heat transfer increases seriously. The safety valve which will be activated then has to account for remaining heat insulation. To improve the understanding of the complex processes of air ingressing into and condensating in the gap between vacuum and pressure vessel cryogenic the special test facility PICARD (Pressure Increase in Cryostats and Analysis of Relief Devices) has been refurbished to accommodate liquid hydrogen and a corresponding modelling effort was started in 2022.

Setting Up the Experimental Infrastructure

The PICARD facility was originally designed and constructed by the Institute of Technical Physics (ITEP) at KIT. The facility mainly consists of a vacuum-insulated cryogenic vessel whose vacuum shield can be broken rapidly by opening a ball valve with customable inlet orifices. The cryogenic vessel is connected to a release branch with a safety valve, in which the volume flow of evaporated cryogenic liquid can be determined via a Venturi tube, before the flow is conducted to a collecting line via an exhaust pipe. In its original configuration the PICARD facility was used to measure the performance of safety valves for vacuum insulated tanks. In these experiments, the cryogenic fluid was liquid helium (LHe) that was collected after evaporation and re-used. After the end of this experimental series the PICARD facility was provided to the Hydrogen Department of ITES, where it is used to perform vacuum break tests for liquid hydrogen (LH2) cryostats developed for aviation.

In the tests the efficiency of different superinsulation layer thicknesses, that shields the cryogenic vessel against radiation, will be investigated. During the experiments, LH2 evaporates to form gaseous hydrogen (GH2), which is different than helium highly flammable and easily forms explosive mixtures with air. Furthermore, the evaporated hydrogen will not be collected and re-used but released into the ambience during the experiments.

Due to these changes in the test conditions from helium to hydrogen, several modifications became inevitably for safety reasons. First of all, the facility had to be transferred to an open-air test site, where all evaporating hydrogen can be vented through a stack to the ambience without generating any hazards to the environment. Due to the large mass of gaseous hydrogen that has to be released from the facility in an experiment, the initially planned location for the modified PICARD facility behind KIT-HYKA had to be abandoned, since air intake openings of a new neighboring building were found to be too close in this configuration.

After the facility had been transferred to the free-field test site in Hochstetten, where no adjacent inhabited buildings exist, additionally a stack with a height of 12 m was erected and connected to the exhaust line of the PICARD facility for a safe disposal of the expected boil-offs.

The later described pre-calculations of the release behavior from the facility after a vacuum break revealed that the Venturi-tube for measuring the release volume flow might be oversized to measure the most important parameter of the experiments with the desired accuracy. So already during the relocation of the facility, a suitable Coriolis flow meter was ordered, but unfortunately this device had a long delivery time of more than 6 months. To minimize project delays it was decided to start with reference experiments without superinsulation, for which the highest boil-off rates and thus volume flows were expected. With the first delivery of LH2 two reference experiments

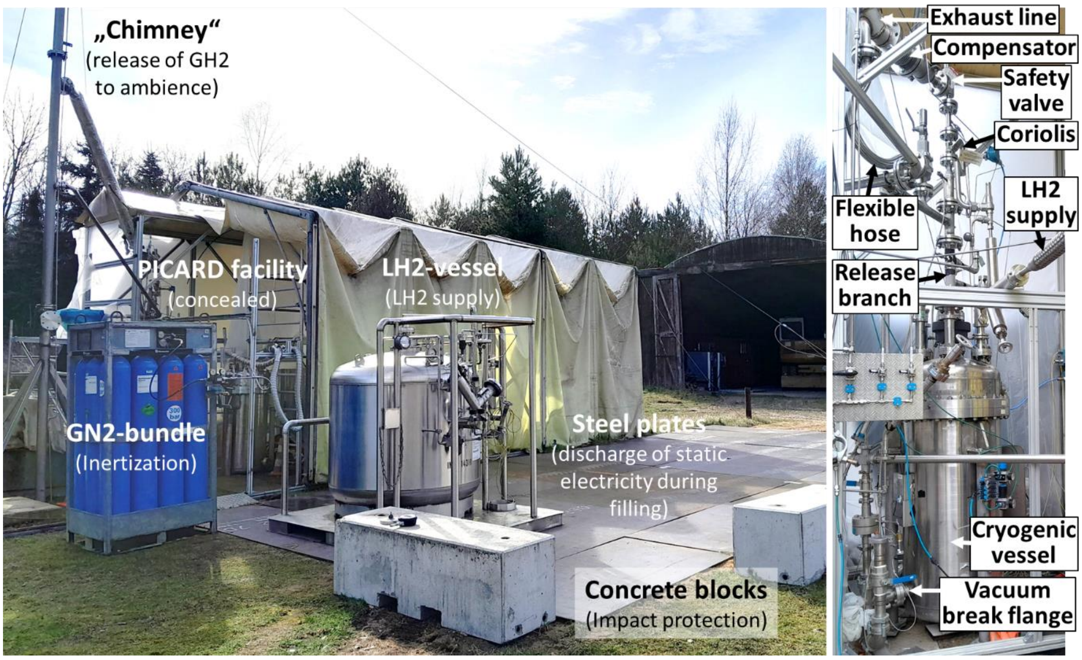

Figure 1. Overall view of the modified PICARD facility on the free field test site in Hochstetten (left) and details of the facility (right).

were performed after which the integration of the Coriolis flow meter was begun. Due to the smaller pipe diameter of the Coriolis flow meter, large parts of the release branch and its connection to the exhaust pipe had to be reworked. In first tests after its integration, it was discovered that the new device measures faulty and irreproducible values and a systematic investigation showed that the faulty signals originate from stresses in the thin probe that are caused by its connection to the heavy exhaust pipe. Although these stresses can be eliminated by precisely aligning the pipes at ambient temperature, it is to be expected that these faults can never be completely eliminated, as there will be immense temperature fluctuations in the exhaust pipe in every experiment. To overcome this problem one compensator and a flexible hose for the two connections of the release branch to the exhaust system were ordered and installed. In the new design the Coriolis flow meter worked properly, but by the time the facility could be put into operation again, the LH2 supplier had stopped the service and no substitute LH2-supplier could be found.

Modelling LOVA

To support the proper set-up of the experiments with the PICARD facility, to extrapolate the results of the planned experiments with regard to the behaviour of the radiation shield in different tank designs and to provide basic data for a proper safety valve design a modelling activity has been started at the hydrogen department.

Figure 2 provides a simplified scheme of the PICARD facility during a test, or in general a LH2 cryostat under air-sided vacuum break conditions.

As shown in figure 2, the LH2 cryostat consists mainly of the cryogenic inner "pressure" vessel and the outer vacuum vessel. The inner vessel contains liquid hydrogen in 80 % of the total volume and gaseous hydrogen in 20 % at the saturation state with a pressure of 4 bar and temperature of 26 K. On the top of the cryostat there is a valve to vent the boil-off, which represents in a conventional LH2 cryostat the safety valve. The outer vessel isolates the storage tank from the environment and forms the vacuum space together with the cryogenic vessel. To improve the thermal insulation, a multi-layer-insulation (MLI) system is wrapped loosely around the cryogenic vessel, which is made of up to 50 layers of very thin aluminum foils separated by spacers made of microfibers.

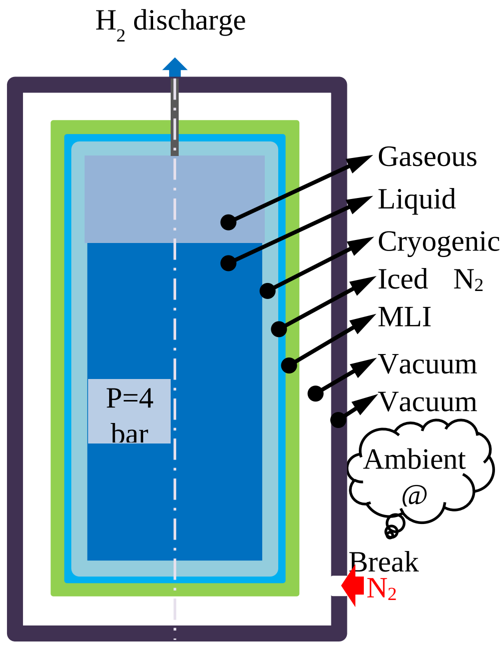

Figure 2. Scheme of the test facility of the LH2 cryostat in a LOVA

Important assumptions are made as follows for the following modelling work.

- Initiation of LOVA is assumed a break on the vacuum vessel wall (air ingress)
- Ingressing gas is assumed pure nitrogen for lack of suitable data of air at these conditions (error estimated < 10%).

The ingressing nitrogen gas experiences phase changes, condensation and freezing, due to the cryogenic condition on the steel wall of cryogenic vessel or even in some inner layers of the MLI. This phase changes release considerable latent heat. As the temperature is mostly below the triple point of nitrogen, desublimation may occur while gas molecules deposit on the solid surfaces. The loose structure of the MLI is not gas tight at all. Therefore, nitrogen condensation and freezing might happen there also.

The dynamic process of the heat and mass transfers in the LOVA scenario is studied then by simplifying the above scheme further to a axissymmetrisch one-dimensional problem along the radius, reaching from the inner LH2 to the outer vacuum vessel. The problem is then discretised into concentric shells, where especially the inner cryogenic wall and the MLI are represented with a reative large number of cells – the MLI got 1 cell per layer and the cryogenic vessel wall was divided into 10 cells, respectively nodes. Then energy and mass are balanced in each cell and heat transfer and phase transitions are modelled with established engineering correlations.

The resulting lumped parameter model has been applied to the PICARD experiments with typical initial conditions. A part of the simulation results highlighting the transients of solid nitrogen deposition and radiative and convective fluxes are depicted in Figure 3. The results were further used to design suitable measurement devices mainly for pressure evolution and boil-off mass and volume flow for the actual experiments.

The lump parameter model on heat and mass transfers are able to predict reasonably well the thermal load on the LH2 contained in the PICARD cryostat during a loss of vacuum accidental (LOVA) scenario. The model accounts for the characteristics of the multi-layer insulation, accounts for the freezing of nitrogen, the convection in the vacuum enclosure and the pool boiling heat transfer in the cryogenic vessel. The simulations show that the nitrogen, respectively air deposition dominates the contributions to the thermal loads to the LH2. The convection and thermal radiation play significantly less roles.

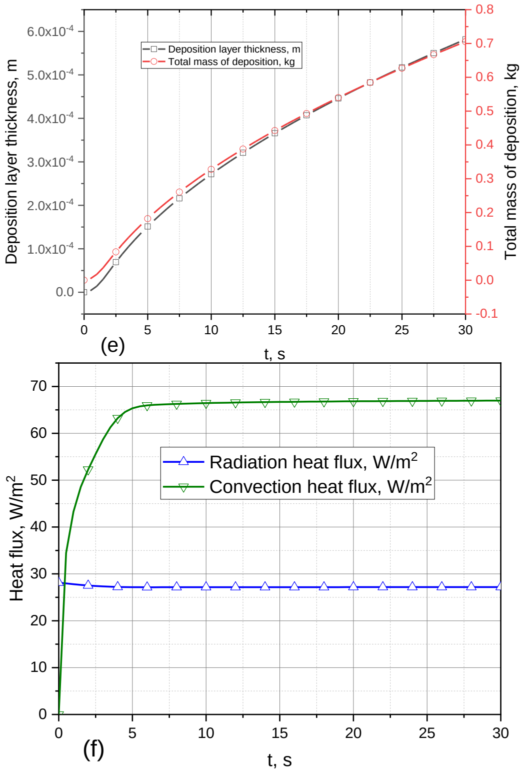

Figure 3. Transient parameter evolutions in the PICARD LH2 cryostat in the first 30 s of a LOVA, thickness of nitrogen deposition (top), radiative and convective heat flux (bottom)

So, this model may predict the accidental behaviour of the MLI in a LOVA and therefore allows proper safety valve design for any cryogenic vessel resembling the generic design used for PICARD. However, some adaptations might be needed for horizontally installed or form-free cryostats and for new construction materials, in particular non-metallic compound materials. Furthermore, the effect of oxygen and humidity in the ingressing gas mixtures has to be studied.

Hydrogen Pilot Projects for Fessenheim

As part of the feasibility study, a concept for the Innovative Region and, based on this concept, different lines of action for Franco-German demonstration projects for the Fessenheim Innovative Region have been developed. The overall objective is to develop a sustainable and forward-looking CO2-neutral economic region. The transformation of society and the economy towards a renewable energy supply and a sustainable use of resources, combined with the creation of future-oriented jobs, will be strongly promoted by implementing hydrogen as an energy carrier. Green hydrogen allows almost immediate replacing of fossil fuel based hydrogen in industrial processes, seasonal storage of renewable electricity and allows to couple different energy sectors in a flexible and efficient way.

The hydrogen department represented by its head Thomas Jordan was coordinating the development of the specially adapted pilot projects, forming the basis of a regional hydrogen hub. Key hydrogen technologies shall be demonstrated in an integrated way, coupled with the smart electricity grid, battery technologies and storage and infrastructural also with the other innovative energy technologies. The pilot projects cover the whole value chain from production, storage, transportation and use of “green” hydrogen. The projects themselves and the selection of applied technologies account for the specific characteristics and assets of the concerned region and introduce the most promising and realistic sequence for their adoption. The initial large industrial use of hydrogen will provide the required scale for cost reduction and prepare the ground for a more distributed use. The diverse regional opportunities for green hydrogen production via electrolysis and from biomass are addressed. As importing and exporting hydrogen will be an economic necessity, appropriate transport schemes via pipelines and batch transport on roads and on the river Rhine are suggested. Multi-modal transport will be accomplished with a fleet of hydrogen driven heavy duty trucks. Finally, the transformation of agriculture into a green hydrogen producing and using, self-sustained economic sector will be demonstrated with appropriate and mature approaches.

Besides the demonstration of technologies with high maturity the hydrogen hub should also provide opportunities for research and development, testing of new innovative solutions, sub-systems or components under most realistic conditions.

Anyway, key success factor will be the viability of a business case for the first private up-takers and the commitment of the public to support the development of the required infrastructure, all on a robust and targeted regulatory framework.

Special Activities and Events

HySafe RPW2022

The HySafe Research Priorities Workshop (RPW) takes place every even year. The 2022 edition was held in Quebec City, Quebec on November 21 – 23, 2022. RPW addresses the pre-normative research tackled by the members. Presented within the report are the extended abstracts provided by the attendees. Participants asked to prioritize the topics and subtopics. These data clearly show the level of importance for the different categories addressed in the workshop.

1. Accident physics of liquid / cryogenic behavior is on top followed closely by Mitigation Sensors, Hazards prevention and Risk.
2. A sharp drop in the priority for Integrated Tools probably represents the fact that many such tools currently exist for use by the industry.
3. While there is still much to be understood about hydrogen effects on materials, the group ranked that about in the middle with a score of 5.5.
4. Accident physics for the Gas Phase ranked pretty low. This is a topic that the pre-normative effort has been spending significant effort on over the past many

years. The ranking clearly mirrors that the topic is reasonably well understood.

5. Applications followed by storage and general aspects of Safety make up the bottom three levels.

This workshop was excellent in bring out the gaps and directions the research community feels are important.

State Advisory Board Hydrogen Technology

Thomas Jordan member of the state advisory board for Hydrogen Technology and its safety. In a so-called "seven-point plan", the advisory board presents concrete recommendations for action for the upcoming update of the Baden-Württemberg hydrogen roadmap.

Kick-Off Meeting GreenSkills4H2

The ERASMUS+ Project GreenSkills4H2 took place in Brussels July 2022. The project will get carried out by 34 partners and associated partners from industry. The focus of the project is to support skills and education facing hydrogen technology and safety. In these light objectives are to identify the demands (manly industry), to develop specific educational materials and course curricula and to provide and execute seminars and schools facing thematic priorities identified. KIT demands and aspect to develop hydrogen technology courses further included. Overall Coordinator of the project Olaf Jedicke. The project duration is 48 months and will last until 2026.

Partner

We would thank Anke Veser from Pro-Science GmbH and Natascha Kotchourk from Co-Study GmbH for the good work, which they have done.

References

[1] Morawska, L., et al., “How can airborne transmission of COVID-19 indoors be minimised?”, Environ. Int., vol. 142, no. April, 2020.

[1] Lowen, A. C., et al., “Influenza virus transmission is dependent on relative humidity and temperature”, PLoS Pathog., vol. 3, no. 10, pp. 1470–1476, 2007.

[2] Morawska, L,.et al., “It Is Time to Address Airborne Transmission of Coronavirus Disease 2019 (COVID-19)”, Clin. Infect. Dis., vol. 2019, no. 9, pp. 2311–2313, 2020.

[3] Xiao, J., et al., GASFLOW-MPI: A Scalable Computational Fluid Dynamics Code, VOLUME 1: Theory and Computational Model, Revision 1.0, KIT Scientific Report Nr. 7710, KIT Scientific Publishing, Karlsruhe, ISBN: 9783731504481, April, 2016.

[5] Innovationspool-Projekt 2021-2023 des FB Energie – Programm MTET Zukunftsthema „Solarer Wasserstoff – hochrein und komprimiert (Solarer Wasserstoff)“, FB Energie – Innovationspool 2021 – 2023: Zukunftsthema „Solarer Wasserstoff“, 15th, May, 2020.

[6] Geißler, T., Abánades, A., Heinzel, A., Mehravaran, K., Müller, G., Rathnam, R.K., Rubbia, C., Salmieri, D., Stoppel, L., Stückrad, S. and Weisenburger, A., 2016. Hydrogen production via methane pyrolysis in a liquid metal bubble column reactor with a packed bed. Chemical Engineering Journal, 299, pp.192-200.

[7] Ohi, J.M., Vanderborgh, N., Consultants, G.V., Ahmed, S. and Kumar, R., 2016. Hydrogen fuel quality specifications for polymer electrolyte fuel cells in road vehicles. Office of Energy Efficiency and Renewable Energy: Washington, DC, USA.

[8] Xiao, J., Breitung, W., Kuznetsov, M., Zhang, H., Travis, J.R., Redlinger, R. and Jordan, T., 2017. GASFLOW-MPI: A new 3-D parallel all-speed CFD code for turbulent dispersion and combustion simulations: Part I:

Models, verification and validation. International journal of hydrogen energy, 42(12), pp.8346-8368.

Links

[1] https://hysafe.info/wp-content/uploads/2023/09/RPW_2022_Final_Report.pdf

[2] https://um.baden-wuerttemberg.de/de/energie/energiewende/wasserstoffwirtschaft/beirat-wasserstoff-roadmap-bw

[3] https://greenskillsforhydrogen.eu/

Department: Framatome Professional School

CFD Validation Of Forced And Natural Convection For The Open Phase Of IAEA Benchmark CRP - I31038[1]

Abdalla Batta, Andreas Class

Abstract

The goal of the IAEA Coordinated Research Project “Benchmark of Transition from Forced to Natural Circulation Experiment with Heavy Liquid Metal Loop” (CRP - I31038) is to develop Member State advanced fast reactor analytical capabilities for simulation and design using system, CFD, and subchannel analysis codes. Here we present CFD validation employing the commercial CFD code Star CCM+ applied to the fuel pin simulator for forced and natural convection cases in the open phase where experimental data is provided in the benchmark specification provided by ENEA (Italian National Agency for New Technologies, Energy and Sustainable Economic Development) for the NACIE-Up facility (NAtural CIrculation Experiment-UPgrade). Considered is the fuel pin simulator with 19 pins, each consisting of a preheated lower section and heated upper sections, respectively. Three configurations (i) all pins heated, (ii) inner 7 pins heated and (iii) asymmetric heating are studied. For each heating configuration data for forced and natural convection are provided. Here case (i) is studied. Temperatures at three planes are measured near the inlet, in the middle and near the end of the heated section, respectively. In addition, the axial temperature along the wall of one fuel pin simulator (in second row) is measured so that in total 67 thermocouples measure fluid and wall temperatures for validation purposes. Our validation confirms that the thermohydraulic inside the fuel pin simulator can be simulated with a good accuracy. Applied is a polyhedral mesh with 2 prism layers, the k-omega SST model with all all-wall treatment and order unity y+ values. Moreover, we performed a grid-sensitivity study and analysed the importance of conjugate heat transfer inside the fuel-pin simulators and the wrapper. Our studies indicate that it is possible to implement further simplifications without corrupting the accuracy of the simulation to reduce computational effort

Keywords: CFD, Liquid metal thermal hydraulic, Turbulence flow, Wire-wrapped bundle flow

Introduction

Benchmark studies are an essential tool to obtain confidence in simulation capabilities when large thermal loads occur. In particular, for nuclear applications, where failure can be accompanied with hazards to the public, maximum temperatures must be limited, and yet compact solutions must be achieved.The ENEA Brasimone Research Centre (Italy) proposed for a benchmark exercise intended for system-alone, CFD/TH system code coupled simulations and stand-alone CFD simulations based on experimental results obtained from the 2017 campaign performed with the NACIE-UP (NAtural CIrculation Experiment- UPgraded) facility, [1], Fig. 1 shows the schematic representation of the NACIE-UP facility consists in a

---

[1] Paper held at SCOPE – Saudi International Conference on Nuclear Power Engineering, November 13 – 15, 2023 – KFUPM, Paper 23031

rectangular loop. It consists of two vertical pipes with an inner diameter of 62,68mm. The working fluid is Lead Bismuth Eutectic (LBE), a fluid proposed for liquid metal cooled fast reactors. The experiments allow operation in the regimes of forced and mixed convection by combining a gas-lift pumping and buoyancy.

Inside the loop a fuel pin simulator (FPS) simulating a 19-pin fuel bundle is installed. Each pin-simulator contains an ohmic heater which can be activated individually, resulting in a maximum total heating power of 250 kW. The heated pins are arranged in 3 ranks with a triangular pitch (P) and with an active length L_{active} = 600 mm. The pins have a diameter D_{pin} = 6.55 mm and maximum wall heat flux close to 1 MW/m^2. The wire diameter d_{wire}=1.75 mm. The pins are placed on a hexagonal lattice by a suitable wrapper, while spacer grids will be avoided thanks to the adoption of the wire spacer. The primary loop is insulated to ensure well-defined adiabatic experimental conditions.

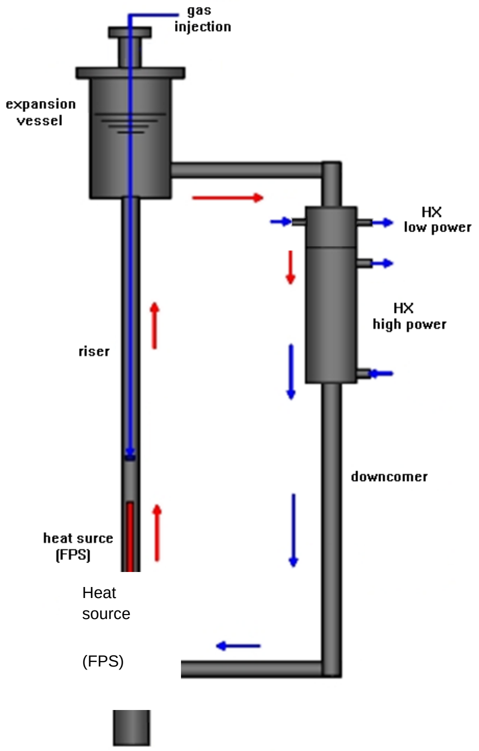

Fig. 1: Schematic representation of the NACIE-UP primary loop [1].

The 19 wire-spaced electrical pins are arranged in a triangular lattice by the hexagonal wrapper. The pitch to diameter ratio (P/D) is 1.2824. The total length, which includes the non-active length and the electrical connectors, is 2000 mm. The dimensions of the FPS are summarized in table I

Table I : FPS design parameters [1]

Parameter	Value
D_{pin}	6.55 mm
P	8.4 mm
P/D	1.2824 mm
d_{wire}	1.75 mm
P_{wire}	262 mm
L_{total}	2000 mm
L_{active}	600 mm
$D_{H,nom}$	3.84 mm

In the open phase of the benchmark two symmetric heating configurations are studied. Test ADP10 corresponds to the activation of heating of all pins, while in the case ADP06 only the central and the second inner row are activated. The goal of the open phase is to set-up first simulations and choice of suitable models and computational parameters. In phase two a complex situation corresponding to asymmetrical heating is to be studied. Researchers do not receive any experimental data during the blind phase. The aim is to demonstrate that computational methods allow predictions once the researchers could validate their implementation for a small number of cases.

Note that each FPS heating configuration is experimentally investigated for a transient. The starting point of operation is a stationary forced convection state which is followed by a pump down-ramping resulting in a stationary natural-convection operation. Thus, each of the test cases ADP10, ADP 06 and ADP07 shown schematically in Fig. 2 acquired data for two steady states. In the current study we consider the case ADP10 for both forced and natural convection. Note that Fig.2 also indicates the numbering of rods and subchannels. In Fig. 3

details and dimensions of the vertical FPS are shown. The flow enters at the bottom of the test section to flow through an unheated preconditioner section located within the lower half of the vertical arrangement. The heated section follows the preconditioner section beginning at height z=0mm, as shown in the figure.

In Fig. 4 positions of the thermocouples in the experimental setup are depicted. The experiment is equipped with three measurement planes (A,B and C) at heights 38mm, 300mm and 562 mm where both wall temperatures (i.e. red dots in the right figure) and subchannel temperatures (i.e. blue dots in the right figure) are collected.

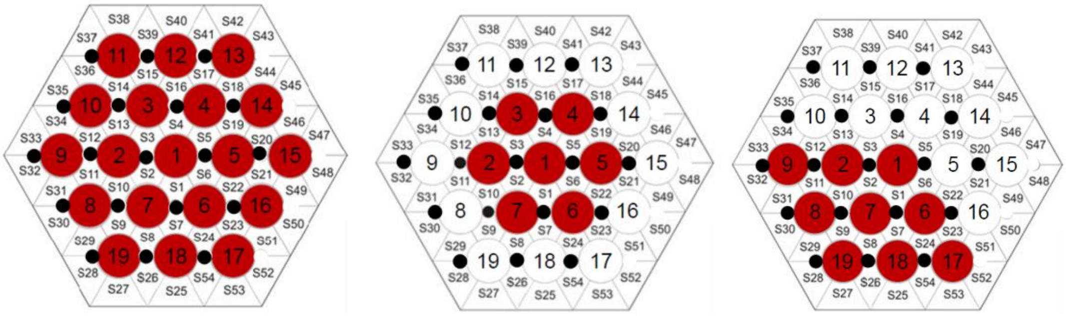

ADP10 ADP06 ADP07

Fig. 2 Bundle cross section, benchmark test cases ADP10, ADP06 and ADP07, active pins (in red) during test.

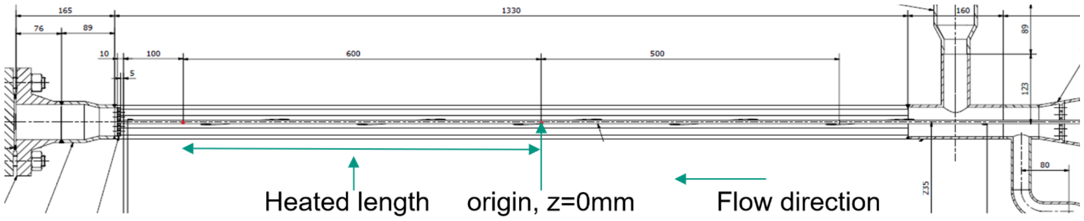

Fig. 3 CAD drawing of the test section and origin of the used coordinate system [1].

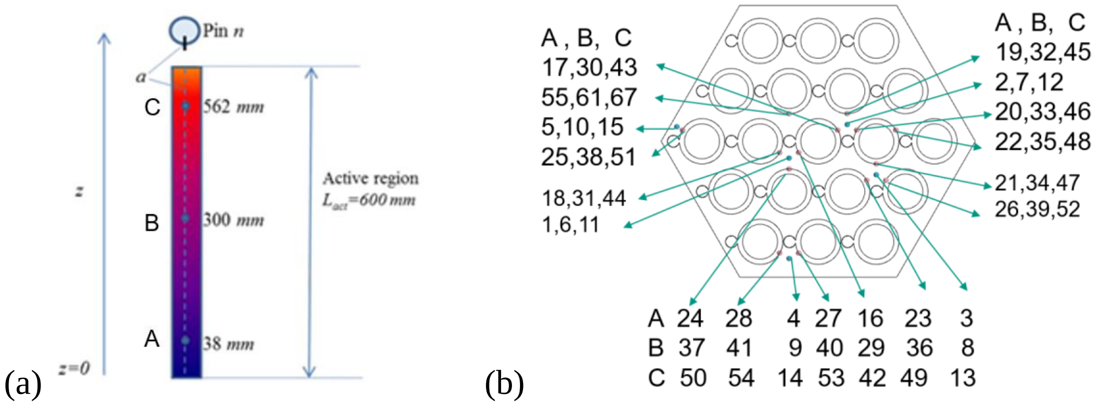

Fig. 4 (a) Location of planes for TC measurements in the test section (A at 38mm, B at 300mm and C at 562mm) (b) location and names of thermocouples in measurements planes.

In addition, rod 3 is equipped with 10 (plus 3 in the measurement planes) thermocouples to measure the axial surface temperature, TC number from 55 to 67, see Fig. 4. The 13 thermocouples on pin 3 are arranged inline. The temperature data at the thermocouples along with integral operational data serves as the benchmark data. The reader is referred to benchmark specifications in [1] for more details.

Table II contains the integral operational conditions of the steady state conditions 1 and 2, corresponding to forced and natural convection, respectively, case APD10. The table also includes error estimates for the integral parameters. As forced convection is provided by the gas-lift pumping the LBE mass flow shows an error of up to 11%, this uncertainty with other ones are relevant for later assessment of prediction capabilities. Moreover, the heating is not fully restricted to the heating section as the fuel pin simulators also show some heating in the preconditioning section. Consequently, the effective heating in the heated section Q_{eff} and the Q_{pre} in the preconditioning will be considered in the simulations. The Q_{tfm} is the power supplied for thermos-flow meter upstream of the test section. Q_{tfm} need not to be considered in the simulation. All simulations should have temperature at the FPS inlet ($T_{in,FPS}$) of the value tabulated in table II. This temperature is the average temperature at z=0.0, the start of heating zone.

Table II Integral parameters of the test ADP10. [1]

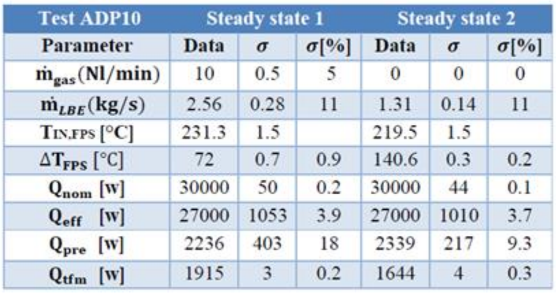

Test ADP10	Steady state 1			Steady state 2		
Parameter	Data	σ	σ[%]	Data	σ	σ[%]
$\dot{m}_{gas}$(Nl/min)	10	0.5	5	0	0	0
$\dot{m}_{LBE}$(kg/s)	2.56	0.28	11	1.31	0.14	11
$T_{IN,FPS}$ [°C]	231.3	1.5		219.5	1.5	
ΔT_{FPS} [°C]	72	0.7	0.9	140.6	0.3	0.2
Q_{nom} [w]	30000	50	0.2	30000	44	0.1
Q_{eff} [w]	27000	1053	3.9	27000	1010	3.7
Q_{pre} [w]	2236	403	18	2339	217	9.3
Q_{tfm} [w]	1915	3	0.2	1644	4	0.3

In [1] the details of the geometric setup of the fuel pins and recommended physical properties of materials are presented. These data are taken from the OECD handbook [2]. Note, that the fuel pin simulators are composed of multiple layers. The outer stainless teal cladding (AISI316L with physical properties in [3]) is followed by an electrical insulating Bohrium Nitride layer [4]. Inside this heat conducting BNi-layer are three more layers corresponding to an Inconel600 (very thin layer, properties for steel are used for Inconel) pipe and an inner copper rod separated by another BNi layer, properties are found in [4]. Time resolved experimental data of all thermocouples is provided in separate excel files not included in the benchmark specification.

Numerical Model and results

For the simulation of the benchmark defined above, the previous experience gained at KIT is employed, see [5-8]. In these validation cases experiments for liquid-metal cooled rod bundles are considered

Fig. 5 shows the used computational domain. It depicts the extent of the fluid domain and the domains for simulation of heater and wrapper. An adiabatic condition is applied thus neglecting heat losses to the environment. Two trials for the simulation of the heater have been undertaken. In the first run a heat flux is imposed on the inner side of the cladding. This represents a simplified model for a short heater, i.e., excluding preheating in the preconditioning zone. In the second trial full details of the heater layers are simulated as shown in Fig. 5 (right). The fluid domain includes the full preconditioning section. Solid structures representing the rods in the preheat zone are excluded. Conjugate heat transfer to the rods and wrapper is accounted for. The mesh for the short heater case is composed of 49 M (Million) fluid cells and 13 M solid cells (mesh I). The mesh for the long heater case uses 96 M fluid cells and 29 M solid cells for the heater and wrapper (mesh II). See Fig. 6 for cross sections of the used meshes.

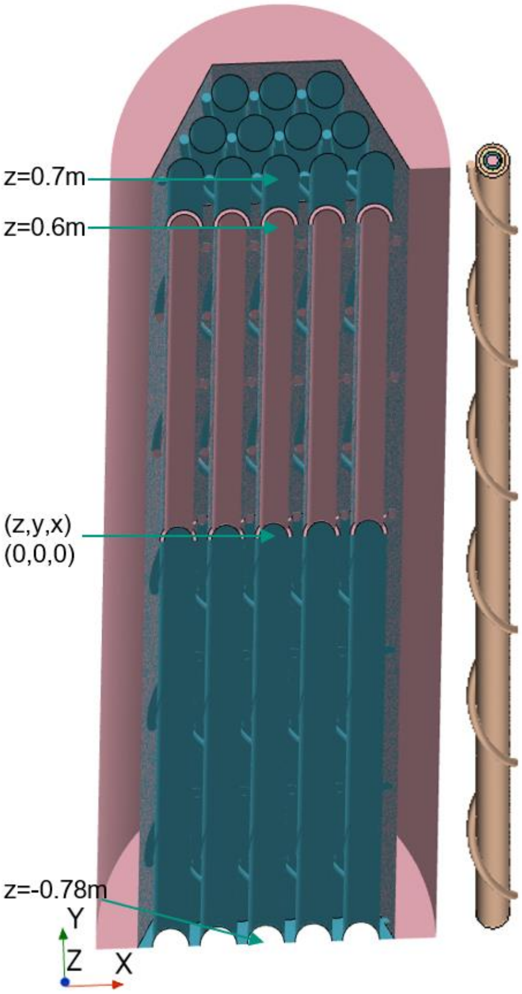

Fig. 5 Computational domain with short, simplified heater (left) and detailed simulated long heater (right).

In this study the flow conditions correspond to the two steady state phases of ADP 10 presented in table II are used. The Star CCM+ CFD code is used. The SST turbulence model with all y+ wall treatment is selected. Material properties according to the benchmark specifications are used, see upper sections. The gravity effect was accounted for in all the calculations. Temperature dependent physical properties are applied. The inlet condition was set according to table II. For the short heater case the preheating was not considered. Consequently, at the inlet of the computational domain the temperature of the FPS inlet temperature according to table II was set. For the longer heater case the preheating is considered. Accordingly, the inlet temperature was set such that FPS inlet temperature becomes equal to the specified value in table II. For the forced convection case short and long heater tests with their corresponding meshes were tested. For the natural convection case only mesh II and the long heater are considered.

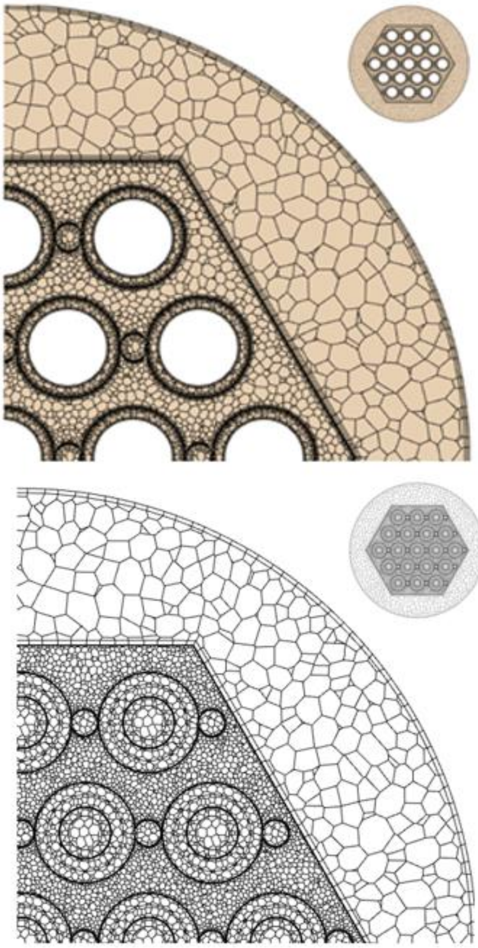

Fig. 6. Cross section of meshes used in simulation. Upper is mesh I and lower is mesh II.

Fig.7 shows the resulting Y+ values for the steady state case 1 using mesh II. Near similar Y+ values are preserved for the simulation with mesh I by adjusting the cell size near the walls. The assigned values are suitable for SST and the used wall function treatment.

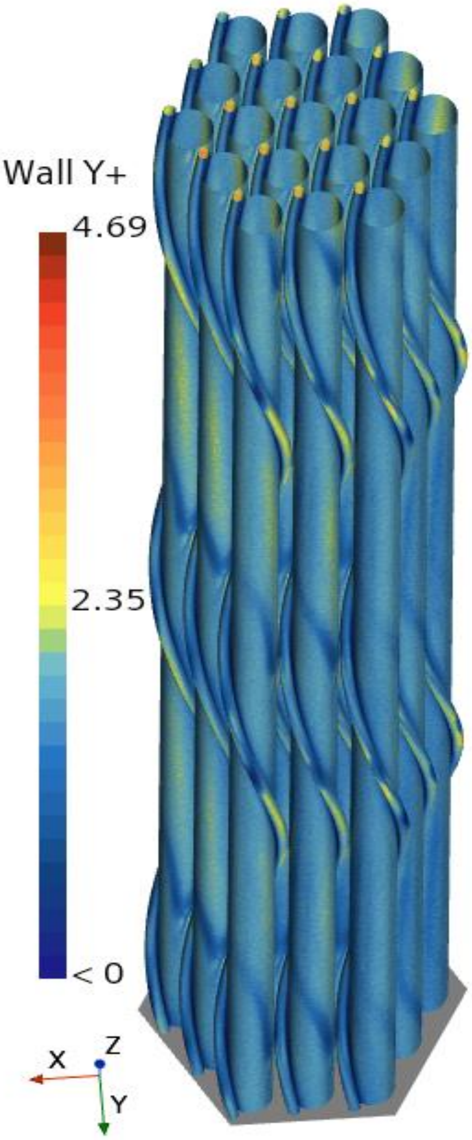

Fig. 7 Y+ values, mesh II, ADP 10 case steady state1.

Fig. 8 shows temperature contours at the heater fluid interface in the heated region (z=0.0 to .0.6 m) for ADP10 case steady state1 and mesh II. The temperature field exhibits a strong temperature gradient in all special directions. Note that the FPS inlet temperature is nonuniform due to the preheating. Thus, near the wrapper wall lower temperatures than average are obtained. The average inlet temperature of the heated section is 231.3C=503.45K. The scale in Fig. 8 starts from 499 K which is the lowest local temperature in the selected domain.

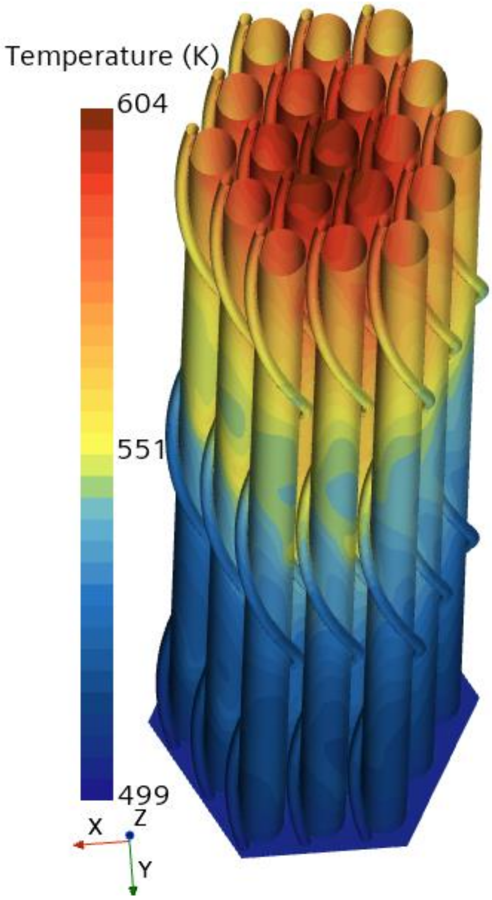

Fig. 8 Temperature contours at heater fluid interface in the heated region, z=0.0 to .06 m. ADP 10 case steady state1, mesh II.

Fig. 9 shows some streamlines originating from a line in the x-y plane (measurement section A, z=0.038m). It highlights strong mixing induced by the wire-wraps. The streamlines are colored by the temperature in their positions.

Local temperature comparisons between benchmark experimental results and simulations are presented in Fig. 10 (forced convection) and Fig. 11 (natural convection). In Fig. 10 and 11 the TC numbers employ the numbering indicated in Fig. 4. TC 1-5, 6-10, and 11-

15 measuring fluid temperatures in the subchannels are located in measurement planes A, B, and C, respectively. Similarly, TC 16-28, 29-41, and 42-54 measuring wall temperatures are installed in the planes A,B, and C, respectively. Finally, TC 55-67 represent the wall temperature measurements along pin 3. They are equally distributed with an axial pitch of 43.7 mm starting from z=38 mm.

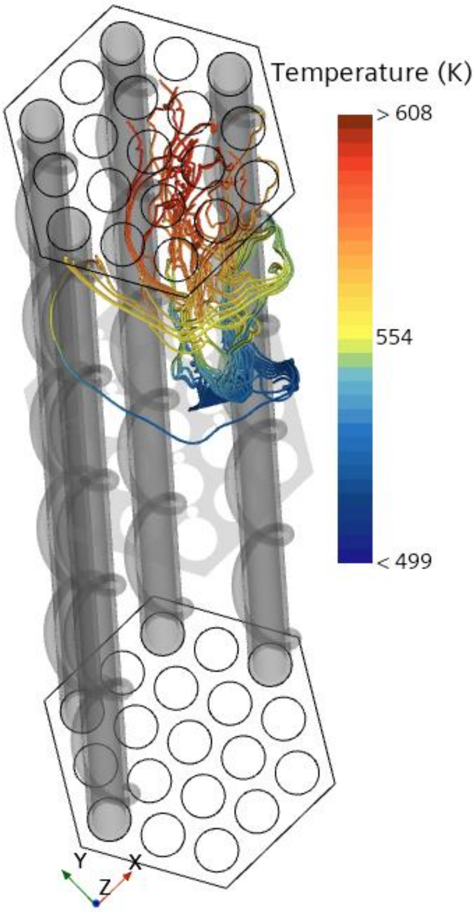

Fig.9 Streamlines originating from a line in x-y plane just downstream of the start of the heated zone, z=.0.038m, case ADP 10 steady state1, mesh II.

Fig. 10 shows the numerical results obtain with the different heater models compared to experiential data. The experimental data have been published and discussed in conference and international journal [9][10][11]. Fig. 10 shows the corresponding experimental results for the steady state case 1 The broken TC number 9 is excluded from the benchmark. The comparison indicates a minimal effect on the numerical results obtained for the short and long cases and even for the more detailed geometry and mesh refinement. Moreover, it proofs a very weak effect when doubling the mesh size. Accordingly, based on the gained experience in the forced convection case, the study of the natural convection case employs mesh II and the long heater geometry. The refined mesh was selected in natural convection simulation for better simulation of the gravitational term, which needs more cells near heated surfaces than for the forced convection. In Fig. 11 results for the natural convection case are compared to the experimental benchmark results.

Even though, deviations are noticeable at all TCs and between the applied models the deviations are rated as acceptable. This is in particular the case, considering the experimental uncertainties in table II.

In measurement plane A the relative error appears to be quite large. Note, that at this plane the effect of the preconditioning is rather large. Therefore, the actual inlet conditions to the heated section exhibit a large experimental uncertainty. Due to the mixing within the rod bundle this uncertainty becomes less important along the bundle.

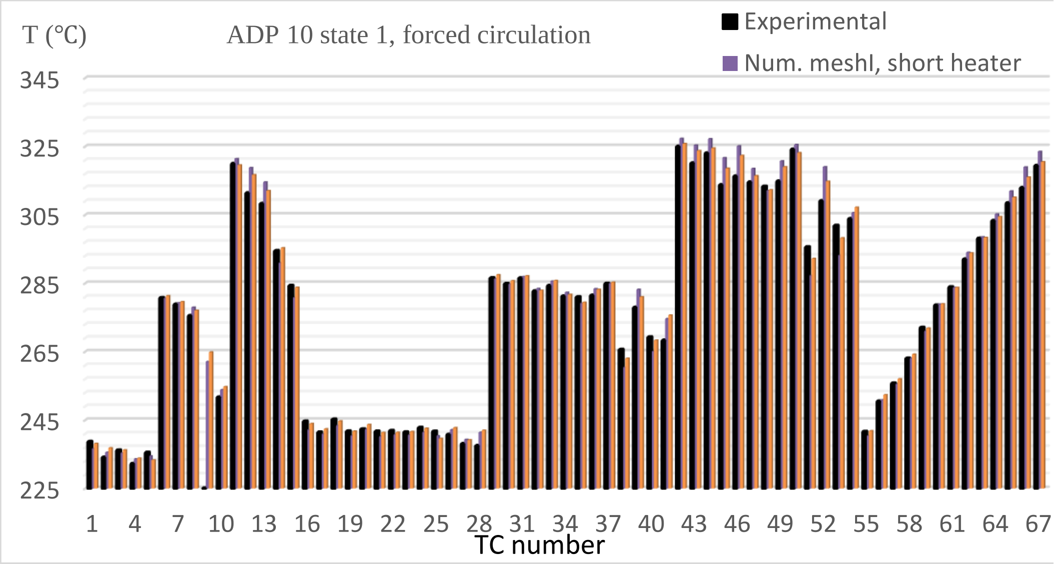

Fig.10 Forced circulation results mesh I with short heater, mesh II with long heater.

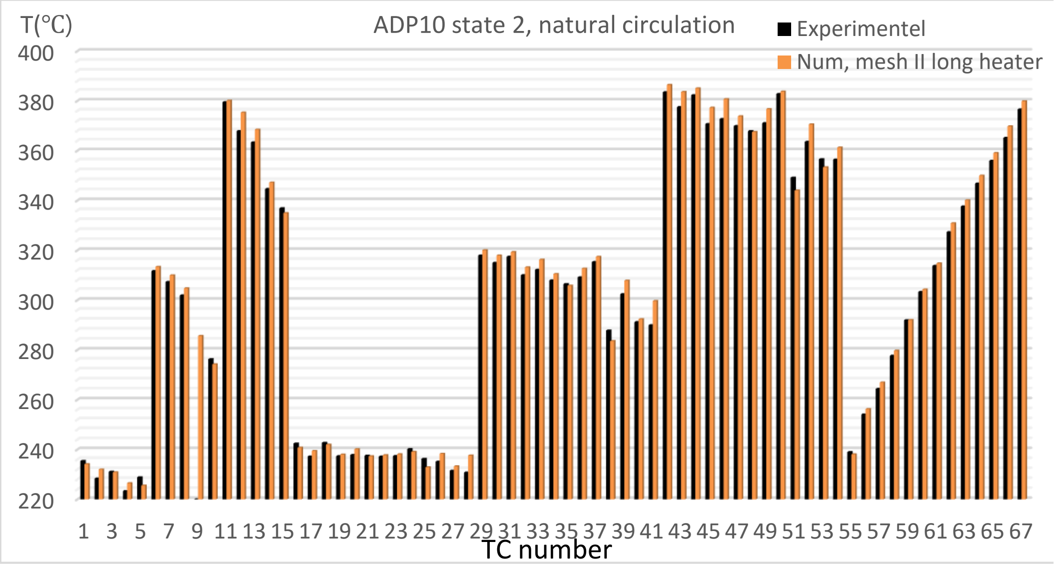

Fig.11 Natural circulation results mesh II with preheating is considered, long heater.

Conclusions

In the open phase of the NACIE -UP benchmark, we were able to test various modelling methodologies. Moreover, we could show less sensitivity of results to mesh refinement. Considering the good quality of our simulations at a relatively low cost, we recommend using the finer mesh and more details in the heater model. When looking at the small differences between the simulations and experiments for the more complex modelling strategy we can still observe slightly better qualitative agreement. This is the main reason, why the more demanding mesh should be employed in the simulations of the blind phase.

We tried various hypothesis to explain systematic deviations between simulation and experiments, including asymmetries and heat losses.

None of these could be confirmed by a trend in the data, so that we believe that statistical deviations are dominant and further improvements by more complex models cannot be expected. In regions with high temperatures the uncertainty due to heating power, benchmark specification, and modelling (physical parameters, turbulence models) is dominant. In the inlet region with low temperatures the uncertainty becomes larger as the uncertainty of the boundary conditions becomes more prominent.

Acknowledgments

This work has been supported by the Framatome Professional School at KIT. The data and information presented in the paper are part of an ongoing IAEA coordinated research project on "Benchmark of Transition from Forced to Natural Circulation Experiment with Heavy Liquid Metal Loop – CRP-I31038".

The work presented is original but some or all of the information may need to be included in a book publication at a later date as part of the output of the an International Atomic Energy Agency coordinated research project on "Benchmark of Transition from Forced to Natural Circulation Experiment with Heavy Liquid Metal Loop – CRP-I31038"

References

[1] Di Piazza, I., Hassan, H., Lorusso, P., Martelli, D., “Benchmark specifications for nacie-up facility: non-uniform power distribution tests”, Ref. NA-I-R-542, Issued: 28/02/2023 ENEA, Italy.

[2] N. E. Agency, “Handbook on Lead-bismuth Eutectic Alloy and Lead Properties, Materials Compatibility , Thermal- hydraulics and Technologies,” Nucl. Sci., pp. 647–730, 2015.

[3] Kim, C.S., “Thermophysical properties of stainless steels”, ANL-75-55, 1975.

[4] Thermocoax, private communication

[5] Batta, A., Class, A., “CFD validation for partially blocked wire-wrapped liquid-metal cooled 19-pin hexagonal rod bundle carried out at KIT-KALLA”, Proc. of the 19th International Topical Meeting on Nuclear Reactor Thermal Hydraulics (NURETH-19) Log nr.: 36240 Brussels, Belgium, March 6 - 11, 2022

[6] Batta, A. Class, A. Pacio, J. Vlidation for CFD thermalhydraulic simulation for liquid metal cooled blocked 19-pin hexagonal wire wrapped rod bundle experiment carried out at KIT-KALLA, AMNT 50, 2019

[7] Batta, A.: Class, A. Thermalhydraulic CFD validation for liquid metal cooled 19-pin hexagonal wire wrapped rod bundle, paper 28473, Nureth 18

[8] Batta, A.: Class, A.; Pacio, J. Numerical analysis of a LBE-cooled blocked 19-pin hexagonal wire wrapped rod bundle experiment carried out at KIT-KALLA within EC-FP7 project MAXSIMA” Paper ID 20532, Nureth 17

[9] Marinari, R., Di Piazza, I., Angelucci, M., Martelli, D., “POST-TEST CFD ANALYSIS OF non-uniformly heated 19-pin fuel bundle cooled by HLM”, ICONE26-81307, Proc. ICONE26, July 22-26, 2018, London.

[10] Angelucci, M., Di Piazza, I., Tarantino, M., Marinari, R., Polazzi, G., Sermenghi, V., “Experimental tests with non-uniformly heated 19-pins fuel bundle cooled by hlm”, ICONE26-81216, Proc. ICONE26, July 22-26, 2018, London.

[11] Marinari, R., Di Piazza, I., Tarantino, M., Angelucci, M., Martelli, D., “Experimental tests and post-test analysis of non-uniformly heated 19-pins fuel bundle cooled by Heavy Liquid Metal”, Nucl.Eng. Des., Vol. 343, pg. 166-177, 2019

List of Puplications

[1] Arndt, T.; Jordan, T.; Tromm, T. W., Hydrogen (Safety) Research at KIT. UNCC (2022), Karlsruhe, Deutschland, 26. Oktober 2022.

[2] Batta, A.; Class, A. G., CFD-Validation for Partially Blocked Wire-Wrapped Liquid-Metal Cooled 19-Pin Hexagonal Rod Bundle Carried out at KIT-KALLA. 19th International Topical Meeting on Nuclear Reactor Thermal Hydraulics (NURETH-19), Brüssel, Belgien, 6.–11. März 2022.

[3] Batta, A.; Class. A. G., CFD-Validation for Partially Blocked Wire-Wrapped Liquid-Metal Cooled 19-Pin Hexagonal Rod Bundle Carried out at KIT-KALLA. 19th International Topical Meeting on Nuclear Reactor Thermal Hydraulics Proceedings, Paper Log nr.: 36240.

[4] Baur, S.; Seibt, A.; Kuhn, D., Laboratory flow-through experiments to determine the effect of inhibitors in the injection of fluids supersaturated with barium sulfate. European Geothermal Congress (EGC 2022), Berlin, Deutschland, 17.–21. Oktober 2022.

[5] Bigot, B.; Gaus-Liu, X.; Clavier, R.; Journeau, C.; Payot, F.; Cron, T.; Angeli, P. E.; Peybernes, M.; Fluhrer, B., Experimental and Numerical Simulations on SFR Core-Catcher Safety Analysis After Relocation of Corium. 10th European Review Meeting on Severe Accident Research (ERMSAR 2022), Karlsruhe, Deutschland, 16.–19. Mai 2022.

[6] Brode, B.; Köhl, B.; Schlegel, P.; Eichinger, F.; Iannotta, J.; Kuhn, D.; Seibt, A.; Teitz, S.; Würdemann, H., Site-specific solutions to reduce calcium carbonte precipitations in production wells in the South German Molasse Basin - Results from EvA-M 2.0 project. European Geothermal Congress (EGC 2022), Berlin, Deutschland, 17.–21. Oktober 2022.

[7] Bühler, L.; Brinkmann, H.-J.; Courtessole, C.; Klüber, V.; Köhly, C.; Mistrangelo, C., Magnetohydrodynamics for liquid-metal blankets. Annual Report 2020 of the Institute for Thermal Energy Technology and Safety. Hrsg.: W. Tromm, 5–19, KIT Scientific Publishing.

[8] Bühler, L.; Courtessole, C.; Mistrangelo, C., Magnetohydrodynamic flows in strong magnetic fields for application in fusion blankets [in press]. Proceedings of the 12th International PAMIR Conference, Fundamental and Applied MHD, Krakow, PL, July 4-8, 2022, 1, International Atomic Energy Agency (IAEA).

[9] Bühler, L.; Courtessole, C.; Mistrangelo, C., Magnetohydrodynamic flows in strong magnetic fields for application in fusion blankets. 12th International PAMIR Conference, Fundamental and Applied MHD, Krakau, Polen, 4.–8. Juli 2022.

[10] Bühler, L.; Klüber, V.; Mistrangelo, C., Magnetohydrodynamic flow in stepwise bent circular pipes. Magnetohydrodynamics, 58 (4), 425 – 433. doi:10.22364/mhd.58.4.6

[11] Bühler, L.; Klüber, V.; Mistrangelo, C., Magnetohydrodynamic flow in stepwise bent circular pipes [in press]. Proceedings of the 12th International PAMIR Conference, Fundamental and Applied MHD, Krakow, PL, July 4-8, 2022, 340–345.

[12] Bühler, L.; Klüber, V.; Mistrangelo, C., Magnetohydrodynamic flow in stepwise bent circular pipes. 12th International PAMIR Conference, Fundamental and Applied MHD, Krakau, Polen, 4.–8. Juli 2022.

[13] Bykov, V.; Koksharov, A.; Kuznetsov, M.; Zhukov, V. P., Hydrogen-oxygen flame acceleration in narrow open ended channels. Combustion and Flame, 238, Art.-Nr.: 111913. doi:10.1016/j.combustflame.2021.111913

[14] Chavali, A.; Denkevits, A.; Hu, G.; Jedicke, O.; Jordan, T.; Kaup, B.; Kotchourko, A.; Kuznetsov, M.; Lelyakin, A.; Prestel, F.; Stassen, M.; Xiao, J.; Xu, Z., Fundamental Behaviour of Hydrogen to Applied Accident Consequence Analysis for Hydrogen as a Safe Energy Carrier. Annual Report 2020 of the Institute for Thermal Energy Technology and Safety. Hrsg.: W. Tromm, 51–57, KIT Scientific Publishing.

[15] Cirrone, D.; Makarov, D.; Friedrich, A.; Grune, J.; Takeno, K.; Molkov, V., Blast Wave Generated by Delayed Ignition of Under-Expanded Hydrogen Free Jet at Ambient and Cryogenic Temperatures. Hydrogen, 3 (4), 433–449. doi:10.3390/hydrogen3040027

[16] Cirrone, D.; Makarov, D.; Kuznetsov, M.; Friedrich, A.; Molkov, V., Effect of heat transfer through the release pipe on simula-

tions of cryogenic hydrogen jet fires and hazard distances. International Journal of Hydrogen Energy, 47 (50), 21596–21611. doi:10.1016/j.ijhydene.2022.04.276

[17] Class, A., Annual report of the Framatome Professional School. Annual Report 2020 of the Institute for Thermal Energy Technology and Safety. Hrsg.: W. Tromm, 67–73, KIT Scientific Publishing.

[18] Daubner, M.; Fellmoser, F.; Hofberger, C.; Kamienowska, M.; Krumholz, R.; Laube, T.; Litfin, K.; Müller-Trefzer, F.; Niedermeier, K.; Stoppel, L.; Uhlenbruck, N.; Wetzel, T.; Wittemann, K., Liquid metal technology research at Karlsruhe Liquid Metal Laboratory 2020 – Fueling sustainable energy and process technology by innovative approaches. Annual Report 2020 of the Institute for Thermal Energy Technology and Safety. Hrsg.: W. Tromm, 31–37, KIT Scientific Publishing.

[19] Fluhrer, B.; Gaus-Liu, X.; Cron, T.; Stängle, R.; Vervoortz, M.; Wenz, T., LIVE-BWR Experiments to Study the Effect of CRGT Cooling on In-Vessel Melt Retention Strategy. 19th Int. Topical Meeting on Nuclear Reactor Thermal Hydraulics (NURETH-19) Proceedings, Nr.: 35414.

[20] Fluhrer, B.; Gaus-Liu, X.; Cron, T.; Stängle, R.; Vervoortz, M.; Wenz, T. (2022, März). LIVE-BWR Experiments to Study the Effect of CRGT Cooling on In-Vessel Melt Retention Strategy. 19th International Topical Meeting on Nuclear Reactor Thermal Hydraulics (NURETH-19 2022), Brüssel, Belgien, 6.–11. März 2022.

[21] Friedrich, A.; Necker, G.; Stern, G.; Veser, A.; Grune, J.; Kuznetsov, M.; Jordan, T., Combustion experiments with homogeneous and gradient H2-CO-air-mixutres in semi-confined geometries. 33rd Meeting of the German CFD Network of Competence, Online, 22.–23. März 2022.

[22] Friedrich, A.; Veser, A.; Gerstner, J.; Jordan, T.; Kuznetsov, M.; Kotchourko, N. (2022, Mai 12). PRESLHY Experiment series 3.4. doi:10.5445/IR/1000145885

[23] Friedrich, A.; Veser, A.; Jordan, T. (2022, Mai 10). PRESLHY Experiment series 3.1, part B. doi:10.5445/IR/1000145859

[24] Friedrich, A.; Veser, A.; Jordan, T.; Kuznetsov, M.; Kotchourko, N. (2022, Mai 12). PRESLHY Experiment series 4.4; Material of the ground: gravel. doi:10.5445/IR/1000145889

[25] Friedrich, A.; Veser, A.; Jordan, T.; Kuznetsov, M.; Kotchourko, N. (2022, Mai 12). PRESLHY Experiment series 4.4; Material of the ground: water. doi:10.5445/IR/1000145888

[26] Friedrich, A.; Veser, A.; Jordan, T.; Kuznetsov, M.; Kotchourko, N. (2022, Mai 12). PRESLHY Experiment series 4.4; Material of the ground: concrete. doi:10.5445/IR/1000145887

[27] Friedrich, A.; Veser, A.; Jordan, T.; Kuznetsov, M.; Kotchourko, N. (2022, Mai 12). PRESLHY Experiment series 4.4; Material of the ground: sand. doi:10.5445/IR/1000145886

[28] Fuchs, S.; Jordan, T. L., „Mit grünem Wasserstoffmotor geht der Umstieg schneller.“ – KIT-Experte Thomas Jordan plädiert für Technologieoffenheit bei der Dekarbonisierung des Verkehrs. - Campus-Report am 11.10.2022. doi:10.5445/IR/1000150087

[29] Fuchs, S.; Jordan, T. L., „Hoffnungsträger in der Energiekrise“ – Forschungsprojekte am Karlsruher Institut für Technologie bereiten den Umstieg auf Wasserstoff vor. - Campus-Report am 12.07.2022. doi:10.5445/IR/1000148532

[30] Fuchs, S.; Ottenburger, S. S., „Den Total-Blackout in jedem Fall verhindern“ – Resilienzforschung am KIT - Campus-Report am 18.10.2022. doi:10.5445/IR/1000151566

[31] Gabriel, S.; Albrecht, G.; Heiler, W.; Heineken, F., Detailed investigations on flow boiling of water up to the critical heat flux. Annual Report 2020 of the Institute for Thermal Energy Technology and Safety. Hrsg.: W. Tromm, 25–30, KIT Scientific Publishing.

[32] Gardella, L.; Wiemer, H.-J., First experimental results of a supercritical Organic Rankine cycle using propane as working fluid. Annual Report 2020 of the Institute for Thermal Energy Technology and Safety. Hrsg.: W. Tromm, 59–65, KIT Scientific Publishing.

[33] Gaus-Liu, X., Recent Severe Accident Experimental Programs LIVE JIMEC. ESFR-SMART European Workshop No 7 Sodium-Cooled Fast Reactor Severe Accidents, CEA Cadarache, Frankreich, 5.–8. April 2022.

[34] Gaus-Liu, X.; Bigot, B.; Journeau, C.; Payot, F.; Cron, T.; Clavier, R.; Peybernes, M.; Angeli, P. E.; Fluhrer, B., Experiment and Numerical Simulation on SFR Core-Catcher Safety Analysis After Relocation of Corium. International Conference on Fast Reactors and Related Fuel Cycles : Sustainable Clean Energy for the Future (FR22), Wien, Österreich, 19.–22. April 2022.

[35] Gaus-Liu, X.; Cron, T.; Bottomley, D.; Fluhrer, B., MCCI on Siliceous and LCS Concrete with Oxide and Metallic Melt: Re-Evaluation of MOCKA Experiments. 19th International Topical Meeting on Nuclear Reactor Thermal Hydraulics (NURETH-19) Proceedings, Nr.: 35635.

[36] Gaus-Liu, X.; Cron, T.; Bottomley, D.; Fluhrer, B., MCCI on Siliceous and LCS Concrete with Oxide and Metallic Melt: Re-Evaluation of MOCKA Experiments. 19th International Topical Meeting on Nuclear Reactor Thermal Hydraulics (NURETH-19), Brüssel, Belgien, 6.–11. März 2022.

[37] Gaus-Liu, X., SAR/ITES research activities in 2020. Annual Report 2020 of the Institute for Thermal Energy Technology and Safety. Hrsg.: W. Tromm, 21–23, KIT Scientific Publishing.

[38] Gaus-Liu, X.; Bubelis, E.; Perez-Martin, S.; Ghidersa, B.-E.; Hering, W., Design Features and Simulation of the New-Build HELOKA-US Facility for the Validation of the DEMO Helium-Cooled Pebble Bed Intermediate Heat Transport and Storage System. Journal of Nuclear Engineering, 3 (4), 461–472. doi:10.3390/jne3040032

[39] Hu, G.; Zhang, H.; Liu, Q., Design optimization on characteristics of packed-bed thermal energy storage system coupled with high temperature gas-cooled reactor pebble-bed module. Energy Conversion and Management, 257, Art.-Nr.: 115434. doi:10.1016/j.enconman.2022.115434

[40] Hu, G.; Zhang, H.; Liu, Q., Assessment on population balance model and wall boiling model for subcooled boiling flow of steam generator of nuclear power plant. Annals of Nuclear Energy, 173, Art.-Nr.: 109128. doi:10.1016/j.anucene.2022.109128

[41] Jähnichen, S.; Degering, D.; Heberling, F.; Hoffmann, R.; Kuhn, D.; Langenmaier, M.; Otto, T.; Seibt, A.; Uhde, J., Characterization of scales from a geothermal plant in the Upper Rhine Graben after long-term application of an inhibitor combination. European Geothermal Congress (EGC 2022), Berlin, Deutschland, 17.–21. Oktober 2022.

[42] Jordan, T.; Friedrich, A., Stand der Wasserstoffsicherheit in Deutschland und Europa. DVGW-Schulung "H2 Sicherheit", Online, 26. Januar 2022.

[43] Jordan, T., Research on the safety of cryogenic hydrogen. 3rd International Workshop on Hydrogen Safety Codes and Standards in the South African Context (IWHSCS 2022), Darmstadt, Deutschland, 2.–3. März 2022.

[44] Jordan, T., Mobile Hydrogen Storage - Challenges and Solutions. 3. Antrieb der Zukunft : Tagung Wasserstoffmotor in Ettlingen, Ettlingen, Deutschland, 14. September 2022.

[45] Jordan, T., Wasserstoff-Opportunitäten. 23. Bodensee-Seminar, IHK Bodensee-Oberschwaben, Konstanz, Deutschland, 30. September–1. Oktober 2022.

[46] Jordan, T., New Liquid Hydrogen Work. HySafe Research Priorities Workshop, Quebec, Kanada, 21.–23. November 2022.

[47] Jordan, T.; Friedrich, A., Stand der Wasserstoffsicherheit in Deutschland und Europa. DVGW-Schulung "H2 Sicherheit", Online, 23. November 2022.

[48] Kağan Mercan, A.; Gabrielli, F.; Hugo Sanchez-Espinoza, V.; Raskob, W., Analysis of the consequences of a LBLOCA with SBO severe accident in a generic VVER-1000 by means of ASTEC and JRODOS codes. Nuclear Engineering and Design, 400, Art.-Nr. 112078. doi:10.1016/j.nucengdes.2022.112078

[49] Kamienowska, M.; Niedermeier, K.; Bender, M.; Wetzel, T., Production of anhydrous formaldehyde with co-generation of hydrogen. The Role of Catalysis for the Energy Transition, Ludwigshafen am Rhein, Deutschland, 5.–7. Oktober 2022.

[50] Kamienowska, M.; Niedermeier, K.; Stoppel, L.; Daubner, M.; Bender, M.; Wetzel, T., Development of Sodium Catalyst Dosing Method for Water Free Formaldehyde Production. Annual Meeting on Reaction Engineering and ProcessNet Subject Division Heat and Mass Transfer, Würzburg, Deutschland, 18.–20. Juli 2022.

[51] Keßlau, K.; Litfin, K., Keramik 3D-Druck leistet Beitrag zur Entwicklung sauberer Kernenergie, Wissenschaftskommunikation im Internet.

[52] Köhly, C.; Bühler, L., Design of a scaled mockup of the WCLL TBM for MHD experiments in liquid metal manifolds and breeder units. 32nd Symposium on Fusion Technology (SOFT 2022), Dubrovnik, Kroatien, 18.–23. September 2022.

[53] Kuhn, D.; Wiemer, H.-J.; Stern, G.; Gardella, L.; Fossati, M.; Leuteu Sahmen, M., Grundlagen effizienter und hygienischer Verdunstungskühlung. Haus der Technik, Essen, Deutschland, 25. Januar 2022.

[54] Kuznetsov, M., Flame acceleration and detonation transition of hydrogen-air mixtures at cryogenic temperatures. International Workshop on Explosion and Reactive Flow, Peking, China, 16.–17. Juli 2022.

[55] Kuznetsov, M.; Denkevits, A.; Friedrich, A.; Veser, A., Critical Conditions for Flame Acceleration and DDT for Hydrogen-Air Mixtures at Cryogenic Temperatures. 28th International Colloquium on the Dynamics of Explosions and Reactive Systems (ICDERS 2022), Napoli, Italien, 19.–24. Juni 2022.

[56] Kuznetsov, M.; Denkevits, A.; Veser, A.; Friedrich, A., Flame propagation regimes and critical conditions for flame acceleration and detonation transition for hydrogen-air mixtures at cryogenic temperatures. International Journal of Hydrogen Energy, 47 (71), 30743–30756. doi:10.1016/j.ijhydene.2022.07.024

[57] Kuznetsov, M.; Friedrich, A.; Necker, G.; Veser, A.; Breitung, W., An analysis of combustion regimes for hydrogen/CO/air mixtures in different geometries. Proceedings of the 10th European Review Meeting on Severe Accidents Research (ERMSAR 2022) : Severe Accident Research Eleven Years after the Fukushima Accident : in memory of Martin Kissane : Karlsruhe, Germany, May 16-19, 2022. Ed.: F. Gabrielli, Artikel-Nummer: 334, Karlsruher Institut für Technologie (KIT).

[58] Kuznetsov, M.; Friedrich, A.; Necker, G.; Veser, A.; Breitung, W., An analysis of combustion regimes for hydrogen/CO/air mixtures in different geometries. 10th European Review Meeting on Severe Accident Research (ERMSAR 2022), Karlsruhe, Deutschland, 16.–19. Mai 2022.

[59] Laube, T.; Dietrich, B.; Marocco, L.; Wetzel, T., Turbulent heat transfer in a liquid metal tube flow with azimuthally inhomogeneous heat flux. International Journal of Heat and Mass Transfer, 189, Art.-Nr.: 122734. doi:10.1016/j.ijheatmasstransfer.2022.122734

[60] Laube, T.; Dietrich, B.; Marocco, L.; Wetzel, T., Analysis of Thermoelastic Stress in a Tube with Azimuthally Inhomogeneous Heat Flux and Liquid Metal Cooling. 28th SolarPACES, Albuquerque, NM, USA, 27.–30. September 2022.

[61] Lei, B.; Xiao, J.; Kuznetsov, M.; Jordan, T., Effects of heat transfer mechanism on methane-air mixture explosion in 20 L spherical device. Journal of Loss Prevention in the Process Industries, 80, Article no: 104864. doi:10.1016/j.jlp.2022.104864

[62] Ma, Y.; Hu, G.; Zhang, H.; Liu, Q., Comparison of breakup and coalescence kernels in population balance model for modeling isothermal gas-liquid flow. Nuclear Engineering and Design, 388, Art.-Nr.: 111616. doi:10.1016/j.nucengdes.2021.111616

[63] Madokoro, H.; Yamashita, T.; Sato, I.; Gaus-Liu, X.; Cron, T.; Fluhrer, B.; Stängle, R.; Wenz, T.; Vervoortz, M., LIVE-J1 Experiment on Debris Melting Behavior Toward Understanding Late In-Vessel Accident Progression of the Fukushima Daiichi Nuclear Power Station. 19th International Topical Meeting on Nuclear Reactor Thermal Hydraulics (NURETH-19 2022), Brüssel, Belgien, 6.–11. März 2022.

[64] Madokoro, H.; Yamashita, T.; Sato, I.; Gaus-Liu, X.; Cron, T.; Fluhrer, B.; Stängle, R.; Wenz, T.; Vervoortz, M.; Mizokami, S., LIVE-J1 Experiment on Debris Melting Behavior Toward Understanding Late In-Vessel Accident Progression of the Fukushima Daiichi Nuclear Power Station. 19th International Topical Meeting on Nuclear Reactor Thermal Hydraulics Proceedings, Nr.: 36023.

[65] Madokoro, H.; Yamashita, T.; Gaus-Liu, X.; Cron, T.; Fluhrer, B.; Sato, I.; Mizokami, S., The Experimental and Simulation Results of LIVE-J2 Test — Investigation on Heat Transfer in a Solid-Liquid Mixture Pool. Nuclear Technology, 209 (2), 144–168. doi:10.1080/00295450.2022.2121545

[66] Marthaler, P.; Class, A. G., A Fourier-Chebyshev non-interpolating method for the direct numerical simulation of two-dimensional wall-induced electrokinetic flow. 75th Annual Meeing of the APS Division of Fluid Dynamics, Indianapolis, IN, USA, 20.–22. November 2022.

[67] Marthaler, P. G.; Class, A. G., Weak curvature asymptotics for Debye layers as electrohydrodynamic discontinuities. Physical Review E, 105 (3), Art.-Nr.: 035106. doi:10.1103/PhysRevE.105.035106

[68] Mercan, A. K.; Gabrielli, F.; Sanchez-Espinoza, V. H.; Raskob, W., Determination of the Radiological Consequences by means of JRODOS and JRODOS codes at a generic Akkuyu VVER-1000 plant unit. International Nuclear Sciences and Technologies Conference (INSTEC 2022), Tralleis, Türkei, 19.–22. Oktober 2022.

[69] Mistrangelo, C.; Bühler, L.; Klüber, V. (2022, September). Towards the simulation of MHD flow in an entire WCLL blanket mock-up. 32nd Symposium on Fusion Technology (SOFT 2022), Dubrovnik, Kroatien, 18.–23. September 2022.

[70] Müller-Trefzer, F.; Hesse, R.; Niedermeier, K.; Heinzel, A.; Wetzel, T., Filler Material Screening for a Dual-Media Energy Storage with Liquid Metal as Heat Transfer Fluid. 28th SolarPACES, Albuquerque, NM, USA, 27.–30. September 2022.

[71] Müller-Trefzer, F.; Niedermeier, K.; Daubner, M.; Wetzel, T., Experimental investigations on the design of a dual-media thermal energy storage with liquid metal. Applied Thermal Engineering, 213, Art.-Nr.: 118619. doi:10.1016/j.applthermaleng.2022.118619

[72] Niedermeier, K.; Klasing, F.; Lux, M.; Daubner, M.; Weisenburger, A.; Bonk, A.; Bauer, T.; Wetzel, T., Testing key components for Carnot batteries in molten lead and molten salt at elevated temperatures. 3rd International Workshop on Carnot Batteries, Stuttgart, Deutschland, 27.–28. September 2022.

[73] Niedermeier, K.; Lux, M.; Weisenburger, A.; Wetzel, T., Design of an Experimental Loop for Testing Key Components for Thermal Energy Storage with Liquid Lead at 700 °C. International Renewable Energy Storage and Systems Conference (IRES 2022), Düsseldorf, Deutschland, 20.–22. September 2022.

[74] Niedermeier, K.; Müller-Trefzer, F.; Wetzel, T., High temperature heat storage with liquid metals as heat transfer fluids - status and challenges. 2nd World Energy Storage Conference (WESC) / 7th UK Energy Storage Conference (UKESC), Birmingham, Vereinigtes Königreich, 12.–14. Oktober 2022.

[75] Niedermeier, K.; Sinning, S.; Müller-Trefzer, F.; Marocco, L.; Wetzel, T., Liquid metal as heat transfer fluid in dual-media sensible and latent heat storage. Proceedings of the 17th UK Heat Transfer Conference (UKHTC 2021), Manchester, UK, April 4-6, 2022.

[76] Niedermeier, K.; Sinning, S.; Müller-Trefzer, F.; Marocco, L.; Wetzel, T., Liquid metal as heat transfer fluid in dual-media sensible and latent heat storage. 17th UK Heat Transfer Conference (UKHTC 2022), Manchester, Vereinigtes Königreich, 4.–6. April 2022.

[77] Niedermeier, K.; Mueller-Trefzer, F.; Daubner, M.; Marocco, L.; Weisenburger, A.; Wetzel, T., Theoretical and experimental studies of dual-media thermal energy storage with liquid metal. 26th International Conference on Concentrating Solar Power and Chemical Energy Systems (SolarPACES 2020), Article no: 160011, AIP Publishing. doi:10.1063/5.0085881

[78] Niedermeier, K.; Müller-Trefzer, F.; Marocco, L., Parametric study of filler size and properties for a liquid-metal thermal energy storage. Applied Thermal Engineering, 212, Article no: 118568. doi:10.1016/j.applthermaleng.2022.118568

[79] Ottenburger, S. S.; Möhrle, S.; Müller, T. O.; Raskob, W., A Novel MCDA-Based Methodology Dealing with Dynamics and Ambiguities Resulting from Citizen Participation in the Context of the Energy Transition. Algorithms, 15 (2), Article no: 47. doi:10.3390/a15020047

[80] Ottenburger, S. S.; Raskob, W.; Müller, T.; Möhrle, S., Smart Resilience Engineering: Mitigative Planning of Networked Infrastructures, Uncertainties and Robust Management. Annual Report 2020 of the Institute for Thermal Energy Technology and Safety.

Hrsg.: W. Tromm, 39–49, KIT Scientific Publishing.

[81] Pacio, J.; Van Tichelen, K.; Eckert, S.; Wondrak, T.; Di Piazza, I.; Lorusso, P.; Tarantino, M.; Daubner, M.; Litfin, K.; Ariyoshi, G.; Obayashi, H.; Sasa, T., Advanced Thermal-Hydraulic experiments and instrumentation for heavy liquid metal reactors. Nuclear Engineering and Design, 399, Art.-Nr.: 112010. doi:10.1016/j.nucengdes.2022.112010

[82] Ren, Z.; Giannissi, S.; Venetsanos, A. G.; Friedrich, A.; Kuznetsov, M.; Jordan, T.; Wen, J. X., The evolution and structure of ignited high-pressure cryogenic hydrogen jets. International Journal of Hydrogen Energy, 47 (67), 29184–29194. doi:10.1016/j.ijhydene.2022.06.230

[83] Rosenstiel, A.; Vehse, M.; Peterssen, F.; Voglstätter, C.; Kolb, T.; Jordan, T.; Musonda, F.; Thrän, D., Wasserstoff als zentraler Baustein der Sektorenkopplung. Mit Wasserstoff zur Klimaneutralität - von der Forschung in die Anwendung : Jahrestagung 2021 des ForschungsVerbunds Erneuerbare Energien 10. und 11. November 2021, 23–28, ForschungsVerbund Erneuerbare Energien (FVEE).

[84] Schulenberg, T.; Otic, I., Concept of a Small Modular SCWR With Horizontal Fuel Assemblies. Journal of Nuclear Engineering and Radiation Science, 8 (3), Pap. No:NERS-21–1074. doi:10.1115/1.4052191

[85] Staiß, F.; Adolf, J.; Ausfelder, F.; Erdmann, C.; Fischedick, M.; Hebling, C.; Jordan, T.; Klepper, G.; Müller, T.; Palkovits, R.; Poganietz, W.-R.; Schill, W.-P.; Schmidt, M.; Stephanos, C.; Stöcker, P.; Wagner, U.; Westphal, K.; Wurbs, S., Optionen für den Import grünen Wasserstoffs nach Deutschland bis zum Jahr 2030 Transportwege – Länderbewertungen – Realisierungserfordernisse. acatech - Deutsche Akademie der Technikwissenschaften. doi:10.48669/esys_2022-6

[86] Thomas, J., Safety of Cryogenic Hydrogen. 772. WE-Heraeus-Seminar: Metrology and Process Safety for Hydrogen Technologies & Applications, Bad Honnef, Deutschland, 10.–13. Oktober 2022.

[87] Tromm, T. W., Überblick Kompetenzverbund Kerntechnik (KVKT). Sitzung der Entsorgungskommission (RSK 2022), Bonn, Deutschland, 15. Juni 2022.

[88] Tromm, T. W., Rückbau kerntechnischer Anlagen. VDI Wissensforum, Rückbau kerntechnischer Anlagen, Workshop: Nukleares Erbe, Berlin, Deutschland, 5. Juli 2022.

[89] Tromm, T. W., Outlook Programme NUSAFE at KIT and Helmholtz Association. 27th International QUENCH Workshop, Karlsruhe, Deutschland, 27.–29. September 2022.

[90] Tromm, T. W., Können Kernreaktoren das Klima retten?. Ringvorlesung Umweltethik in der Hochschule Rhein-Bonn-Sieg, Siegburg, Deutschland, 21. April 2022.

[91] Tromm, T. W., Programme Nusafe Reactor Safety Research at KIT. UNCC, Karlsruhe, Deutschland, 26. Oktober 2022.

[92] Tromm, T. W., Overview Programme NUSAFE at KIT and Helmholtz Association. Union Stiftung, Eggenstein-Leopoldshafen, Deutschland, 26. November 2022.

[93] Tromm, W. (Hrsg.), Annual Report 2021 of the Institute for Thermal Energy Technology and Safety. Karlsruher Institut für Technologie (KIT). doi:10.5445/IR/1000153904

[94] Tromm, W., Structure and Activities of the Institute for Thermal Energy Technology and Safety (ITES). Annual Report 2020 of the Institute for Thermal Energy Technology and Safety. Hrsg.: W. Tromm, 1–3, KIT Scientific Publishing.

[95] Tromm, W. (Hrsg.)., Annual Report 2020 of the Institute for Thermal Energy Technology and Safety (KIT Scientific Reports ; 7762). KIT Scientific Publishing. doi:10.5445/KSP/1000140139

[96] Tromm, W. T., Hochtemperaturspeicher. VDI Fachausschuss Kraftwerkstechnik, Düsseldorf, Deutschland, 23. November 2022.

[97] Tromm, W. T., Können Kernreaktoren das Klima retten?. Hans Seidel Stiftung, Bildungszentrum Kloster Banz, Banz, Deutschland, 26. November 2022.

[98] Tromm, W. T., Overview Programme NUSAFE at KIT and Helmholtz Association. 27th International QUENCH Workshop, Karlsruhe, Deutschland, 27.–29. September 2022.

[99] Uhlenbruck, N.; Dietrich, B.; Durán, I.; Hofberger, C.; Stoppel, L.; Wetzel, T., Preliminary Analysis of Carbon Produced from Methane Pyrolysis in a Liquid Metal Bubble Column Reactor. CMEMS, Kopenhagen, Dänemark, 6.–8. Juli 2022.

[100] Uhlenbruck, N.; Dietrich, B.; Hofberger, C.; Stoppel, L.; Wetzel, T., Methane Pyrolysis in a Liquid Metal Bubble Column Reactor: A Model Approach Combining Bubble Dynamics with Byproduct and Soot Formation. Energy Technology, 10 (11), Art.-Nr.: 2200654. doi:10.1002/ente.202200654

[101] Veser, A.; Friedrich, A.; Jordan, T.; Kuznetsov, M.; Kotchourko, N. (2022, Mai 12). PRESLHY Experiment series 5.3; block ratio: 60%; initial temperature: approx. 80K (cold). doi:10.5445/IR/1000145896

[102] Veser, A.; Friedrich, A.; Jordan, T.; Kuznetsov, M.; Kotchourko, N. (2022, Mai 12). PRESLHY Experiment series 5.3; block ratio: 30%; initial temperature: approx. 80K (cold). doi:10.5445/IR/1000145895

[103] Veser, A.; Friedrich, A.; Jordan, T.; Kuznetsov, M.; Kotchourko, N. (2022, Mai 12). PRESLHY Experiment series 5.3; block ratio: 0%; initial temperature: approx. 80K (cold). doi:10.5445/IR/1000145893

[104] Veser, A.; Friedrich, A.; Jordan, T.; Kuznetsov, M.; Kotchourko, N. (2022, Mai 12). PRESLHY Experiment series 5.3; block ratio: 60%; initial temperature: ambient (warm). doi:10.5445/IR/1000145892

[105] Veser, A.; Friedrich, A.; Jordan, T.; Kuznetsov, M.; Kotchourko, N. (2022, Mai 12). PRESLHY Experiment series 5.3; block ratio: 30%; initial temperature: ambient (warm). doi:10.5445/IR/1000145891

[106] Veser, A.; Friedrich, A.; Necker, G.; Kuznetsov, M.; Jordan, T., Flame Propagation in a Semiconfined Layer of Stratified Cryogenic Hydrogen-Air Mixture. 10th International Seminar on Fire and Explosion Hazards, Oslo, Norwegen, 22.–27. Mai 2022.

[107] Veser, A.; Jordan, T.; Kuznetsov, M.; Kotchourko, N.; Friedrich, A. (2022, Mai 12). PRESLHY Experiment series 5.3; block ratio: 0%; initial temperature: ambient (warm). doi:10.5445/IR/1000145890

[108] Wang, F.; Xiao, J.; Jordan, T., GASFLOW-MPI analysis on deflagration in full-scale hydrogen refueling station experiments: H2-air premixed cloud and high-pressure H2 jet. International Journal of Hydrogen Energy, 47 (32), 14725–14739. doi:10.1016/j.ijhydene.2022.02.215

[109] Weber, L.; Class, A. G., Methodology for statistical evaluation of bubbly flows using grouped bubble cells. 75th Annual Meeing of the APS Division of Fluid Dynamics, Indianapolis, IN, USA, 20.–22. November 2022.

[110] Yanez, J.; Class, A. G., Reduced Order Model of Standard k- ϵ turbulence model. Computers & Fluids, 245, Art.Nr. 105608. doi:10.1016/j.compfluid.2022.105608

[111] Yanez, J.; Kuznetsov, M.; Veiga-López, F., On the velocity, size, and temperature of gaseous dendritic flames. Physics of Fluids, 34 (11), Art.-Nr.: 113601. doi:10.1063/5.0118271

[112] Zheleznyak, M.; Donchyts, G.; Maderich, V.; Dronova, I.; Tkalich, P.; Trybushnyi, D.; Faybishenko, B.; Dvorzhak, A., Ecological footprint of Russia’s Ukraine invasion. Science, 377 (6612), 1273. doi:10.1126/science.ade6869

KIT Scientific Working Papers
ISSN 2194-1629

www.kit.edu